University of Tokyo

Turbulent Mixing and Transport of Collision-less Plasmas across a Stratified Velocity Shear Layer

A dissertation submitted in partial satisfaction
of the requirements for the degree
Doctor of Philosophy in Earth and Planetary Sciences

by

Yosuke Matsumoto

January
2004

To my parents

Table of Contents

0.1 Cross-field diffusion across a homogeneous velocity shear layer xvii

0.2 Turbulent mixing and transport across a stratified velocity shear layer xvii

0.3 Dawn-dusk asymmetry in the non-linear development of the K-H instability . xviii

1 General Introduction 1

1.1 Kelvin-Helmholtz instability 1

1.2 Sun-Earth connection 3

1.3 Theoretical and computational approach to K-H instability 6

2 Cross-field diffusion across a homogeneous velocity shear layer 11

2.1 Introduction 11

2.1.1 Magneto-hydro dynamic Kelvin-Helmholtz instability 11

2.1.2 Kinetic treatments on the Kelvin-Helmholtz instability 13

2.2 Linear analysis 14

2.3 Non-linear development of K-H instability 18

2.3.1 Initial conditions of simulations 18

2.3.2 Mixing rate 20

2.3.3 Non-linear development of the K-H instability for $\lambda/r_{gi} = 4.0$ 21

2.3.4 Simulation results for various λ/r_{gi} 33

2.3.5 Electron mixing process 35

2.3.6 Thin shear cases ($\lambda/r_{gi} = 1.0$) 37

2.4 Summary and discussion 45

3 Turbulent mixing and transport across a stratified velocity shear layer . 49

3.1 Introduction 49

3.2 Situation in consideration 54
3.3 Linear analysis 56
3.4 Ideal MHD Simulation 58
3.4.1 Simulation parameters and initial conditions 59
3.4.2 Linear growth 59
3.4.3 Onset of secondary instabilities in the non-linear stage of the K-H instability 60
3.4.4 Energy spectra 62
3.4.5 Baroclinicity inside the K-H vortex 62
3.4.6 Secondary Kelvin-Helmholtz and Rayleigh-Taylor instability 65
3.4.7 Width and position of the mixing layer 68
3.4.8 Effect of numerical resolution on the secondary instability 71
3.4.9 Effect of inhomogeneity in magnetic field 72
3.5 Full particle simulation 73
3.5.1 Initial condition 73
3.5.2 Linear growth 75
3.5.3 Onset of the secondary R-T instability 77
3.5.4 Mixing rate 77
3.5.5 Width of density interface 82
3.5.6 Energy spectrum 84
3.6 Summary and Discussion 88

4 Dawn-dusk asymmetry 91
4.1 Introduction 91
4.2 Initial condition 93

4.3 Non-linear development for $\lambda/r_{gi} = 4.0$ and $\alpha = 0.2$ 93

4.4 Ion orbits in a strong velocity shear layer 96

4.5 Modeling the outer edge of the vortex 101

4.6 Summary and Discussion 104

5 Concluding remarks 109

5.1 Summary and Conclusions 109

5.2 Important issues for future works 111

A Linear Analysis 113

A.1 Basic equations 113

A.1.1 Ideal MHD equations 113

A.1.2 Two fluid MHD equations 114

A.2 Linearization and solution 114

A.2.1 Ideal MHD 115

A.2.2 Two fluid MHD 116

B Rayleigh-Taylor instability 119

B.1 Rayleigh-Taylor instability 119

References 123

List of Figures

1.1 Ukiyoe. Adopted from Hokusai Katsushika, Fugaku Sanjurokkei [1831] . . . 1

1.2 A picture of clouds where the K-H seems to develop. The picture is adopted from the web site Houze's Cloud Atlas (http://www.atmos.washington.edu/gcg/Atlas/). 2

1.3 The simulation result which models the global interaction between the solar wind and the Venus ionosphere. The color intensity shows the number density of plasmas. The picture is cited from Figure 4 in Terada et al.[2002]. 3

1.4 Astrophysical phenomena where the K-H instability seems to operate. The left panel shows the X-ray image of the core of the galaxy cluster observed by *Chandra*. The image is cited from Figure 1(b) in Fujita et al.[2002]. The right panel shows the simulation result of the astrophysical jet performed by Hardee et al.[1997]. 4

1.5 Schematic view of the earth magnetosphere interacting with the solar wind (picture by J. Burch, Southwest Research Institute, San Antonio, USA). . . . 5

1.6 Left panel: Open magnetosphere model proposed by Dungey[1961]. The figure shows the cross section of the magnetosphere in the noon-midnight meridian plane (Adopted from Bothmer[1993]). Right panel: Close magnetosphere model proposed by Axford and Hines[1961]. The figure shows the cross section of the magnetosphere in the equatorial plane which is viewed from the north. 6

2.1 The growth rates of the K-H instability are shown for various mass ratios, 16(dash), 64(dash-dot) and 144(dash-three dots) along with the result for the ideal MHD case (solid). The abscissa shows the wave number in the x direction normalized by the initial shear width and the ordinate shows the growth rate normalized by the factor λ/V_0. 16

2.2 Eigen mode structures of the perturbed ion thermal pressure of the FGM for the mass ratio (A)16, (B)64, (C)144, and (D)the ideal MHD result. The color intensity indicates the power of the mode and the abscissa and the ordinate shows the x and y coordinate in the unit of the initial shear width. Perturbed and unperturbed velocity components are also added on the figure with the vector plot of the white arrows. (Non uniform intervals between the arrows in the y direction shown in (A)-(C) are due to the nonuniform grids adopted in those calculations.) 17

2.3 The initial setting of the simulation 19

2.4 The effect of the number of particles per cell on the evolution of the K-H instability. The figure shows time development of the y component of the perturbed ion velocity, whose mode number corresponds to the FGM. The results are shown for $N = 32$ (open diamond), $N = 128$ (asterisk), and $N = 256$ (solid line). 20

2.5 The relation between the occupation rate and the mixing rate. 22

2.6 Snapshots of the simulation result for $\lambda/r_{gi} = 4.0$. The color intensity indicates the occupation rate calculated in accordance with eq.(2.3). The contour lines show the electrostatic potential whose equipotential lines approximately indicate the fluid stream lines. 23

2.7 Snapshots of the electron occupation rate are shown in the same format of ion's in Fig. 2.6. 24

2.8 Time development of the FGM (solid line with asterisks) is shown in the same format of Figure 2.4. The dashed line shows the result obtained in the linear analysis. 25

2.9 Time profile of the integrated mixing rate for the ion (cross) and the electron (open square). The abscissa shows the time normalized by the factor λ/V_0 and the ordinate shows the integrated mixing rate normalized by the initial shear area $L_x\lambda$. 26

2.10 (A)The orbit in the simulation domain, (B)the time development of the y coordinate and (C)the x coordinate, and (D)the orbit in a phase space are shown. The coordinate x and y are normalized by the initial shear width λ, the time is normalized by the parameter λ/V_0, and the velocity is in the unit of the speed of light. 27

2.11 Same profiles as shown in Fig. 2.10but for the electron. 27

2.12 Snapshots of the ion mixing rate are shown in the same format of Fig. 2.6. . 28

2.13 Snapshots of the electron mixing rate are shown in the same format of ion's in Fig. 2.6. 29

2.14 The time profile of the average mixing rate for (A)the ion and (B)the electron as a function of the x direction is shown by the color intensity. The average mixing rate is obtained by integrating the mixing rate in the y direction normalized by the value integrated in the simulation domain at each time. The abscissa shows the normalized x coordinate and the ordinate shows the normalized time. 30

2.15 Time profile of (A)ion and (B)electron mixing rate with fitted curve lines (solid green) are shown in the same format of Fig.2.9. 32

2.16 The snapshots of the mixing rate of the ion in the simulation runs of $\lambda/r_{gi} =$ (A)1.0, (B)2.0 and (C)4.0 are shown. Figures show the same stages of the K-H instability, each of which are taken at $t = 95.31, 87.02, 82.87(\lambda/V_0)$, respectively. 33

2.17 Mixing rate for the various initial shear width for (A)the ion and (B)the electron. 35

2.18 The sliced cuts of the mixing rate are shown for λ/r_{gi} =1.0(black), 2.0(green), 4.0(red) to compare the width of the ion mixing area. The cuts are taken at (A)$x = 12.5\lambda$ and (B)$x = 6.25\lambda$ as indicated by the white vertical lines in Fig.2.16. 36

2.19 Time profile of the integrated mixing rate for the case $\lambda/r_{gi} = 1.0$ (cross), and $\lambda/r_{gi} = 2.0$ (asterisk) for (A)the ion and (B)the electron. Additionally, the red and green lines are shown. These two color lines show the result of the case $\lambda/r_{gi} = 4.0$ multiplied by a factor $\sqrt{\lambda_0/\lambda}$, where $\lambda_0 = 4r_{gi}$. 37

2.20 Snapshots of the electron mixing rate taken at $t = 82.37(\lambda/V_0)$ for each numbers of particles are shown. Meandering structure of the electron demarcation line is zoomed in the result with N=512. 38

2.21 Time profile of the electron integrated mixing rate for various particle numbers. The result for N=512 is not completed due to its large computational resources and the limited CPU time. 39

2.22 The energy spectra of the x component of the electric field normalized by the plasma energy density are shown for each particle numbers. The abscissa shows the wave number in the x direction normalized by the initial shear width λ. 40

2.23 The snapshots of the occupation rate of the ion 1 (left column) and the electron 1 (center column) with the z component of the magnetic field (right column). The vector plots of the black arrows in the B_z profiles show the electron velocity difference from the ion's $(\mathbf{V}_i - \mathbf{V}_e)$. From the top to the bottom panel snapshots are taken at $t = 62.16\lambda/V_0$, $t = 82.87\lambda/V_0$, $t = 103.59\lambda/V_0$. 41

2.24 The K-H eigen mode structure of the perturbed ion thermal pressure with the vector plot of the perturbed electric current density. 42

2.25 The y component of the perturbed ion (asterisk) and electron (open square) velocity along with the linear analysis result (dashed line) for $\lambda/r_{gi} = 1.0$. . . 43

2.26 Time development of the FGM is shown for positive (asterisks) and negative shear (open diamond) case. The dashed line shows the result obtained in the linear analysis. 44

2.27 Snapshots of the occupation rate for the ion (left column) and electron (right column) for the strong negative shear layer. 46

2.28 Time profile of the integrated mixing rate for (A) the ion and (B)the electron for the negative shear case (open diamond). For the comparison, the results obtained in the positive shear case are also shown in each panels (asterisks). The abscissa shows the time normalized by the factor λ/V_0 and the ordinate shows the integrated mixing rate normalized by the initial shear area $L_x\lambda$. . 47

3.1 IMF dependence of plasma sheet temperature (left) and density (right) as a function of the solar wind kinetic energy is shown. Adopted from Terasawa et al. [1997]. 50

3.2 The E-t diagram for omni-directional ions (bottom) and electrons (top) observed by Geotail spacecraft. Adopted from Fujimoto et al.[1998]. 51

3.3 An observation of LLBL by Geotail spacecraft on March 29 in 1995. From the top to the bottom panel shown are the absolute value and three vector components of the magnetic field, ion density and temperature, and the x component of the ion velocity. The vertical thick line indicates the boundary which separates the magnetosphere and the solar wind. 55

3.4 The growth rates of the K-H instability for different density profiles. The green line is the growth rate for the incompressible case with the discontinuous velocity profile for α=0.2. (eqn. (3.1)) 57

3.5 The eigen mode structure of the fastest growing mode for (A)$\alpha = 0.2$ and (B)$\alpha = 1.0$. The abscissa and the ordinate shows the x and the y coordinate normalized by the initial shear width λ . The color coded strength shows the power of the thermal pressure of the fastest growing mode. The arrows shows the corresponding perturbed and unperturbed velocity. 58

3.6 The time development of the FGM for (A)$\alpha = 1.0$ and (B)$\alpha = 0.2$. The abscissa shows the time normalized by λ/V_0 and the ordinate shows the power of the Fourier transformed thermal pressure whose mode number corresponds to the K-H instability. The dashed lines in the panels shows the growth rate calculated in the linear analysis in section 3.3 60

3.7 Number density profiles with flow vectors for $\alpha = 0.2$ are shown at a time (A) t $= 71.88\lambda/V_0$, (B) t $= 84.38\lambda/V_0$, (C) t $= 89.84\lambda/V_0$, and (D) t $= 156.25\lambda/V_0$. The abscissa and the ordinate shows the x and the y coordinate in the unit of the initial shear width, λ. The onset of secondary instabilities are recognized in (B) as zoomed-in the white frames. The mushroom like structure zoomed in (C) reminds the readers of the onset of the secondary Rayleigh-Taylor instability. 61

3.8 The energy spectra are shown in (A) for $\alpha = 0.2$, (B) for $\alpha = 0.6$, and (C) for $\alpha = 1.0$. Time evolution is expressed by the change in color of the line from blue to dark red. (D)-(F) shows the number density profiles with flow vectors which correspond to the energy spectra of the thick dark red lines (t=$156.25\lambda/V_0$) in (A)-(C), respectively. Spectra at $t = 156.25\lambda/V_0$ (thick dark red lines) are fitted with power functions (dash lines in (A)-(C)) and the powers are evaluated as -1.32, -1.38, -2.49, respectively. 63

3.9 Time evolution of (A) baroclinic term and (B) enstrophy in eq. (3.5) are shown for different α. The time and the both two terms are normalized by λ/V_0 and the grid number of the simulation domain ($N_x \times N_y$). Solid, dash-dotted, dash, dotted, and dash-3-dotted lines correspond to the result for $\alpha = 0.2, 0.3, 0.4, 0.6, 1.0$, respectively. 64

3.10 The snapshots of (A) Number density, (B) baroclinicity, and (C) vorticity taken at $t = 93.75(\lambda/V_0)$ are shown. 65

3.11 Comparison of the growth rate between the normal K-H and the secondary R-T instability. The asterisk shows the result for the secondary R-T instability obtained by the linear analysis. The open square shows the growth rate of the normal K-H instability. The solid line shows the analytical result of eq. (3.10). 68

3.12 Time profiles of the modes $k_x\lambda = 0.39 \sim 2.36$ are shown for the results of $\alpha = 0.2$ (red) and $\alpha = 1.0$ (black). 69

3.13 Macroscopic properties are shown for different α. The profile of V_x averaged over the x direction is fitted with a functional form of $0.5V_0\tanh((y-y_0)/\mu)$ with two free parameters of width μ and position y_0. Shown are the time evolution of (A) the width μ and (B) the position y_0 in the unit of the initial shear width λ. The second phases at t=$80\lambda/V_0$ in (A) and (B) for $\alpha = 0.2, 0.3$ correspond to the onset of turbulence and indicate that the turbulence effectively enhances the mixing of two media and the transport of dense fluid to the tenuous region. 70

3.14 Macroscopic properties for $\alpha = 0.2$ are shown for three numerical resolutions in the same format of Fig. 3.13. 71

3.15 Magnetic field profiles with flow vectors for br = 0.2 are shown at a time (A) t = $68.75\lambda/V_0$, (B) t = $87.5\lambda/V_0$, (C) t = $106.25\lambda/V_0$, and (D) t = $125.00\lambda/V_0$ in the same format of the Fig. 3.7. No development of the turbulence is confirmed in the absence of the stratification. 74

3.16 The time development of the FGM for (A)α = 1.0 and (B)α = 0.2 in the same format of the Fig. 3.6except that the ordinate shows the power of the y component of the Fourier transformed perturbed ion velocity. The dashed lines in the panels shows the growth rate calculated in the linear analysis in section 3.3 76

3.17 Number density profiles with contour lines of the electrostatic potential for $\alpha = 0.2$ are shown at a time (A) t = $49.72\lambda/V_0$, (B) t = $62.15\lambda/V_0$, (C) t = $111.88\lambda/V_0$, and (D) t = $194.75\lambda/V_0$ in the same format of the Fig. 3.7 . . . 78

3.18 (A)The orbit in the simulation domain, (B) the time development of the y coordinate and (C)the x coordinate, and (D)the orbit in a phase space are shown. The coordinate x and y are normalized by the initial shear width λ, the time is normalized by the parameter λ/V_0, and the velocity is in the unit of the speed of light. 79

3.19 Same profiles as shown in Fig. 3.18but for the electron. 80

3.20 The time profiles of the mixing rates for (A) the ion and (B) the electron in the same format of Fig. 2.9. In each panels cross(+), asterisk(*), and open diamond mark the result for $\alpha = 1.0, 0.2, 0.1$, respectively. 81

3.21 The time developments of the power of the waves whose mode number ranges from one(K-H mode, top left) to six(bottom right) are shown. The y component of the perturbed ion velocity is taken to be Fourier transformed in the x direction and then integrated in the y direction. 82

3.22 The mixing rate of (A) the ion and (B) the electron is snapshotted at $t = 66.3\lambda/V_0$ is shown in the same format of Figure 3.17. 83

3.23 The snapshots of (A) the absolute value of the electric field and (B) the electrostatic potential at $t = 66.3\lambda/V_0$ are shown in the same format of Figure 3.17. 84

3.24 The initial (left column) and the snapshot (right column) of the ion density profiles are shown for different initial shear widths λ/r_{gi}. The abscissa shows the y coordinate in the unit of ion gyro radius r_{gi} and the ordinate shows the ion number density. From the top to the bottom the results for $\lambda/r_{gi} = 1.0, 2.0, 4.0$ are shown which are obtained at the time $t = 59.67, 57.45, 49.72\lambda/V_0$, respectively. 85

3.25 The snapshot of the density profile which is similar to the bottom right panel of Fig. 3.24is shown in the same format of Fig. 3.24. The width of the density interface between the two horizontal arrows is estimated. 86

3.26 The time profile of the kinetic spectrum obtained by eq. (3.4) in the simulation for $\alpha = 1.0$ is shown. The abscissa shows the wave number in the x direction and the ordinate shows the time.The strength in color indicate the power of the wave. 87

3.27 The time profile of the kinetic spectrum in the simulation for $\alpha = 1.0$ is shown in the same format of Fig. 3.26. 87

3.28 Power spectrum of the x component of the electric field averaged in the interval $t = 50 \sim 199\lambda/V_0$. The solid line shows the result for $\alpha = 1.0$ and the solid red line shows the result for $\alpha = 0.2$. 88

3.29 Schematic view of the self-similar system obtained by the ideal MHD simulation. 89

4.1 Schematic view of the ion motions in the positive (left) and negative (right) shear layer. Adopted and modified from Fig. 7 in Cai et al.[1990]. 92

4.2 Number density profiles are shown in the right column. The left column shows the result obtained in the positive shear case for the comparison. Snapshots are taken from the top to the bottom at t=66.30, 99.45, and $165.75\lambda/V_0$. . . 95

4.3 The time developments of the wave amplitudes whose mode number ranges from one(K-H mode, top left) to six(bottom right) are shown in the same format of Fig.3.21. The black and red solid lines show the result for the positive and the negative shear case, respectively. 96

4.4 The time development of the mixing rate of (A) the ion and (B) the electron for the positive (cross) and the negative (open diamond) shear layers are shown in the same format of Fig. 2.9. 97

4.5 (A) The x component of the ion velocity and (B) the y component of the electric field are shown at a time $t = 72.93\lambda/V_0$, which are normalized by Alfvén speed defined in the region $y = +10\lambda$ and $V_A B_0/c$, respectively. The contour lines show the electrostatic potential. The cross-section profile of the y component of the electric field in the y direction averaged over the region from $x = 1.56\lambda$ to 3.13λ (solid black box) is shown in (C). 98

4.6 (A) Potential structures calculated from eqn. (4.12) for the case without velocity shear (black), the positive shear case (blue) and the negative shear case (red). (B) The potential profiles around the center of the velocity shear layer are zoomed in the right panel. 100

4.7 The time development of the occupation rate for (A) the positive and (B) the negative shear cases. Time proceeds from the left to the right. Four snapshots are taken at $t = 3.32, 6.63, 9.95, 13.26\lambda/V_0$. 102

4.8 The time development of the standard deviation calculated from eqn. (4.15). The standard deviation is normalized by the thermal ion gyro radius defined in the region y=+10 λ. 103

4.9 A sum of the ion and the electron mixing rate is snapshotted at (A)t = $53.87\lambda/V_0$ for the positive shear case and (B) t = $59.67\lambda/V_0$ for the negative shear case. For comparison, number density profiles are shown in (C) and (D) for each simulation runs. 105

B.1 Initial setting for the linear analysis. From the top to the bottom panel shown are (A)the z component of the magnetic field, (B)the sum of ion and electron thermal pressure, and (C)the ion density with respect to the y coordinate. . 121

B.2 Growth rate of the R-T instability in the two fluid MHD regime (solid red line). The abscissa shows the wave number in the x direction normalized by the initial boundary width and the ordinate shows the growth rate normalized by a factor λ/V_A. Along with the two fluid MHD result ideal (black) and the analytic solution of eq.(B.2) are shown. 122

List of Tables

2.1 Plasma parameters used in the simulations in this chapter. 21

3.1 Plasma parameters used in the simulations in this chapter. 76

4.1 Plasma parameters used in the simulations in this chapter. 93

Acknowledgments

The author wishes to express his unbounded gratitude to Prof. Masahiro Hoshino for his continuous encouragement and guidance during the doctoral course at the University of Tokyo. The author has learned many precious things from him, especially thinking and explaining the problems in a logical way and the attitude of facing physics. Without his shrewd and appropriate guidance, this dissertation could not be completed.

Prof. Toshifumi Mukai at Institute of Space and Astronautical Science (ISAS) should also be acknowledged. The author had acquired the basic magnetospheric physics under his supervision in the master course. From the precious experiences of discussions with him the author had learned the way of explaining the physics with easy words, which is still valuable in the research activities.

The author also wishes to express his special thanks to Prof. Toshio Terasawa and Dr. Akira Miura at the University of Tokyo. Their experienced advise to the problems of the K-H instability always helped and encouraged the author to complete this dissertation. Dr. I. Shinohara at ISAS, Dr. T. Yokoyama at the University of Tokyo and Prof. H. Takabe at the Osaka University are also greatly acknowledged for their helpful comments during the course of this work.

The computational resources for this work had been supported by Fujitsu VPP5000 at the Nagoya University and VPP800 at ISAS and they are also acknowledged.

Many supports are given by the colleagues at the University of Tokyo and ISAS. Having time with them had always encouraged and contributed to the completion of the dissertation. The author especially thanks to H. Jin, Dr. S. Yokota, M. Nishino, H. Tanaka, and A. Ihara.

Lastly, the author would like to express his deep thanks to his parents for their financial and mental supports that enable the author to continue his work in the doctoral course and to complete this dissertation.

Abstract of the Dissertation

Turbulent Mixing and Transport of Collision-less Plasmas across a Stratified Velocity Shear Layer

by

Yosuke Matsumoto

Doctor of Philosophy in Earth and Planetary Sciences

University of Tokyo, Tokyo, 2004

Since Lord Kelvin[1871] and Helmholtz[1868] firstly pointed out that a relative motion of two media causes an unstable wave at the boundary between them, many theoretical and experimental efforts have been devoted to understand its property over the last century. And today, the growing wave at such an interface is well known as Kelvin-Helmholtz (K-H) instability after the names of the first two contributors. Because of its universal property, the applications are involved in diverse areas; the K-H instability appears not only in geophysical phenomena but also in the space and astrophysical phenomena. Among a numerous applications of the K-H instability the present dissertation mainly focuses on the interaction between the solar wind and the earth magnetosphere.

High conductivity of plasma around the earth justifies the frozen-in condition, and thus the earth's intrinsic magnetic field can shield from the solar wind plasma directly penetrating into the earth atmosphere. However, the evidences that indicate the existence of the solar wind plasma inside the earth magnetosphere give us long standing problems. Especially, the indication of the direct penetration of the solar wind plasma across the low latitude boundary at the flanks of the magnetosphere, that cannot be explained by the established reconnection (open magnetosphere) model, still requires a new theoretical model. In this decade, the low latitude boundary therefore has been a subject of mass transport from the solar wind to the earth magnetosphere and many theoretical approaches have attempted to explain it. In this context, the K-H instability, which is considered to be unstable at that region, has been a

candidate for this model because its non-linear development is characterized by mixture of two media. The simple vortex evolution, however, cannot explain the broad mixing area, and another mechanism is needed for this kind of issues.

In this study, I again shed a new light on the K-H instability by showing that it can transport the solar wind mass in the widely spread region by computational manners. The main results of the dissertation are summarized as follows.

0.1 Cross-field diffusion across a homogeneous velocity shear layer

Mixing process of both the ion and electron across a transverse magnetic field by the K-H instability is studied by using full particle simulation. The simulation results indicate that the mixing area increases with time as the K-H develops. The most mixed regions for both the ion and electron are restricted within the interface at which two plasma populations face. The increase in mixing area is mainly contributed from the stretched path length of the interface, while the cross-field diffusion in the direction perpendicular to the interface indicates that the electrons diffuse to follow the ions. Electrostatic waves induced by thermal fluctuation scatter electrons and the interface of two electron population is deformed into fine structures to fill up the ion mixing area.

0.2 Turbulent mixing and transport across a stratified velocity shear layer

The two-dimensional simulation of the K-H instability in a non-uniform density medium shows strong development of turbulence through non-linear instabilities. Ideal MHD simulation results indicate that the difference in density between two media plays a crucial role on the fast turbulent mixing and transport. The onset of the turbulence is triggered not only by the secondary K-H instability but also by the Rayleigh-Taylor (R-T) instability at the density interface inside the normal K-H vortex. The secondary R-T instability alters macroscopic structure by transporting dense fluids to tenuous region, while the secondary K-H instability

is just a seed for the turbulence. Full particle simulation is also conducted and reproduces the similar result of the ideal MHD's except that the secondary R-T instability grows during the first turning over motion of the normal K-H instability. Strong electrostatic field caused by the secondary R-T instability scatters ions and deforms electron density interface and as a result the mixing area increases fast and extends spatially as compared to the result in the uniform density case.

0.3 Dawn-dusk asymmetry in the non-linear development of the K-H instability

The full particle simulations of the K-H instability in the stratified shear layer show the asymmetry in the non-linear development between the positive and the negative velocity shear cases. In the positive shear case the onset of the secondary instability, which leads the system to the turbulence, appears in the early non-linear stage of the K-H instability. On the other hand, the apparent transition from the laminar to the turbulent flows does not appear in the negative shear case. This asymmetry is interpreted as a result of an asymmetry in the finite Larmor radius (FLR) effect of the ion at the outer edge of the vortex. The difference in the FLR effect appears at the newly induced velocity shear layer in the non-linear stage of the K-H instability. In the positive shear case ($\mathbf{B_0} \cdot \mathbf{\Omega_0} > 0$) the outer edge of the vortex in the negative y region, where is R-T unstable, becomes a positive shear. The FLR effect weakly stabilize the onset of the secondary instability, particularly the R-T instability. On the other hand, in the negative shear case ($\mathbf{B_0} \cdot \mathbf{\Omega_0} < 0$), the R-T unstable region becomes a negative shear layer that increases effectively the ion gyro radius. The enhanced FLR effect strongly stabilizes the onset of the secondary R-T instability.

The present onset mechanism and the formation of the broad mixing layer give the new understanding of the mass transport mechanism from the solar wind via the low latitude boundary.

CHAPTER 1

General Introduction

1.1 Kelvin-Helmholtz instability

An interface between two media flowing relative to each other is unstable and the resulting growing wave is well known as Kelvin-Helmholtz (K-H) instability (Helmholtz, 1868; Kelvin, 1871). Since the non-linear evolution of the K-H instability is characterized by a momentum exchange and mixing of two media, it has been studied for a long time and applied to a variety of fields in extensive scales of phenomena. A wind-induced water wave is a general representative phenomenon that can be seen anywhere. When wind flows over a sea surface with speed above 650 cm/s, Kelvin[1871] has shown that the sea surface is unstable. And then, the sea surface eventually develops to a large amplitude wave as shown in Figure 1.1. The K-H instability is a main contributor for the atmospheric and oceanic mixing processes

Figure 1.1: Ukiyoe. Adopted from Hokusai Katsushika, Fugaku Sanjurokkei [1831]

(Fritts et al., 1996). Actually, one may find a K-H vortex growing when one looks up in the sky as shown in Figure 1.2, which indicates the development of the K-H vortex at the cloud surface sheared with the fast wind flows. While the K-H instability has been studied

Figure 1.2: A picture of clouds where the K-H seems to develop. The picture is adopted from the web site Houze's Cloud Atlas (http://www.atmos.washington.edu/gcg/Atlas/).

extensively for the applications to the geophysical phenomena, the plasma physics have also developed the understanding of the role of the K-H instability for the applications to some experimental, space and astrophysical phenomena. Sheared $\mathbf{E} \times \mathbf{B}$ drift (K-H) instability inhibits the turbulent transport in tokamaks of laboratory plasmas (Tajima et al., 1991). Planetary phenomena such as the formation of the low latitude boundary layer (LLBL) at the earth magnetosphere (Axford and Hines, 1961; Sckopke et al., 1981) and the magnetic flux ropes observed in the Venus ionosphere (Russell and Elphic, 1979; Thomas and Winske, 1991) are considered to attribute to the K-H instability excited by the shocked solar wind plasmas. Recently, the global simulation modeling the interaction between the solar wind and the Venus ionosphere reproduced the excitation of the K-H instability (Terada et al., 2002, Fig. 1.3). The recent observational and the computational studies reveal the deformation and/or the disruption of the galaxy cluster (Fujita et al., 2002) and the astrophysical jets (Norman et al., 1982; Hardee et al., 1997; Lobanov et al., 2001) by the K-H instability which is excited by the interaction with the intergalactic medium (Fig. 1.4).

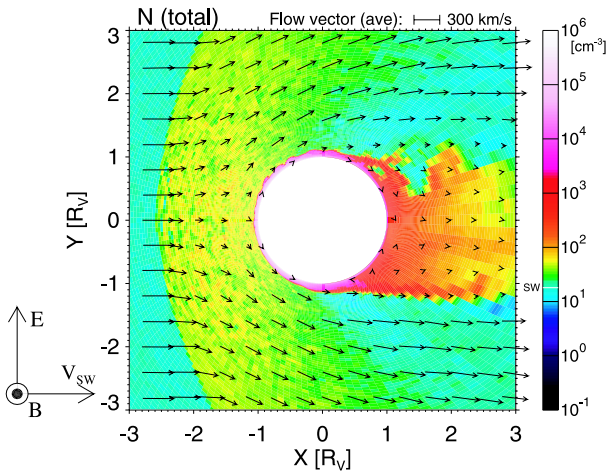

Figure 1.3: The simulation result which models the global interaction between the solar wind and the Venus ionosphere. The color intensity shows the number density of plasmas. The picture is cited from Figure 4 in Terada et al.[2002].

1.2 Sun-Earth connection

Among the numerous applications of the K-H instability, the present dissertation is especially focusing on the interaction between the shocked solar wind and the earth magnetosphere. High energy plasmas ejected from the sun, which is called "**solar wind**", travels the interplanetary space and arrives at the earth with forming a shock at the day side front of the earth ("**bow shock**") as a supersonic flow interacts with an obstacle. Since the solar wind plasma is a high conductive medium, the earth's magnetic field is confined into a cavity generated in the solar wind, which is called "**magnetosphere**" (Fig. 1.5). Hence, the earth dipole magnetic field shields the energetic particles of the solar wind from directly penetrating into the earth and it therefore guarantees our safe and healthy day-life. The past great efforts of the grand-based and the in-situ observations, however, have revealed that the dipole magnetic field does not perfectly protect against the solar wind plasma. It manages to get inside the magnetosphere. How does it get in? Where and what is the loophole? Numerous researchers on space plasma physics have challenged to answer these questions. In this context, in 1961, two major models on the interactions between the solar wind plasma and the earth magnetosphere caused a paradigm shift. The one is so called

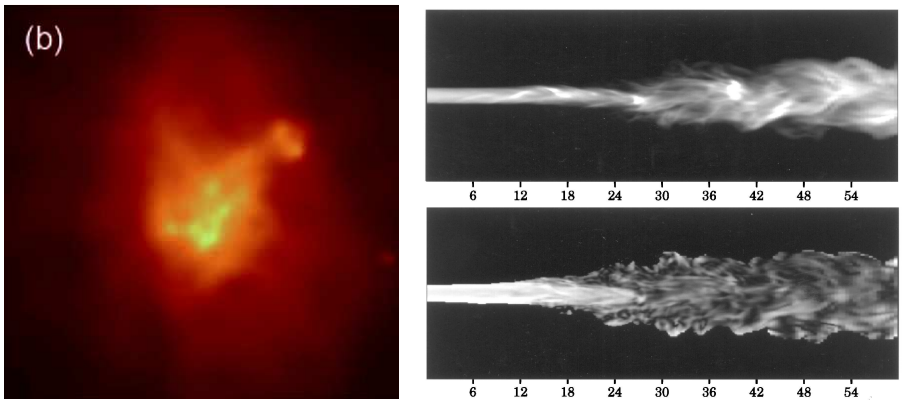

Figure 1.4: Astrophysical phenomena where the K-H instability seems to operate. The left panel shows the X-ray image of the core of the galaxy cluster observed by *Chandra*. The image is cited from Figure 1(b) in Fujita et al.[2002]. The right panel shows the simulation result of the astrophysical jet performed by Hardee et al.[1997].

"**open magnetosphere**" model proposed by Dungey[1961] (Fig. 1.6, left panel) and the other is so called "**closed magnetosphere**" model by Axford and Hines[1961] (Fig. 1.6, right panel).

The former model incorporates the violation of the frozen-in condition, which permits a finite resistivity and thus results the reconnection of the earth's northward dipole magnetic field lines with the southward interplanetary magnetic field (IMF) lines at the day side magnetosphere. Open magnetosphere by the reconnection results the effective transport of the solar wind plasma to the earth magnetosphere. The reconnected magnetic field lines transport the solar wind plasma to the night side of the magnetosphere where the draped field lines again reconnects. Eventually, a part of the plasmas originated from the solar wind gain the magnetic field energy and rushes toward the earth. Those plasmas are considered to be an origin of "**Aurora**". This closure of the energy and the mass trading with the solar wind well explains the in-situ observations and has became a standard model in the case of southward IMF.

On the other hand, the latter model suggested a rather quiet interaction incorporating a viscous interaction along the flanks of the magnetosphere, which could permit solar wind mo-

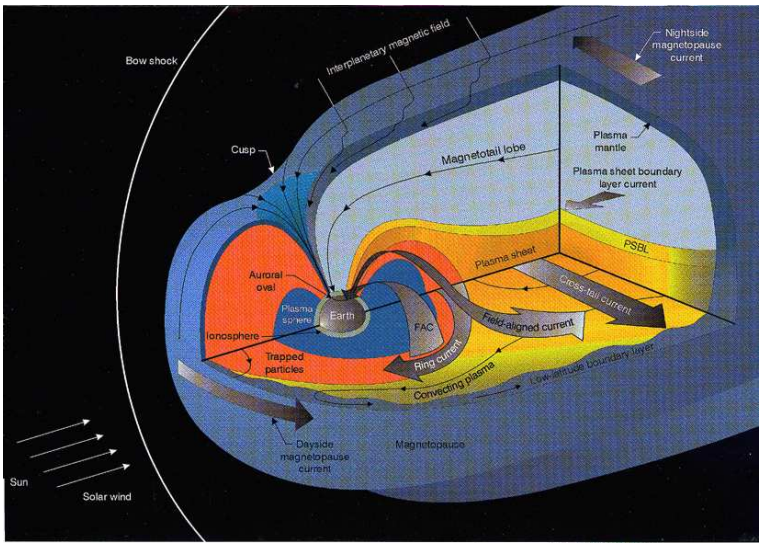

Figure 1.5: Schematic view of the earth magnetosphere interacting with the solar wind (picture by J. Burch, Southwest Research Institute, San Antonio, USA).

mentum to diffuse onto closed magnetospheric field lines. The resulting tailward convection flow would eventually be closed by an earthward returning flow in the center of the tail. The solar wind plasma pasts by the flanks of the magnetosphere across which the flow velocity is sheared. This situation is a favorable condition for the excitation of the K-H instability, and thus the K-H instability has been a major candidate for the mechanism of the viscous interaction along the flanks of the magnetosphere. This model possibly explains the transport of the solar wind momentum into the earth magnetosphere but does not suggest any mass transport mechanisms. Therefore, the K-H instability has been considered to be just a backseat player and support the crucial player ,which instead the explosive phenomenon of the reconnection plays, on the stage of the Sun-Earth connection model. The recent in-situ observations, however, have revealed that there exists the region of closed field lines filled with the mixed plasmas which consist of the solar wind and the magnetospheric origins. That region is called "**Low latitude boundary layer (LLBL)**" (Sckopke et al., 1981; Phan et al., 1997; Fujimoto et al., 1998). At the same time the in-situ observations which indicate the vortex motions generated by the K-H instability in the LLBL have been reported (Hones et al., 1981; Ogilvie and Fitzenreiter, 1989; Seon et al., 1995; Fairfield et al., 2000).

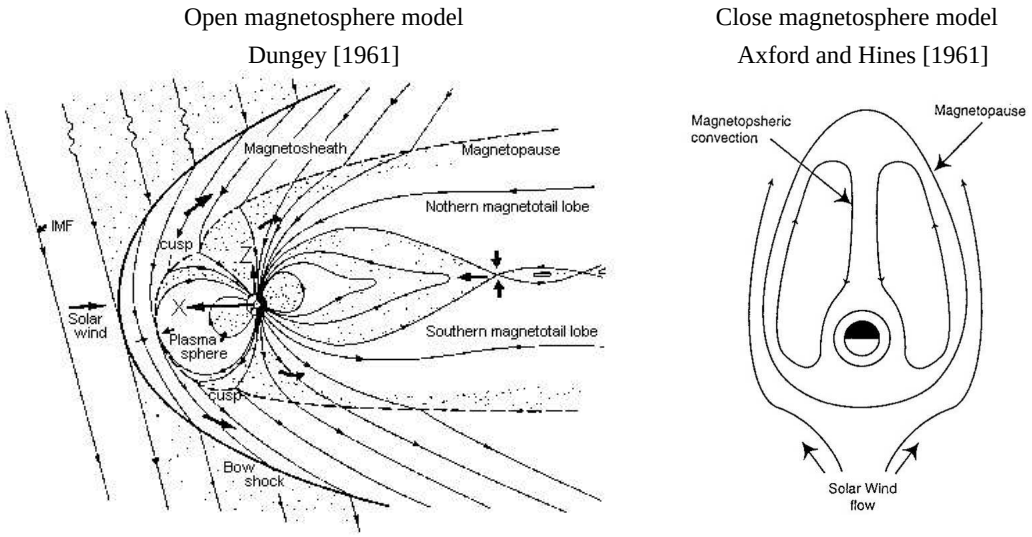

Figure 1.6: Left panel: Open magnetosphere model proposed by Dungey[1961]. The figure shows the cross section of the magnetosphere in the noon-midnight meridian plane (Adopted from Bothmer[1993]). Right panel: Close magnetosphere model proposed by Axford and Hines[1961]. The figure shows the cross section of the magnetosphere in the equatorial plane which is viewed from the north.

From these observations the K-H instability have recently been related with another mass transport mechansims across the LLBL. Even though many observational evidences have indicated that the K-H instability also plays a crucial role on the mass transport, theoretical supports have not been given until now.

1.3 Theoretical and computational approach to K-H instability

Numerous theoretical and computational studies have been devoted to understand the linear and non-linear properties of the K-H instability in relation to the magnetospheric interaction.

Since Chandrasekhar[1961] revealed the importance of the orientation of the magnetic field with respect to the ambient flow on the linear growth of the K-H instability, numerous studies have been devoted to understand the linear properties of the K-H instability (Sen, 1964; Southwood, 1968; Ong and Roderick, 1972; Pu and Kivelson, 1983). Miura and

Pritchett[1982] finally established the linear theory for arbitrary conditions, in which they quantitatively showed that a magnetic field component parallel to the flow is found to be stabilizing effect as a surface tension force acts in a hydrodynamic case. Hence the orientation of the magnetic field with respect to the flow is an important factor for the MHD application. In the earth magnetosphere the solar wind plasma is sheared at the magnetospheric boundary. At the high latitude boundary the solar wind direction is almost parallel to the magnetic field called "**tail lobe**" region. The strong parallel magnetic field limits the unstable condition of the K-H instability and it is unlikely a K-H unstable region. On the other hand, the low latitude boundary is a favorable condition for the excitation of the K-H instability since the strong northward dipole magnetic field is perpendicular to the ambient solar wind flows.

Non-linear behaviors have been explored by means of computer simulation. Miura [1984,1992] examined the two-dimensional ideal MHD simulation of the K-H instability and showed that the Reynolds stress, which transfers the momentum across the shear layer, increases with time. If one permits a larger simulation domain the fastest growing mode inversely cascades to the longer wave modes. This inverse cascade is characterized by the vortex pairing and the emergence of a large isolated vortex (Wu, 1986; Miura, 1997; Miura, 1999). During the coalescence of the vortices the Reynolds stress increases and the momentum is more effectively transported across the boundary layer in a larger simulation domain. Those MHD simulation approaches have revealed that the momentum transport across the shear layer by the K-H instability can satisfy the requirements of the viscous like interaction as suggested by Axford and Hines[1961].

The recent progress in the computational ability enables the kinetic particle simulation to follow the non-linear development and seeks out a unique feature in a collision-less plasma. Hybrid simulations which treat the ion as a particle with the charge neutralizing electron fluid and full particle simulations have been conducted to clarify mixing and transport mechanisms of collision-less plasmas by the K-H instability (Pritchett and Coroniti, 1984; Terasawa et al., 1992; Thomas and Winske, 1993; Cai et al., 1993; Fujimoto and Terasawa, 1994; Fujimoto and Terasawa, 1995; Wilber and Winglee, 1995). Hybrid simulations (Terasawa et al., 1992; Fujimoto and Terasawa, 1994) showed that the finite Larmor radius effect of the ions enhances

the mixing of plasma anomalously and suggested an effective mixture by a K-H vortex. Thomas and Winske [1993] also reported the hybrid simulation study of a in-homogeneous case and showed that the isolated structures on the order of the ion gyro radius are formed which can across the boundary in either direction. They firstly suggested the mass transport of the solar wind plasma by the K-H instability, although the physical mechanism of the generation of the plasma blobs is still remained unsolved (see also, Huba, 1996b). Wilber and Winglee[1995] demonstrated the full particle simulation of the K-H instability modeling the dawn and the dusk LLBL. They pointed out a dawn-dusk asymmetry in the non-linear development of the K-H instability which showed the vortex formation in the dusk side and the tongues of magnetosheath plasma penetrating into the magnetosphere in the dawn side. The asymmetry increases with decreasing the initial velocity shear width. This feature is also reported by Huba[1996b] based on the MHD simulation including a finite Larmor radius (FLR) effect of the ion. Hence the asymmetry should be attributed to the FLR effect of the ion, but the detailed physical mechanism has been remained ambiguous.

It is quite recently that the combination of the magnetic reconnection and the K-H instability has been incorporated in two- (Nykyri and Otto, 2001) and three- (Knoll and Brackbill, 2002) dimensional ideal MHD simulations. Nykyri and Otto[2001] showed that the magnetic reconnection is triggered in the non-linear stage inside the K-H vortex. The finite component of the magnetic field parallel to the flow generates the multiple current sheets inside the vortex and the magnetic reconnection takes place. As a result, the detached high density plasma is transported from the magnetosheath. They suggested this mechanism as a new transport process by the combination of the K-H instability and the magnetic reconnection, while the diffusive property, which is often observed in the LLBL, could not be reproduced.

In spite of the great efforts on the mass transport across the velocity shear layer, only a few things have been understood and the formation mechanism of the LLBL is not clearly understood. In this context the present dissertation again sheds the new lights on the Kelvin-Helmholtz instability by showing that it must play a crucial role not only as a momentum messenger but also as a mass carrier in theoretical and computational manners. What

is newly found in this dissertation is that the strong non-linear coupling of the various instabilities within a K-H vortex triggers the onset of turbulence and the transport of dense medium to the tenuous region in the spatially extended area. In addition, the electron mixing process is investigated for the first time as well as the ion's in the course of the turbulent mixing. Even though the model is quite simple as compared to the actual situation in the magnetosphere, the fast and spatially extended mixing process of collision-less plasma shown here is quite noteworthy.

CHAPTER 2

Cross-field diffusion across a homogeneous velocity shear layer

To understand the basic linear and non-linear behavior of the K-H instability, numerical and computational approach are used to examine for a homogeneous background field case throughout this chapter.

2.1 Introduction

2.1.1 Magneto-hydro dynamic Kelvin-Helmholtz instability

Early theoretical efforts have been devoted to define the linear properties of the K-H instability since the velocity shear boundary was found to be unstable by Helmholtz[1868] and Kelvin[1871]. Linear theories identified the necessary conditions for the instability, the mode structure, the growth rates and the wave number dependence of the K-H instability for various mean flows of hydrodynamic phenomena (Helmholtz, 1868; Kelvin 1871; Chandrasekhar 1961). For the sake of simplicity, let now the velocity vary discontinuously, the fluid is incompressible for a homogeneous fluid. In this circumstance it is always unstable with respect to the K-H instability as long as the velocity difference exists. The growth rate is derived as

$$\gamma = \mathrm{k_x}(\mathrm{U_1} - \mathrm{U_2}), \tag{2.1}$$

where, $\mathrm{U_1}$ and $\mathrm{U_2}$ denote the velocity of the two media moving relatively each other. Compressibility, a finite boundary width and a surface tension force must act against the instability.

For the experimental plasma, space and astrophysical applications the K-H instability must refer to magneto-hydro dynamics (MHD) in which magnetic field comes into play. In the early era, most of the investigations assumed a zero thickness velocity shear boundary in an incompressible plasma. For example, the linear stability results are given also by Chandrasekhar[1961], in which there is two points to be noted. If the plasma flow is perpendicular to the magnetic field (transverse case), the magnetic field has no effect on the instability and it is always unstable for all velocity jumps just as seen in hydrodynamics. If the plasma flow is parallel to the magnetic field (parallel case), however, it acts for the stabilization. The K-H mode is completely stabilized if the total velocity jump is less than twice the Alfvén velocity. Physically, the tension force of magnetic field lines inhibit the growth of the K-H mode as the surface tension force acts in the hydrodynamic case. Hence the orientation of the magnetic field with respect to the flow is an important factor for the MHD application. In the earth magnetosphere, whose interaction with the solar wind is the main topic in this dissertation, the solar wind plasma is sheared at the magnetospheric boundary (magnetopause). At the high latitude boundary the solar wind direction is almost parallel to the magnetic field which is called tail lobe region. The strong parallel magnetic field, which is on the order of ten nano teslas, limits the condition of the excitation of the K-H instability and it is unlikely an K-H unstable region. On the other hand, the low latitude boundary is a favorable condition for the excitation of the K-H instability since the strong northward dipole magnetic field is perpendicular to the ambient solar wind flows. That is the reason why the author is motivated to put the target on the low latitude boundary and to focus on mainly the transverse case throughout the present dissertation.

Non-linear development of the K-H instability in a MHD regime in the view of the magnetospheric interaction has been investigated by means of numerical simulation (Miura, 1984; Wu, 1986, Miura, 1995). Miura[1984] quantitatively demonstrated that the Reynolds stress, which increases in the course of the non-linear development the K-H instability, acts as an anomalous viscosity, which becomes comparable to the Bohm diffusion and satisfies the requirement in Axford and Hines's[1961] hypothesis for a viscous-like interaction. Wu[1986] and Miura[1997,1999] revealed that the larger simulation system allows more effective mo-

mentum transfer across the boundary layer. The inverse cascade of the wave modes produces the vortex paring that results one large vortex. During the coalescence of the vortices the momentum is effectively transported across the boundary due to the large Reynolds stress. By these investigations of the non-linear behavior the viscous interaction by the K-H instability which Axford and Hines[1961] proposed for the first time have been accepted as a possible mechanism for the momentum transport of the solar wind.

2.1.2 Kinetic treatments on the Kelvin-Helmholtz instability

Those magneto-hydro dynamical approach is valid only when

- the characteristic spatial scale is much larger than that of the ion gyro radius and the inertia length, and
- the characteristic time scale is much slower than that of the ion gyro and plasma frequency.

These conditions are not always valid, especially at the discontinuous boundary, such as, the magnetopause. The thickness of the magnetopause boundary has been explored by the in-situ observations. Berchem and Russell[1982] demonstrated the simultaneous observations by ISEE 1 and 2 spacecrafts (Russell and Elphic, 1978) of the magnetopause crossings. Statistical analysis showed that the thicknesses of the magnetopause are concentrated in the interval from 400 to 1000 km which is only a few times thicker than the ion gyro radius. Thus the validation of the MHD approach for understanding of the K-H development at such a thin boundary is questionable.

In this context, a kinetic approach to the K-H instability is needed and a number of challenges have been devoted for further understanding of the K-H instability in a kinetic regime. Fujimoto and Terasawa[1991] showed the ion inertia effect on the linear growth of the K-H instability by including the hall and the electron pressure term in the generalized Ohm's law. They concluded that although the growth rates are only slightly affected by the ion inertia effect the structures of the eigen mode become highly different from the ideal

MHD case. Ganguli et al.[1988] developed a nonlocal kinetic theory in a non-uniform dc electric field. In a small wave number range the kinetic dispersion relation recovers the K-H instability. In a large wave number regime, on the other hand, they found another branch of the unstable mode they named ion-cyclotron (IC) like instability, whose unstable domain is clearly distinctive from the K-H mode. This study was extended by Nishikawa et al.[1988] by showing the non-linear development of the IC like mode by using the kinetic electrostatic particle simulation. In the early 90's the progress in computational ability enables the researchers to follow the long time evolution of the K-H instability with a kinetic particle simulation. Terasawa et al.[1992] showed, for the first time, anomalously fast ion mixing within a K-H vortex with using a hybrid simulation. By treating an ion as a particle followed by electron neutralizing fluids they revealed that the ions are scattered by a rotational part of the electric field perturbation and the ions are mixed anomalously fast. Fujimoto and Terasawa[1994] followed and extended Terasawa et al.[1992] and showed the similar result but their interpretation is that the enhanced ion mixing takes place by the ion scattering at the hyperbolic point in the shrinking phase of the K-H vortex.

By those kinetic treatments, although the unique properties of the K-H instability in a collision-less plasma have became clear, the role of electron dynamics on the K-H instability has remained ambiguous: How can the electrons strongly tied to the transverse magnetic field follow the scattered ions? Do the electrons inhibit or enhance the ions scatter across the magnetic field? The straightforward problems have remained unsolved until now. To understand fully the evolution of the K-H instability in the view point of the mixture of the collision-less plasmas, numerical and computational studies including the dynamics of electrons are conducted in this chapter.

2.2 Linear analysis

In the early era, studies on the linear stability had been done with a discontinuous velocity profile in the incompressible (Chandrasekhar, 1961) and compressible plasma (Sen, 1964; Southwood, 1968; Pu and Kivelson, 1980), and with a finite thickness of the velocity profile

in the limited Mach number (Ong and Roderick, 1972) until Miura and Pritchett[1982] established the linear properties of the K-H instability for a hyperbolic tangent velocity profile in a compressible plasma for the arbitrary direction of the wave number with respect to the ambient magnetic field. For the kinetic treatment, Fujimoto and Terasawa[1991] showed the ion inertia effect on the linear growth of the K-H instability. Based on their results the linear analysis with the two fluids MHD equations including the electron mass is examined to understand the modification of the linear growth rate by the electron inertia.

The growth rates and the corresponding eigen mode structures are obtained by solving a set of two fluid MHD and Maxwell equations as an eigen value problem (Appendix A). The initial conditions and parameters used in the analysis are

- $\mathrm{V_{xs}} = \mathrm{V_0}/2 \tanh(\mathrm{y}/\lambda)$,
- $\mathbf{B} = (0, 0, \mathrm{B_0})$,
- $\mathrm{P} = \text{constant}$,
- $\mathrm{V_0}/\mathrm{V_A} = -1.0$,
- $\beta_{\mathrm{ion}} = \beta_{\mathrm{electron}} = 0.15$,
- $\omega_{\mathrm{ge}}/\omega_{\mathrm{pe}} = 0.35$,
- $\lambda/\lambda_{\mathrm{i}} = 1.0$

where the subscript 's' denotes the particle species, ion and electron, and $\mathrm{V_0}$, V_A, β, ω_{ge}, ω_{pe}, and λ_{i} denote a jump in velocity across the shear layer, Alfvén speed, plasma beta, electron gyro frequency, electron plasma frequency, and ion inertia length, respectively. The fourth condition guarantees the flows are sub-magnetosonic everywhere in the simulation domain and the fast shock at the edge of the vortex will not be formed (Miura, 1984). These parameters are chosen for the adaption to the simulation in the remaining part of this chapter.

Figure 2.1 shows the growth rate with respect to the wave number in the x direction for a various mass ratio of ion's to electron's which varies from 16 to 144. The solid line shows the

result based on the ideal MHD equations. As seen in Fujimoto and Terasawa[1991], a finite

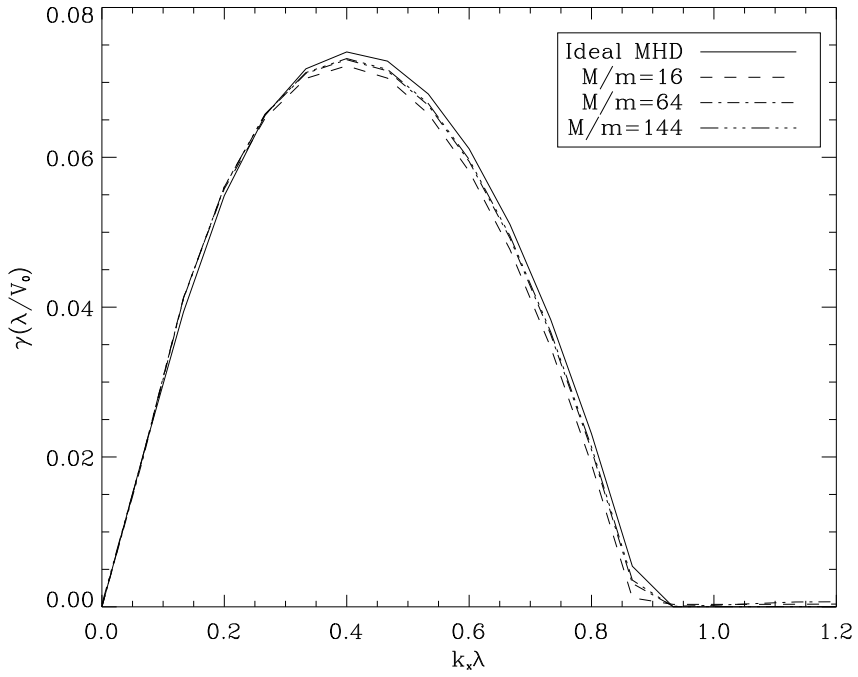

Figure 2.1: The growth rates of the K-H instability are shown for various mass ratios, 16(dash), 64(dash-dot) and 144(dash-three dots) along with the result for the ideal MHD case (solid). The abscissa shows the wave number in the x direction normalized by the initial shear width and the ordinate shows the growth rate normalized by the factor λ/V_0.

electron inertia also only slightly affects the growth rate of the K-H instability. Figure 2.2 shows the eigen mode structure of the perturbed ion thermal pressure of the fastest growing mode (FGM, Miura and Pritchett, 1982) for the mass ratio (A)16, (B)64, (C)144 and the corresponding result of (D)ideal MHD's. The white arrows indicates the vector plot of the ion velocity which is a sum of perturbed and unperturbed velocity component. The color intensity indicates the power of the mode and the abscissa and the ordinate shows the x and y coordinate in the unit of the initial shear width. Although the strong modification of the eigen mode structure by the ion inertia effect was reported in Fujimoto and Terasawa[1991], the present two fluid MHD analysis exhibits little difference from the ideal MHD's eigen mode structure.

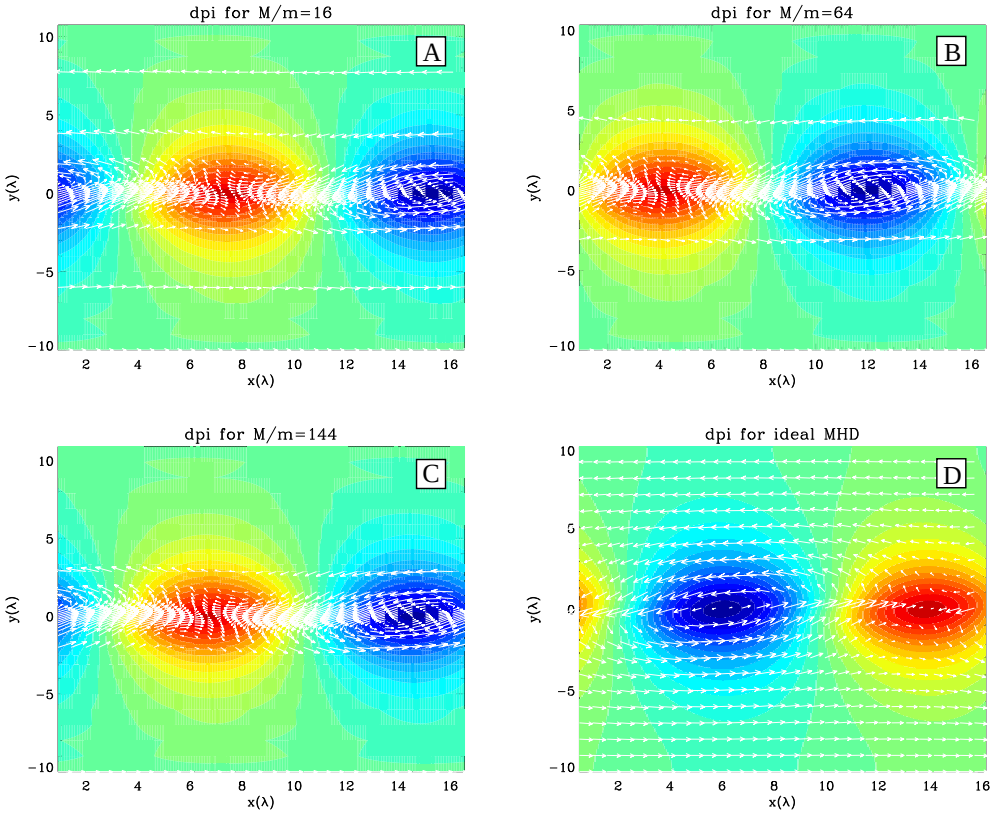

Figure 2.2: Eigen mode structures of the perturbed ion thermal pressure of the FGM for the mass ratio (A)16, (B)64, (C)144, and (D)the ideal MHD result. The color intensity indicates the power of the mode and the abscissa and the ordinate shows the x and y coordinate in the unit of the initial shear width. Perturbed and unperturbed velocity components are also added on the figure with the vector plot of the white arrows. (Non uniform intervals between the arrows in the y direction shown in (A)-(C) are due to the nonuniform grids adopted in those calculations.)

As a conclusion of the linear analysis, the electron inertia effect does not significantly affects both the linear growth rate and the eigen mode structure of the K-H instability even though the initial shear width is comparable to the ion inertia length.

2.3 Non-linear development of K-H instability

Non-linear development of the K-H instability is characterized by a momentum exchange and a mixing of two media. While ion dynamics in the mixing process has been studied by Terasawa et al.[1992] and extended by Fujimoto and Terasawa[1994] in which the finite ion Larmor radius effect anomalously enhances the mixing rate, the process how the electron, which is strongly tied to the transverse magnetic field, can trance the ion has been remained ambiguous. In this section the mixing process of collision-less plasma during the non-linear development of the K-H instability is explored by means of full particle simulation, which fully solves ion and electron dynamics along with the electric and magnetic field (Birdsall and Langdon, 1991; Hoshino, 1986).

2.3.1 Initial conditions of simulations

The schematic view of the initial setting of the simulation is shown in Figure 2.3. The x component of the velocity is sheared in the y direction. The uniform magnetic field is oriented in the z direction and thus the thermal pressure is uniformly set in the simulation domain. Particles are uniformly distributed in the simulation domain by using a cumulative distribution function (Birdsall and Langdon, 1991) so that Gauss' law

$$\begin{aligned} \nabla \cdot \mathbf{E} &= \frac{\partial \mathrm{E_y}}{\partial y} = \frac{\partial}{\partial y}\left(\frac{\mathrm{V_x(y)B_z}}{c}\right) \\ &= 4\pi q(n_i - n_e) \end{aligned} \tag{2.2}$$

is satisfied.

Choosing the number of particles per cell determines the balance between the computational resources and the accuracy of the calculation. We have tested the effect of the number of particles on the evolution of the K-H instability. Figure 2.4 shows the time development

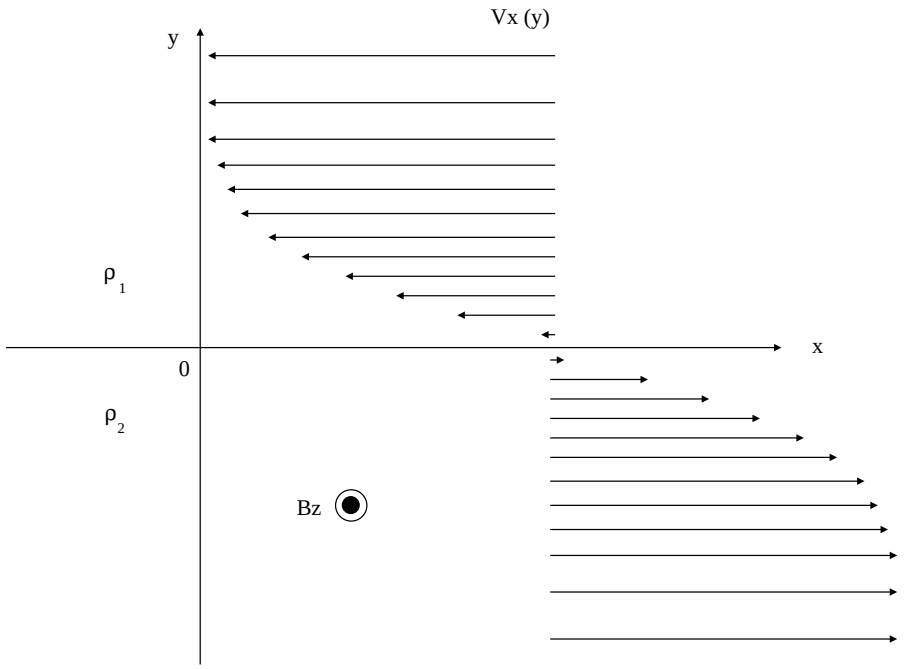

Figure 2.3: The initial setting of the simulation

of the fastest growing mode for various number density. From Figure 2.4, the calculations with more than 128 particles per cell almost express the same profile of the FGM. Therefore we take N=128 in the following results unless otherwise specified.

We take a grid size which corresponds to twice the Debye length for relatively thick shear cases ($r_{\rm gi}/\lambda = 2.0, 4.0$) and to the Debye length for a thin shear case ($r_{\rm gi}/\lambda = 1.0$). Mass ratio of the ion (M) to the electron (m) is set 16 throughout the paper due to the limited computational resources.

Plasma parameters used in the following simulations are basicly similar to that shown in section 2.2 except that the initial shear width, the orientation of the flow (sign of V_0), and the number of particles per cell are changed in the following subsections. The parameters are summarized in Table 2.1.

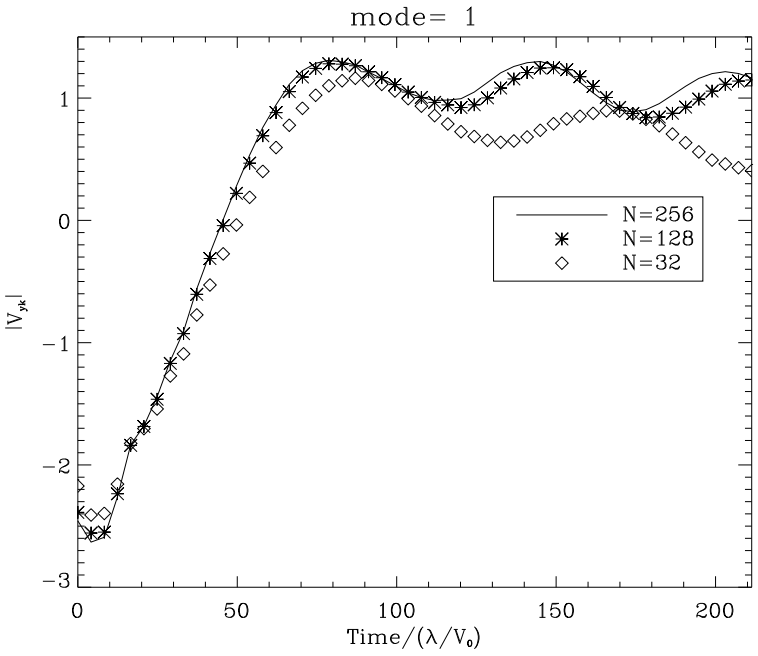

Figure 2.4: The effect of the number of particles per cell on the evolution of the K-H instability. The figure shows time development of the y component of the perturbed ion velocity, whose mode number corresponds to the FGM. The results are shown for $N = 32$ (open diamond), $N = 128$ (asterisk), and $N = 256$ (solid line).

2.3.2 Mixing rate

To quantitatively deal with the mixing process, a quantity, mixing rate, is defined as follows. Particles which are initially located in the region y $>$ 0 are numbered 1. Then as the simulation proceeds the orbits of the particles 1 are followed. The occupation of the particles 1 are calculated at the grid points and we can obtain the occupation rate by calculating

$$\text{Occupation rate} = \frac{N_{i,j}^{(1)}}{N_{i,j}}, \tag{2.3}$$

where $N_{i,j}$ denotes number of the particle at the grid point (i,j), and $N_{i,j}^{(1)}$ denotes that of the particle 1. The mixing rate is obtained by transforming the occupation rate in accordance with

$$\text{Mixing rate} = -2.0\,|\text{Occupation rate} - 0.5| + 1.0 \tag{2.4}$$

Table 2.1: Plasma parameters used in the simulations in this chapter.

λ/r_{gi}	V_0/V_A	N	β_{ion}	$\beta_{electron}$	M/m	ω_{ge}/ω_{pe}	subsection
4.0	-1.0	32	0.15	0.15	16	0.35	2.3.5
4.0	-1.0	128	0.15	0.15	16	0.35	2.3.3, 2.3.5
4.0	-1.0	256	0.15	0.15	16	0.35	2.3.5
4.0	-1.0	512	0.15	0.15	16	0.35	2.3.5
2.0	-1.0	128	0.15	0.15	16	0.35	2.3.4
1.0	-1.0	128	0.15	0.15	16	0.35	2.3.4, 2.3.6
1.0	+1.0	128	0.15	0.15	16	0.35	2.3.6

The conversion of the occupation rate to the mixing rate is summarized in Fig. 2.5. The mixing rate is defined so that it takes the maximum value when the particle 1 occupies the grid point equally with the other particle.

2.3.3 Non-linear development of the K-H instability for $\lambda/\mathrm{r_{gi}} = 4.0$

Figure 2.6 shows the snapshots of the simulation result for $\lambda/\mathrm{r_{gi}} = 4.0$. The color intensity shows the occupation rate of the ion 1 and the contour lines show the electrostatic potential. Figure 2.7 shows the similar snapshots as shown in Figure 2.6 but for the electron. Both figures show the vortex motion of the K-H instability as expected from the MHD results. In the linearly growing stage the FGM develops with the growth rate as expected from the linear analysis. Figure 2.8 shows the time development of the FGM along with the result obtained in the linear analysis. The dashed line shows the result obtained in the linear analysis which justifies that the simulation result agrees well with the linear theory.

The mixing rate integrated in the simulation domain is examined to show how the mixing area is broaden in the simulation domain. Figure 2.9 shows the time profile of the integrated mixing rate normalized by the initial shear area $\mathrm{L_x}\lambda$. It is to be noted from Figure 2.9 that both the ion and the electron mixing area increase with time as the K-H instability develops. To elucidate how the electron mixing area as well as the ion's increases in spite of

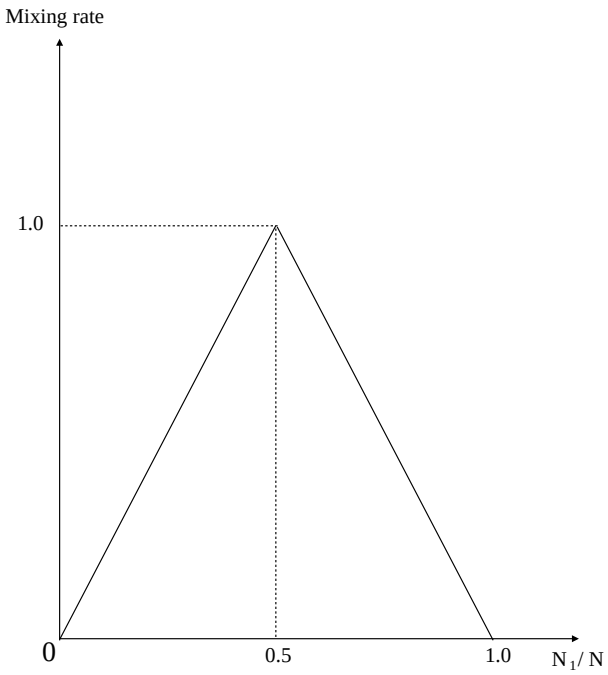

Figure 2.5: The relation between the occupation rate and the mixing rate.

the small gyro radius, the orbits of the ions and electrons are traced during the simulation run. Shown in Figure 2.10 and Figure 2.11 are the typical (A)orbit in the simulation domain, time development of (B)the y coordinate and (C)the x coordinate, and (D)the orbit in the phase space. As shown in Fig. 2.10(A) and 2.11(A) both the ion and electron shows the hydrodynamical orbits which are characterized by a $\mathbf{E} \times \mathbf{B}$ drift. Figure 2.12 and 2.13 show the snapshots of the mixing rate which correspond to the Figure 2.6 and 2.7. As time proceeds from the top left panel ($t = 62.16\lambda/V_0$) to the bottom right panel ($t = 207.19\lambda/V_0$) both figures indicate that the most mixed region appears along the boundary which is stretched, folded and deformed in the course of the non-linear development of the K-H instability.

Figure 2.14 shows the time profile of the average mixing rate for (A)the ion and (B)the electron as a function of the x coordinate. The average mixing rate is obtained by integrating it in the y direction normalized by the value integrated in the simulation domain at each time steps. Thus the average mixing rate as a function of the x coordinate indicates the contribution of the mixing rate in the x direction to the total value at each time steps. In the linearly growing stage from $t = 0$ to $t = 100\lambda/V_0$ most of the contribution of the

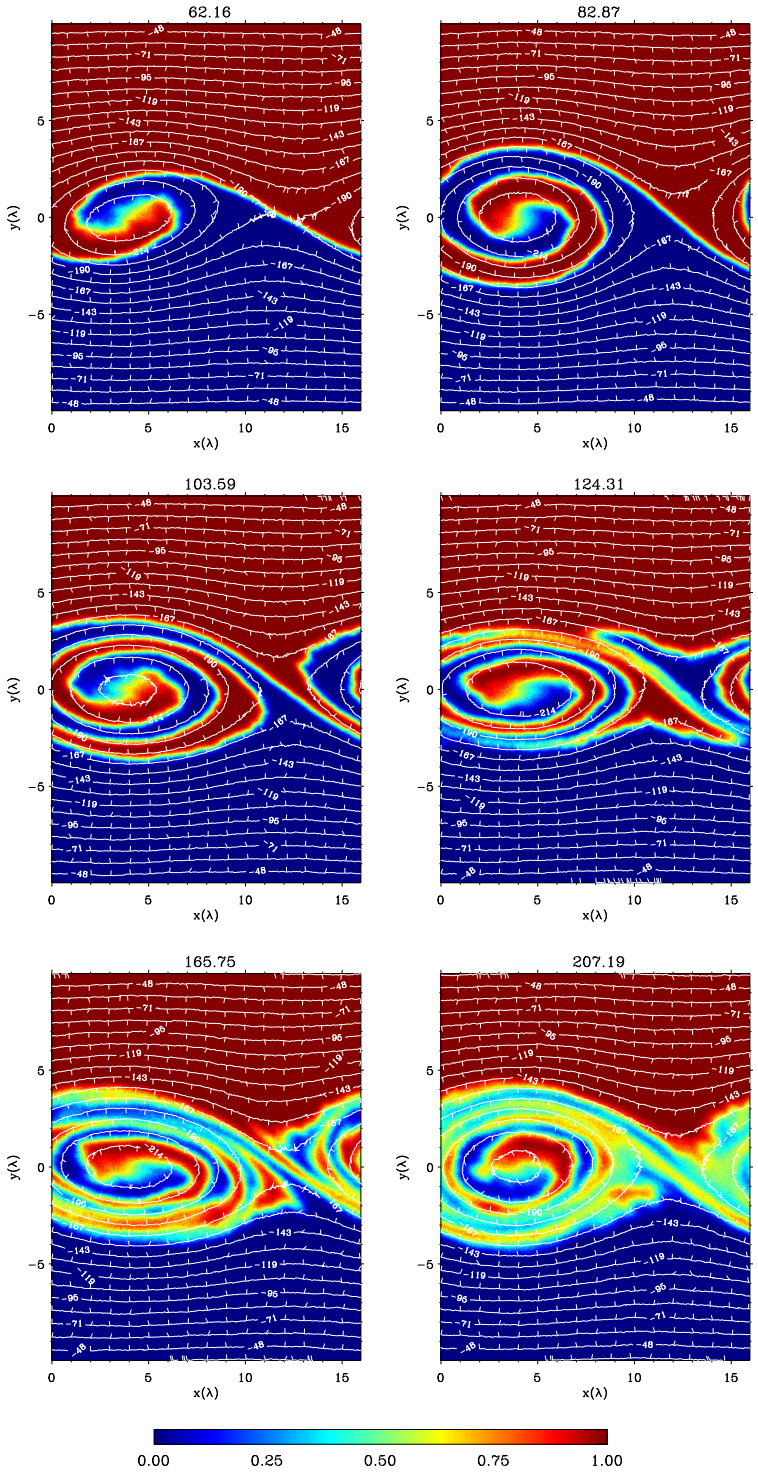

Figure 2.6: Snapshots of the simulation result for $\lambda/r_{gi} = 4.0$. The color intensity indicates the occupation rate calculated in accordance with eq.(2.3). The contour lines show the electrostatic potential whose equipotential lines approximately indicate the fluid stream lines.

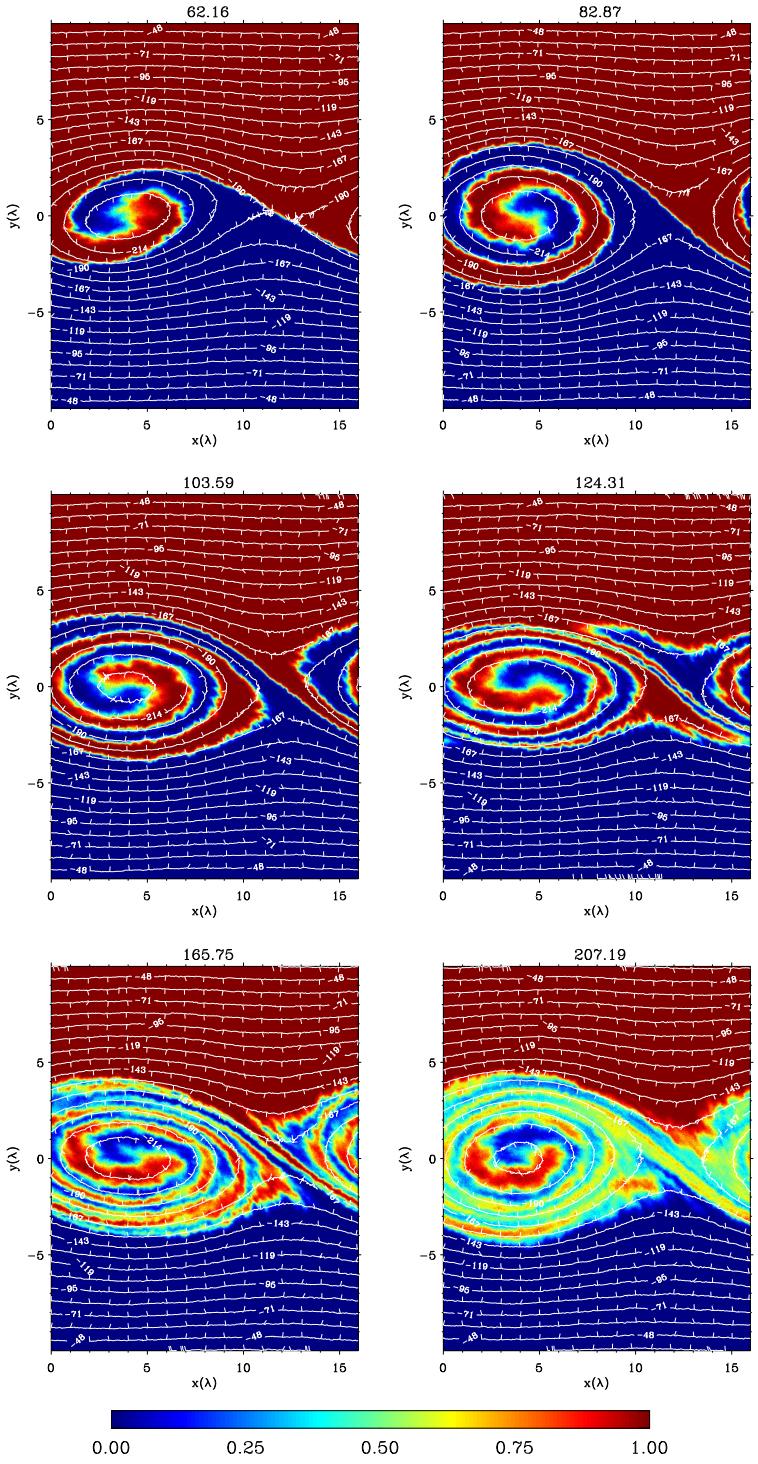

Figure 2.7: Snapshots of the electron occupation rate are shown in the same format of ion's in Fig. 2.6.

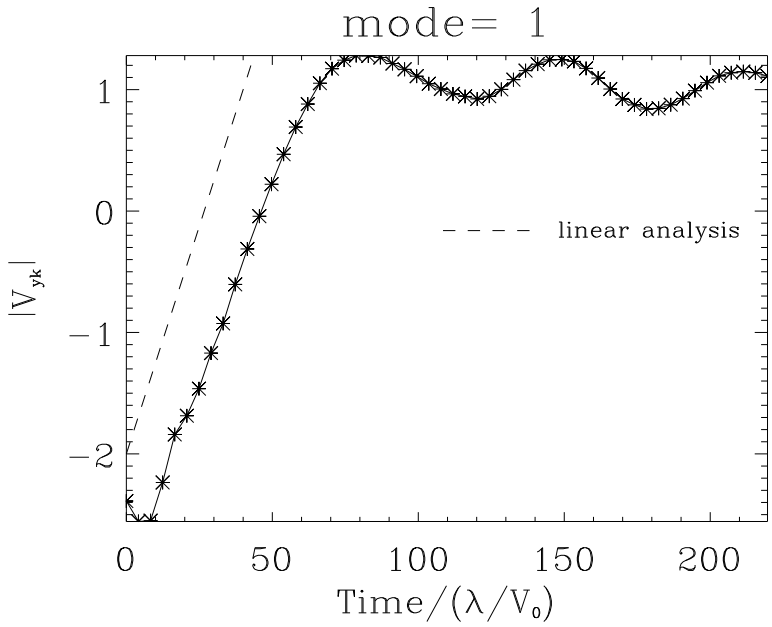

Figure 2.8: Time development of the FGM (solid line with asterisks) is shown in the same format of Figure 2.4. The dashed line shows the result obtained in the linear analysis.

mixing rate to the total value takes place within the region $x = 0 \sim 8\lambda$ in both the ion and the electron results, which means that it takes place within the K-H vortex. In the early non-linear stage from $t = 100$ to $t = 180$, although the most mixed region within the K-H vortex is not clear as can be seen in the linear stage, the contribution of the mixing rate within the vortex is a main part. In the late non-linear stage from $t = 180$ to the end of the simulation run the contribution of the mixing rate is uniformly distributed in the x direction. This phase corresponds to the diffusive phase as indicated by Fujimoto and Terasawa[1994]. Figs. 2.9-2.14 indicate that the increase in the mixing area shown in Figure 2.9 is a result of the stretched path length of the boundary layer in the course of the linear and non-linear development of the K-H instability.

From these results the increase in the mixing area can be modeled by the following mechanisms. Initially, the classical diffusion perpendicular to the demarcation line is dominant since there is no evident increase in the length of the demarcation line. The next stage

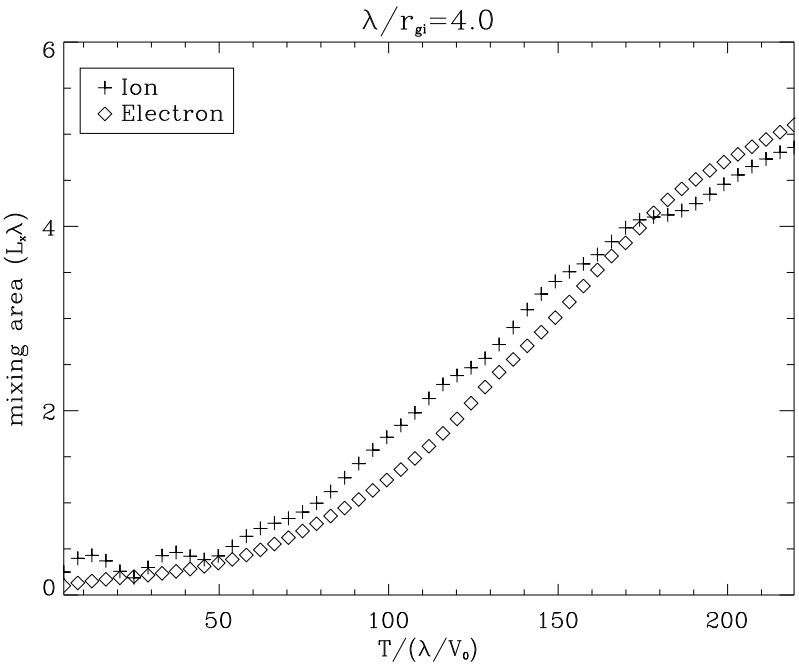

Figure 2.9: Time profile of the integrated mixing rate for the ion (cross) and the electron (open square). The abscissa shows the time normalized by the factor λ/V_0 and the ordinate shows the integrated mixing rate normalized by the initial shear area $L_x\lambda$.

is contributed mainly by the increase in the length of the demarcation line. The lateral diffusion is also operative in this stage in the old boundary as well as in the newly generated boundary. Incorporating these mechanisms the total mixing area at a time t can be expressed as follows.

$$S_{mix}(t) = L_x\sqrt{D_\perp t} + \int_0^t \sqrt{D_\perp(t-t')}\frac{dl(t')}{dt}dt' + \int_0^t r_g\frac{dl(t')}{dt}dt' + L_x r_g, \qquad (2.5)$$

where $D_\perp$ is the cross-field diffusion coefficient, L_x is the wave length of the FGM, $l(t)$ is the increment of the path length of the demarcation line which is a function of t, and r_g is the thermal gyro radius of the particle. The first term in the right-hand side of the equation represents the "old" boundary in which particles are diffused with time. These particles consist mainly inside the K-H vortex. The second term represents the generation of the new demarcation line along with the lateral diffusion. In the new boundary particles are also

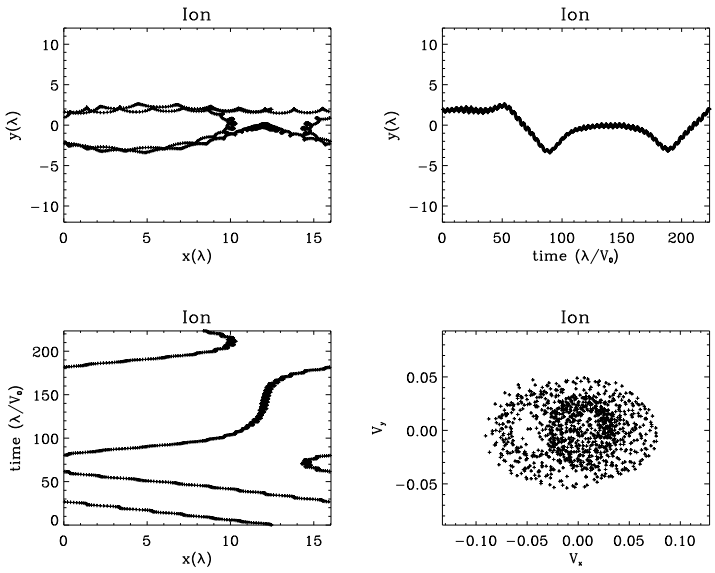

Figure 2.10: (A)The orbit in the simulation domain, (B)the time development of the y coordinate and (C)the x coordinate, and (D)the orbit in a phase space are shown. The coordinate x and y are normalized by the initial shear width λ, the time is normalized by the parameter λ/V_0, and the velocity is in the unit of the speed of light.

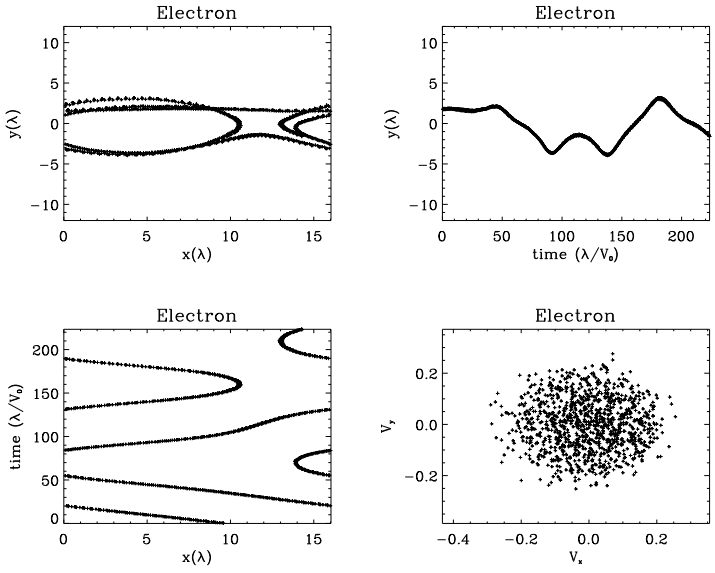

Figure 2.11: Same profiles as shown in Fig. 2.10 but for the electron.

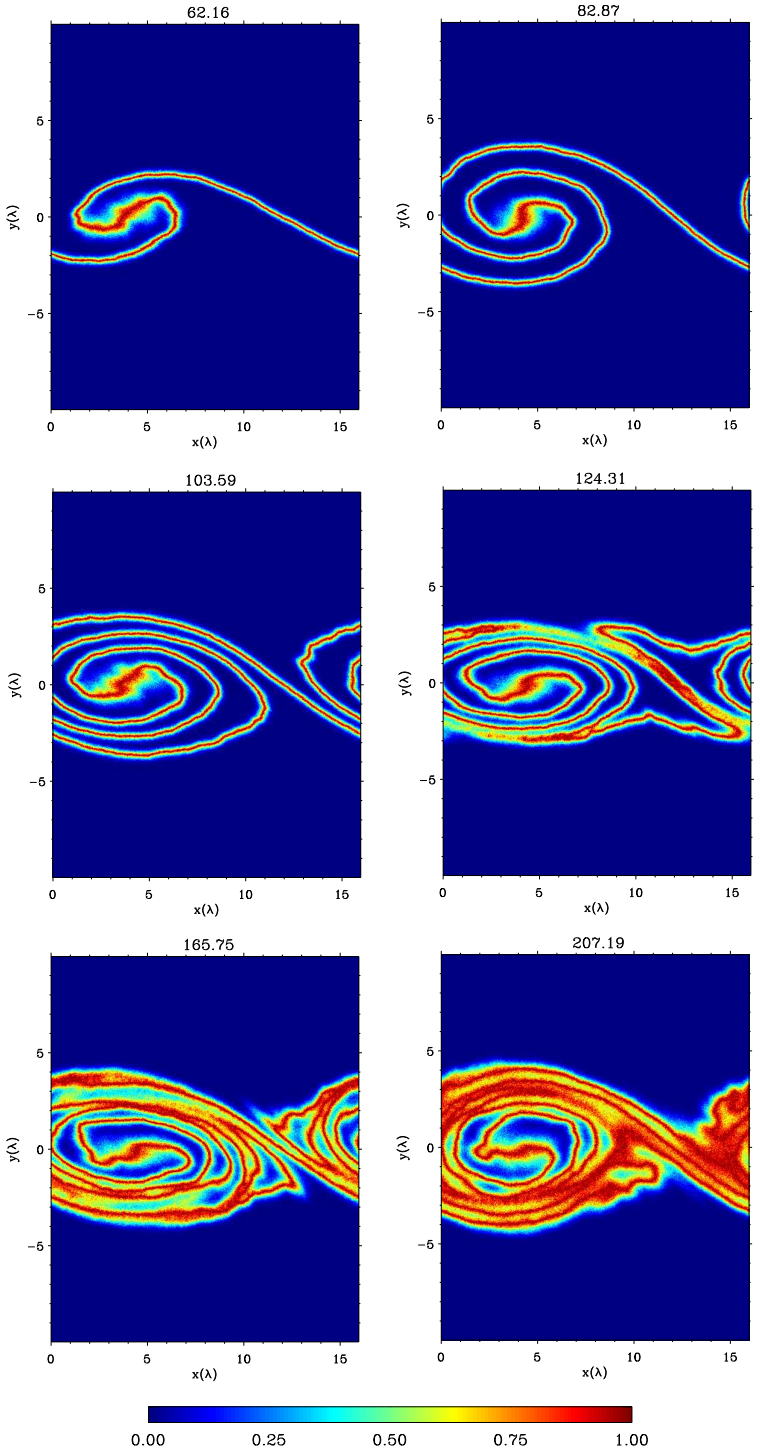

Figure 2.12: Snapshots of the ion mixing rate are shown in the same format of Fig. 2.6.

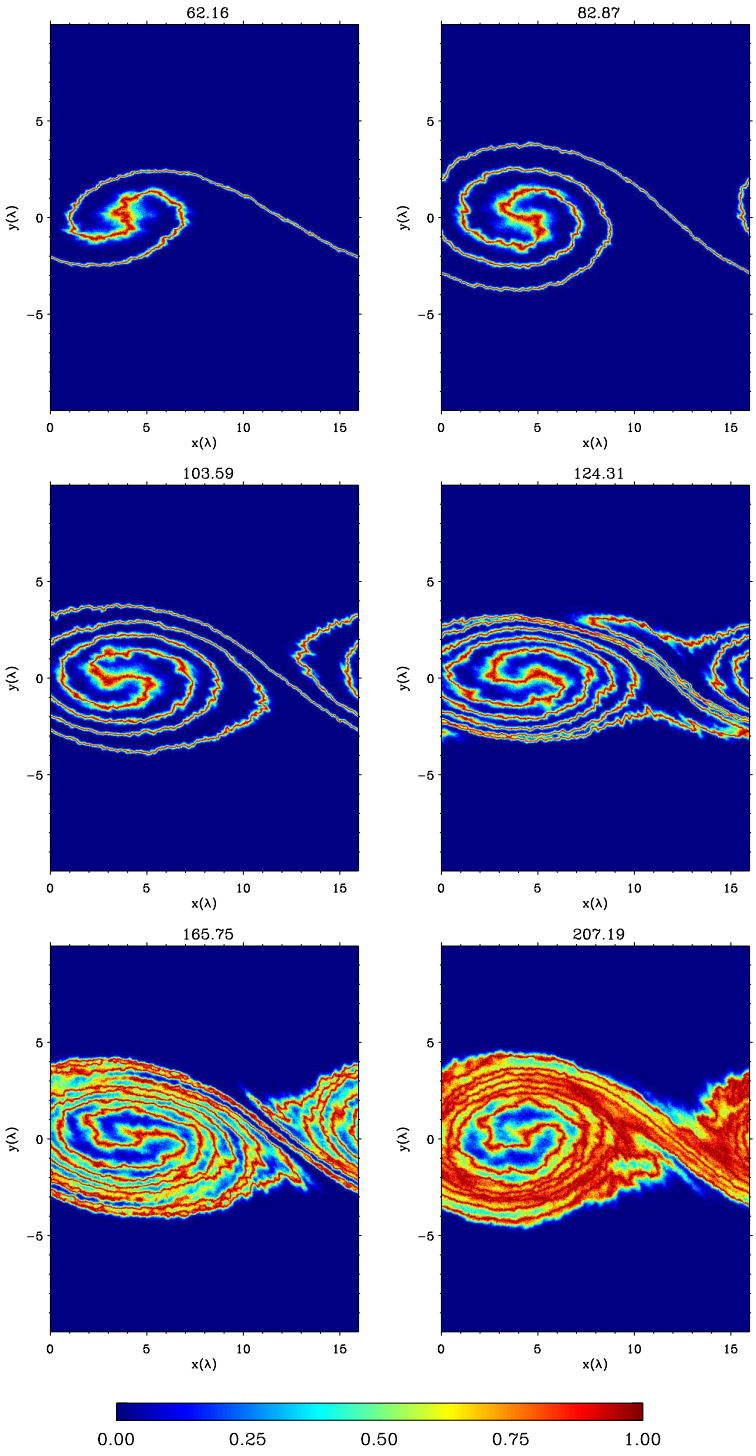

Figure 2.13: Snapshots of the electron mixing rate are shown in the same format of ion's in Fig. 2.6.

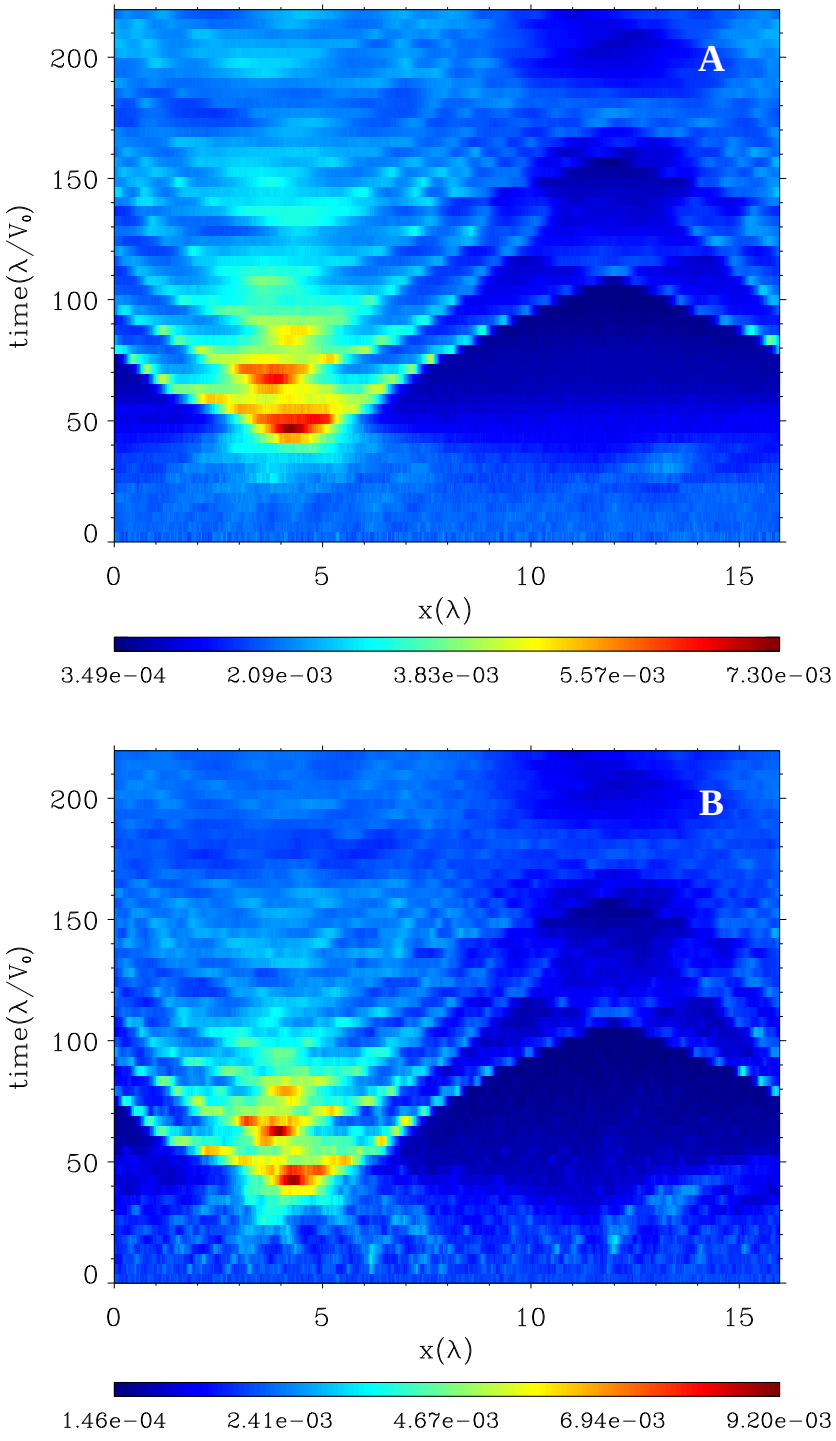

Figure 2.14: The time profile of the average mixing rate for (A)the ion and (B)the electron as a function of the x direction is shown by the color intensity. The average mixing rate is obtained by integrating the mixing rate in the y direction normalized by the value integrated in the simulation domain at each time. The abscissa shows the normalized x coordinate and the ordinate shows the normalized time.

diffused in the perpendicular direction and contribute to the increase in the mixing area. The last two terms represents the offset of mixing area with the scale of gyro radius. From eq.(2.5) the normalized mixing area is obtained as

$$S'_{mix}(T) = \frac{S_{mix}}{L_x \lambda} = \sqrt{\frac{D_\perp}{\lambda V_0}} \left(\sqrt{T} + \int_0^T \sqrt{T - T'} \frac{dL(T')}{dT} dT' \right) + \frac{r_g}{\lambda} \left(\int_0^T \frac{dL(T')}{dT} dT' + 1 \right) \quad (2.6)$$

where T represents time normalized by the factor λ/V_0 and $L(T)$ is the length of the newly generated demarcation line normalized by the wave length of the FGM $L_x \approx 16\lambda$. The second term on the right-hand side of the equation has the highest order of T and thus the normalized mixing area is weakly dependent on the dimensionless parameter $D_\perp/(\lambda V_0)$. The increase in the mixing area is mainly contributed from the generation of the new boundary. This is expressed by the term dL/dT whose exact functional form is not obtained. In the early stage ($T = 0 \sim 75$), dL/dT can be related to the linear growth of the K-H instability and be expressed in the functional form of $dL/dT \approx \exp(\gamma_{mix(1)} T) - 1$. In this approximation, inserting it to eq.(2.6), one finds

$$\begin{aligned} S'_{mix}(T) &= \sqrt{\frac{D_\perp}{\lambda V_0}} \left[(1 - \frac{1}{\gamma_{mix(1)}}) \sqrt{T} - \frac{2}{3} T^{3/2} + \frac{\sqrt{\pi}}{2\gamma_{mix(1)}^{3/2}} \exp(\gamma_{mix(1)} T) Erf\left(\sqrt{\gamma_{mix(1)} T} \right) \right] \\ &+ \frac{r_{gi}}{\lambda} \left(\frac{1}{\gamma_{mix(1)}} \exp(\gamma_{mix(1)} T) - \frac{1}{\gamma_{mix(1)}} - T + 1 \right), \end{aligned} \quad (2.7)$$

where $Erf(t)$ is the error function and is defined as

$$Erf(t) = \frac{2}{\sqrt{\pi}} \int_0^t \exp(-x^2) dx. \quad (2.8)$$

Then mixing rate is fitted by using eq.(2.7) with two free parameters, $D_\perp$ and $\gamma_{mix(1)}$. Figure 2.15 shows the result of fitted curve line (solid green) and the simulation data for the (A)ion and (B)electron. The two free parameters are determined by using the simulation data from $T = 0 \sim 75$ and the curve is extended to $T = 160$. As results the function of eq.(2.7) well fits with the data and the free parameters are obtained for the ion, $D_\perp/\lambda V_0 = 2.3 \times 10^{-5}$, $\gamma_{mix(1)} = 7.3 \times 10^{-4}$ and for the electron, $D_\perp/\lambda V_0 = 3.1 \times 10^{-4}$, $\gamma_{mix(1)} = 1.1 \times 10^{-3}$. While the $\gamma_{mix(1)}$ does not change in order in magnitude between the ion and the electron profiles, the electron diffusion coefficient $D_\perp$ is about ten times larger than that of the ion, indicating that the electron effectively gains the mixing area. To compare with the results obtained

above, here we introduce the diffusion coefficient of the lower-hybrid mode as (Treumann et al., 1991)

$$D_{LH} = \left(\frac{\pi}{8}\right)^{\frac{1}{2}} \frac{m_i}{m_e} \left(1 + \frac{w_{pe}^2}{\Omega_{ge}^2}\right) \frac{\int W_k dk}{n k_B T_i} \omega_{LH} r_{ge}^2, \tag{2.9}$$

where Ω_{LH} is lower hybrid frequency, r_{ge} is the electron gyro radius, nk_BT_i is the ion thermal energy density, and W_k is the field energy of perturbed electric field of the k-th mode and defined as

$$W_k = \left(1 + \frac{\omega_{pe}^2}{\Omega_{ge}^2}\right) \left(1 + \frac{k^2 v_{thi}^2}{\omega_{LH}^2}\right) \frac{\delta E_k^2}{8\pi}, \tag{2.10}$$

where v_{thi} is the ion thermal speed. Using the simulation parameters and data, we obtain

$$D_{LH}/\lambda V_0 \sim 10^{-3} \tag{2.11}$$

which is about 10 times larger than the electron diffusion coefficient obtained from the above fitting result.

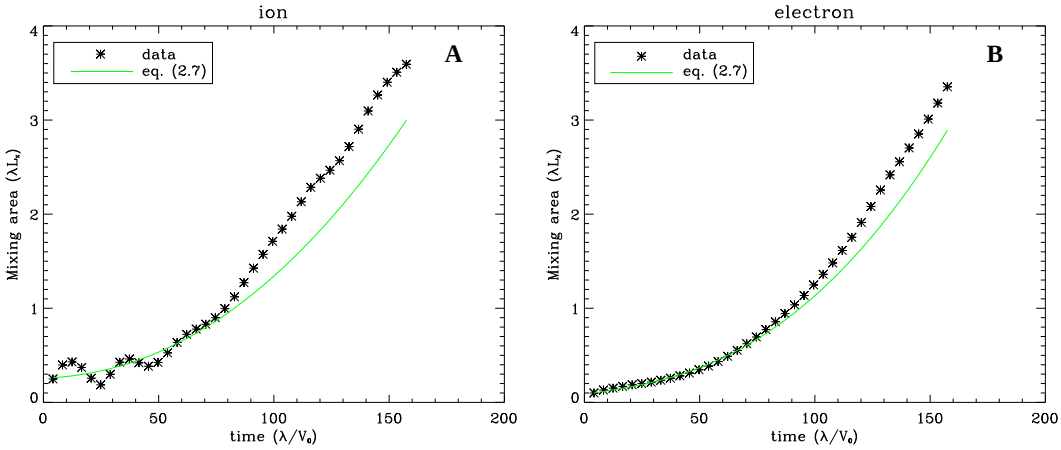

Figure 2.15: Time profile of (A)ion and (B)electron mixing rate with fitted curve lines (solid green) are shown in the same format of Fig.2.9.

In the late stage ($T = 75 \sim$) the mode amplitude is saturated as was seen in Figure 2.8, and dL/dT can be expressed as a constant. In this approximation one finds the time profile of the mixing area as

$$S'_{mix}(T) = \sqrt{\frac{D_\perp}{\lambda V_0}} \sqrt{T} \left(1 + \frac{2}{3}\gamma_{mix(2)} T\right) + \frac{r_{gi}}{\lambda} \left(\gamma_{mix(2)} T + 1\right), \tag{2.12}$$

where $\gamma_{mix(2)}$ represents the stretching speed of the demarcation line and here we assumed $dL/dT = \gamma_{mix(2)}$. In this stage, the mixing area increases with time with a functional form of $\sim T^{3/2}$.

2.3.4 Simulation results for various $\lambda/\mathrm{r_{gi}}$

From eq.(2.6), the mixing area should be scaled to the parameter $\sqrt{D_\perp/\lambda V_0}$ if the demarcation line self-similarly develops, i.e., the path length of the demarcation line is the same if one sees in the normalized unit. Figure 2.16 shows the snapshots of the mixing rate of the ion in each simulation runs for λ/r_{gi} = (A) 1.0, (B) 2.0, and (C) 4.0 with a fixed V_0. As is evident from Figure 2.16, the structure of the K-H vortex is similar in each other if one sees them in the normalized unit of space λ and time λ/V_0. Figure 2.17 shows the

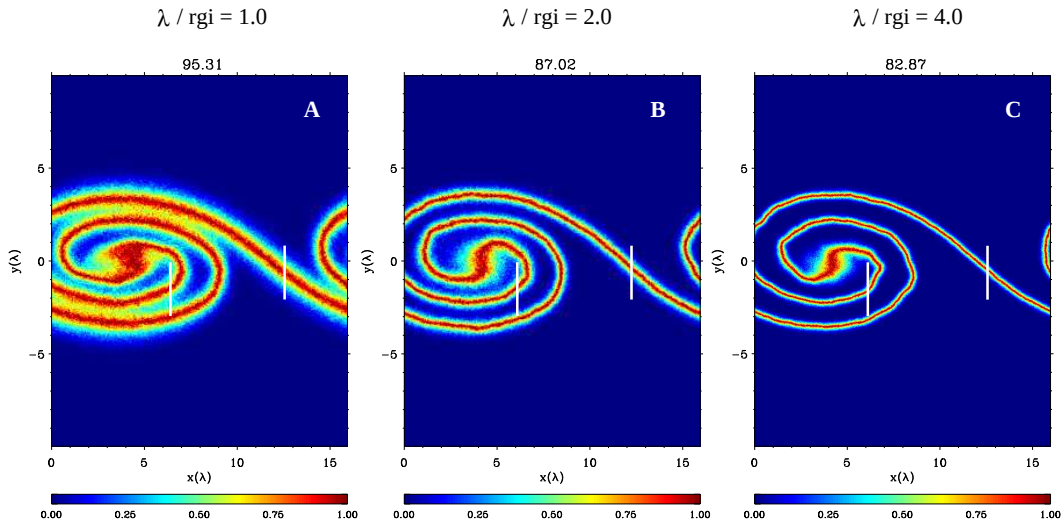

Figure 2.16: The snapshots of the mixing rate of the ion in the simulation runs of λ/r_{gi} = (A)1.0, (B)2.0 and (C)4.0 are shown. Figures show the same stages of the K-H instability, each of which are taken at $t = 95.31, 87.02, 82.87(\lambda/V_0)$, respectively.

integrated mixing rate for the various initial shear width for (A)the ion and (B)the electron. The mixing area saturates earlier in the thinner initial shear width case but the mixing area is weakly dependent on the initial shear width λ as was indicated by eq.(2.6). This can be explained alternatively by the following idea. In the normalized unit of time, the K-H

instability develops similarly and the same snapshots of the vortex evolution are obtained in a hydrodynamical regime. If one incorporates the diffusion across the magnetic field at the same time, the resultant picture is not obtained similarly. Here, we compare the case with the initial shear width λ_1 and λ_2 with a fixed velocity jump V_0 assuming a constant diffusion coefficient $D_\perp$. For a normalized time T, the time in which particles experience the gyro motion in each cases are expressed as

$$t_1 = \frac{\lambda_1}{V_0} T \tag{2.13}$$

$$t_2 = \frac{\lambda_2}{V_0} T \tag{2.14}$$

Hence, the diffusion of the particle at the demarcation line at T is expressed as

$$< \triangle x_1^2 > \;=\; D_\perp t_1 = D_\perp \frac{\lambda_1}{V_0} T \tag{2.15}$$

$$< \triangle x_2^2 > \;=\; D_\perp t_2 = D_\perp \frac{\lambda_2}{V_0} T \tag{2.16}$$

From these equations, we have

$$\frac{\triangle x_2}{\triangle x_1} = \sqrt{\frac{< \triangle x_2^2 >}{< \triangle x_1^2 >}} = \sqrt{\frac{\lambda_2}{\lambda_1}}. \tag{2.17}$$

Thus, we cannot obtain the same picture of the K-H instability at a normalized time T if we incorporate the particle dynamics. Figure 2.18 shows the width of the ion mixing area at the demarcation line sliced vertically at (A)$x = 12.5\lambda$ and (B)$x = 6.25\lambda$ in each simulation runs as indicated by the white vertical lines in Figure 2.16. The y coordinate is instead normalized by ion thermal gyro radius. At $x = 12.5\lambda$ the mixing areas almost coincide with each other with a scale of ion thermal gyro radius. On the other hand, at $x = 6.25\lambda$ inside the vortex, they no longer coincide with each other and the width of the mixing area is wider in larger λ and the width is scaled to $\sqrt{\lambda}$ rather than λ. This difference comes from the "age" of the demarcation line. The mixing is just started at the hyperbolic point of the flow and the longer diffusion process is operative in the older demarcation line inside the vortex. Figure 2.19 again shows the time profile of integrated mixing rate of the case $\lambda/r_{gi} = 1.0, 2.0$ for (A)the ion and (B)the electron. Additionally, the red and green lines are shown. These two color lines show the result of the case $\lambda/r_{gi} = 4.0$ multiplied by a factor

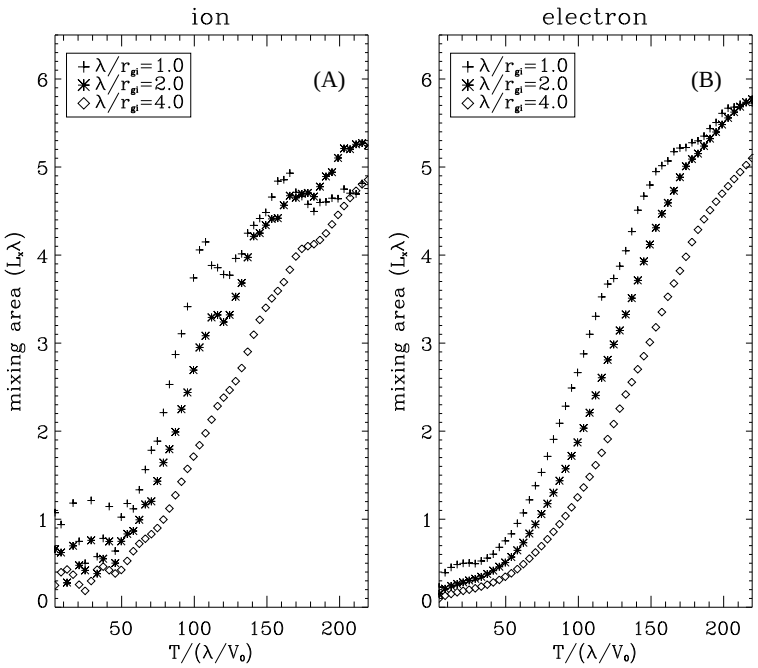

Figure 2.17: Mixing rate for the various initial shear width for (A)the ion and (B)the electron.

$\sqrt{\lambda_0/\lambda}$, where $\lambda_0 = 4r_{gi}$. It is clearly shown that the integrated mixing rate for both the ion and the electron is inversely scaled to square root of the initial shear width λ.

2.3.5 Electron mixing process

Returning to Figure 2.9, one can confirm that the electron mixing area effectively follows the ion's in spite of its small gyro radius. To explore how the electrons can effectively mix, the number of particles per cell is changed from N=32 to N=512 to reduce the electric field fluctuation by the statistical noise due to the finite particle number in calculating the electric current density as well as in the electric charge density. Figure 2.20 shows the snapshots of the electron mixing rate taken at $t = 82.37(\lambda/V_0)$ for each numbers of particles. The result for N=32 is somewhat too noisy and is not treated accurately enough as was revealed in Fig. 2.4. However, the result obtained in the simulation with more than N=128 show the similar profiles. As results, the time profile of the electron integrated mixing rate shows almost the same as shown in Figure 2.21. (The result for N=512 is not completed due to

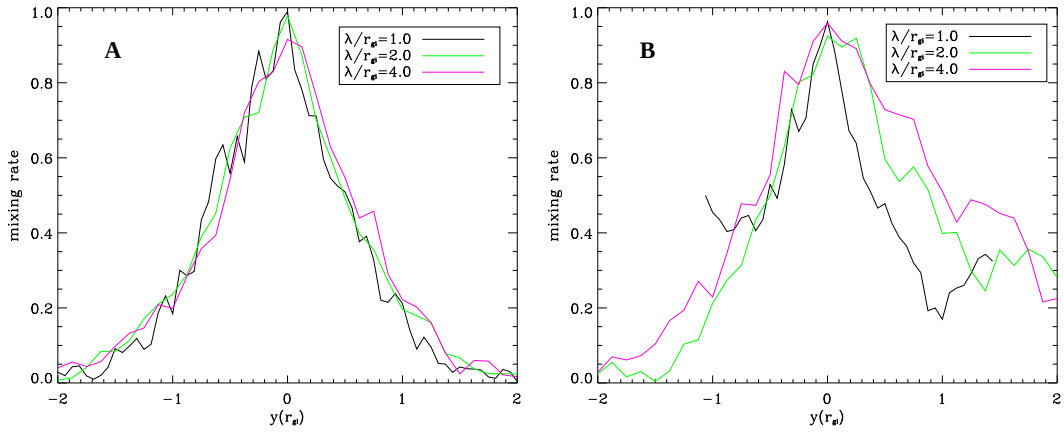

Figure 2.18: The sliced cuts of the mixing rate are shown for λ/r_{gi} =1.0(black), 2.0(green), 4.0(red) to compare the width of the ion mixing area. The cuts are taken at (A)$x = 12.5\lambda$ and (B)$x = 6.25\lambda$ as indicated by the white vertical lines in Fig.2.16.

its large computational resources and the limited CPU time.) It is notable that the diffusive mixing inside the vortex is enhanced in all simulation runs. To find out what causes the lateral diffusion inside the vortex, the energy spectra of the x component of the electric field are taken in the x direction and averaged in the y direction from $-3.32(\lambda)$ to $3.32(\lambda)$. Figure 2.22 shows the spectra taken at $t = 82.87(\lambda/V_0)$. Except the case of N=32, the simulations well express the scale $k_x\lambda = 0 \sim 5$, beyond which is affected by the particle number and fundamentally artificial. The modes within a scale $k_x\lambda = 1 \sim 5$ is, however, slightly enhanced in all simulation runs. Looking more carefully in Fig. 2.20 the deformation of the demarcation line itself is observed in all simulation runs as zoomed in the white frame. The characteristic scale of this structure is about one λ which can be related to the mode $k_x\lambda = 6.28$. The structure's scale is slightly smaller than the enhanced mode suggested in the energy spectrum. Since the reduced artificial noise does not strongly alters the electron mixing profile for the N=512 case, these modes may deform the structure of the demarcation line. The generation mechanisms of the structure, however, could not be identified in the present simulations.

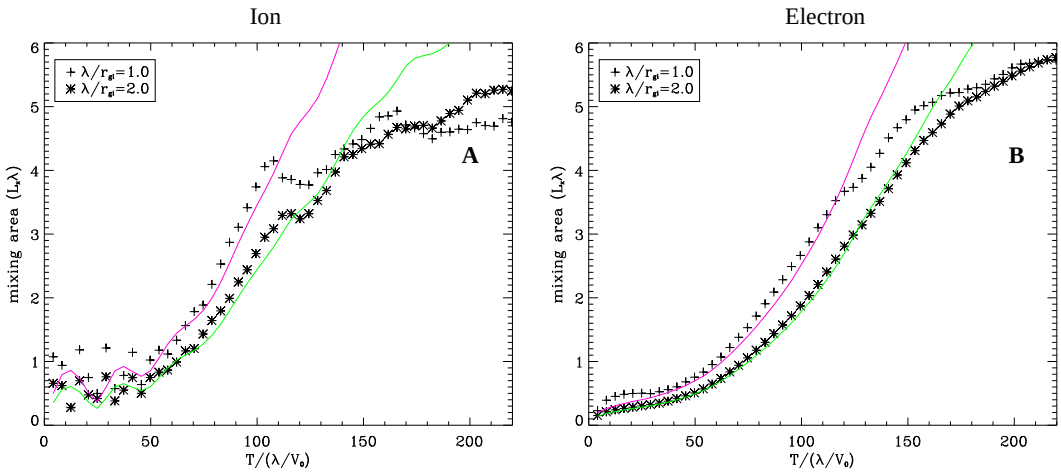

Figure 2.19: Time profile of the integrated mixing rate for the case $\lambda/r_{gi} = 1.0$ (cross), and $\lambda/r_{gi} = 2.0$ (asterisk) for (A)the ion and (B)the electron. Additionally, the red and green lines are shown. These two color lines show the result of the case $\lambda/r_{gi} = 4.0$ multiplied by a factor $\sqrt{\lambda_0/\lambda}$, where $\lambda_0 = 4r_{gi}$.

2.3.6 Thin shear cases ($\lambda/\mathrm{r_{gi}} = 1.0$)

In a thin boundary layer the difference in the motion between the ion and the electron cannot be negligible and their mixing area develop differently. In this regime, new parameters become important and are introduced for the initial setting along with the hydrodynamical parameters. The one defines the shear direction and is expressed as

$$\mathbf{B} \cdot (\nabla \times \mathbf{V}) \tag{2.18}$$

and the other parameter defines the shear strength

$$|\frac{1}{\Omega_{gi}} \frac{\partial V_x}{\partial y}|. \tag{2.19}$$

The simulation results shown previously have the parameter range

$$\mathbf{B} \cdot (\nabla \times \mathbf{V}) > 0 \tag{2.20}$$

and therefore generally one calls this case "positive shear". The "negative shear" is the case in the range

$$\mathbf{B} \cdot (\nabla \times \mathbf{V}) < 0. \tag{2.21}$$

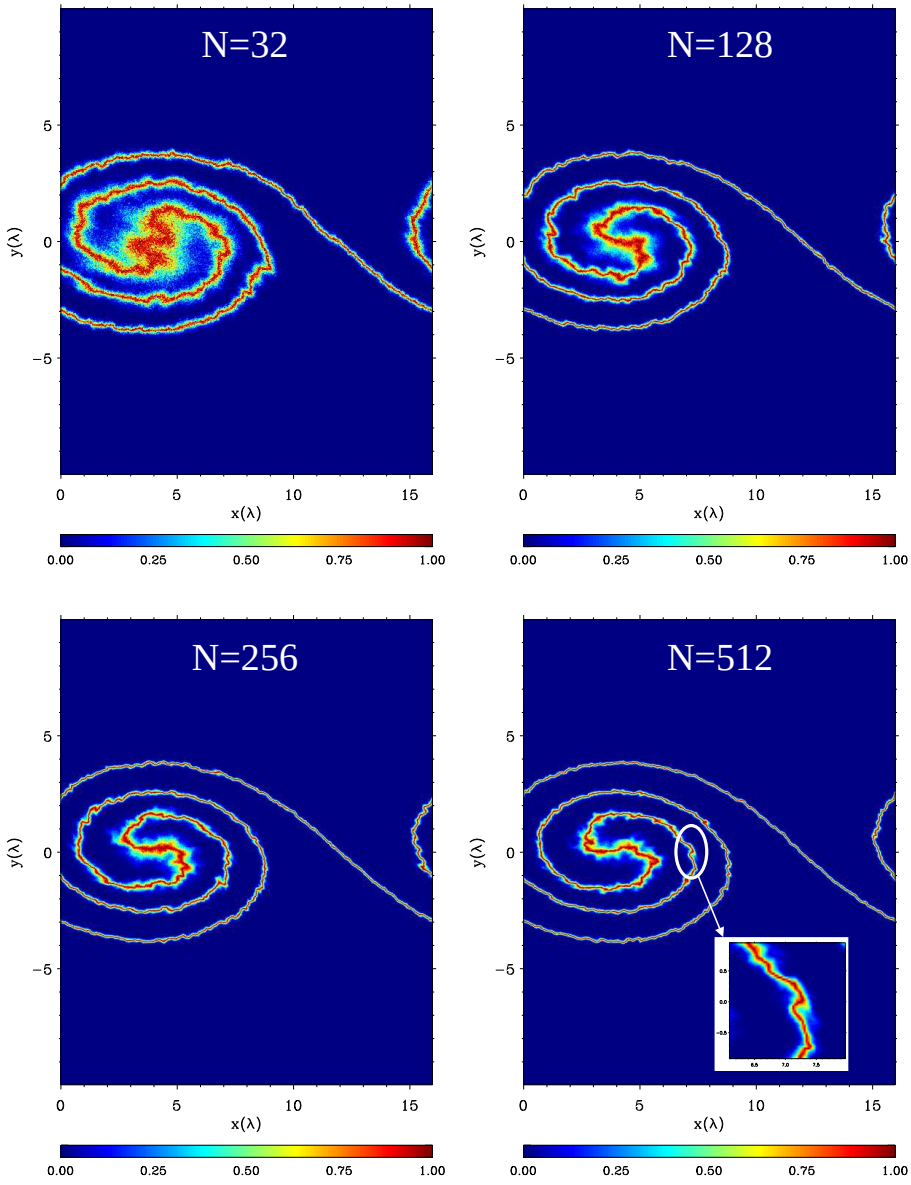

Figure 2.20: Snapshots of the electron mixing rate taken at $t = 82.37(\lambda/V_0)$ for each numbers of particles are shown. Meandering structure of the electron demarcation line is zoomed in the result with N=512.

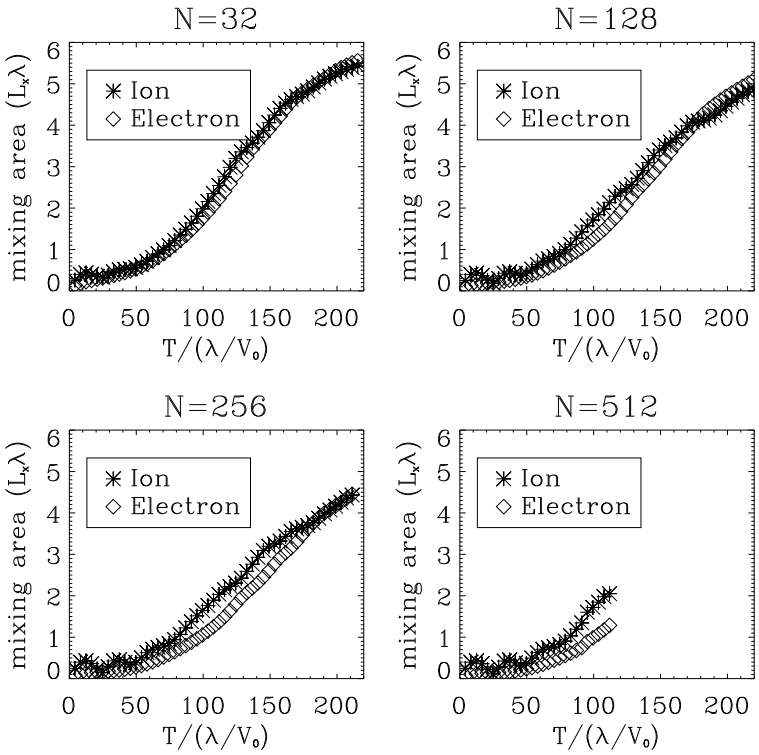

Figure 2.21: Time profile of the electron integrated mixing rate for various particle numbers. The result for N=512 is not completed due to its large computational resources and the limited CPU time.

In a MHD regime "positive" or "negative" does not have any significance and the results are mirrored images. However, in a strong shear regime, $|\frac{1}{\Omega_{gi}}\frac{\partial V_x}{\partial y}| > 1$, "positive" or "negative" is an important factor which will be verified in the following simulations. The results will be shown and discussed firstly for the positive shear case and after that the negative shear case will be presented. In both simulations we adopted

$$|\frac{1}{\Omega_{gi}}\frac{\partial V_x}{\partial y}| = 1.29. \tag{2.22}$$

(In chapter 4 the difference in the non-linear development of the K-H instability between in the positive and the negative shears is discussed and it is shown that the shear direction is important even in the MHD regime in a stratified shear layer.)

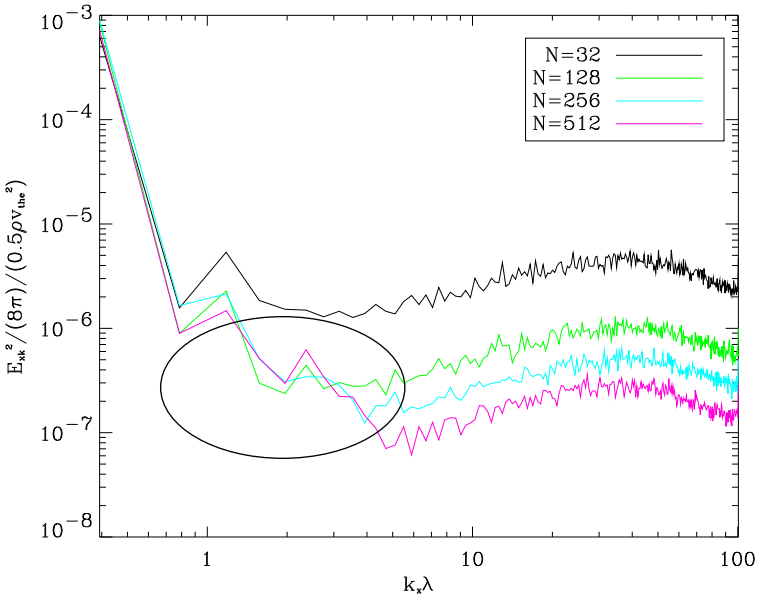

Figure 2.22: The energy spectra of the x component of the electric field normalized by the plasma energy density are shown for each particle numbers. The abscissa shows the wave number in the x direction normalized by the initial shear width λ.

2.3.6.1 positive shear

Figure 2.23 shows the snapshots of the occupation rate of the ion 1 (left column) and the electron 1 (center column) with the z component of the magnetic field (right column). The vector plots of the black arrows in the B_z profiles show the electric current density. As can be seen in the figure, the electron vortex rotates faster than that of the ion and accordingly, the electric current density flows inside the hole of the magnetic field. This difference can be confirmed in the linear stage since the perturbed magnetic field separates the motion between the ion and the electron. Figure 2.24 shows the eigen mode structure of the perturbed ion thermal pressure with the vector plot of the perturbed electric current density. Since the temperature ratio of the ion to the electron is one in the present linear analysis and in the simulation, particles drift with the equal speed so that the resultant current density satisfies the relation $\nabla \times \mathbf{B} = 4\pi/\mathrm{c}\,\mathbf{j}$, which can be confirmed in the Figure 2.24. In this situation the ion drifts clockwise and the electron drifts counterclockwise. Hence, the electron flows faster than the ion. Figure 2.25 shows the y component of the perturbed ion (asterisk)

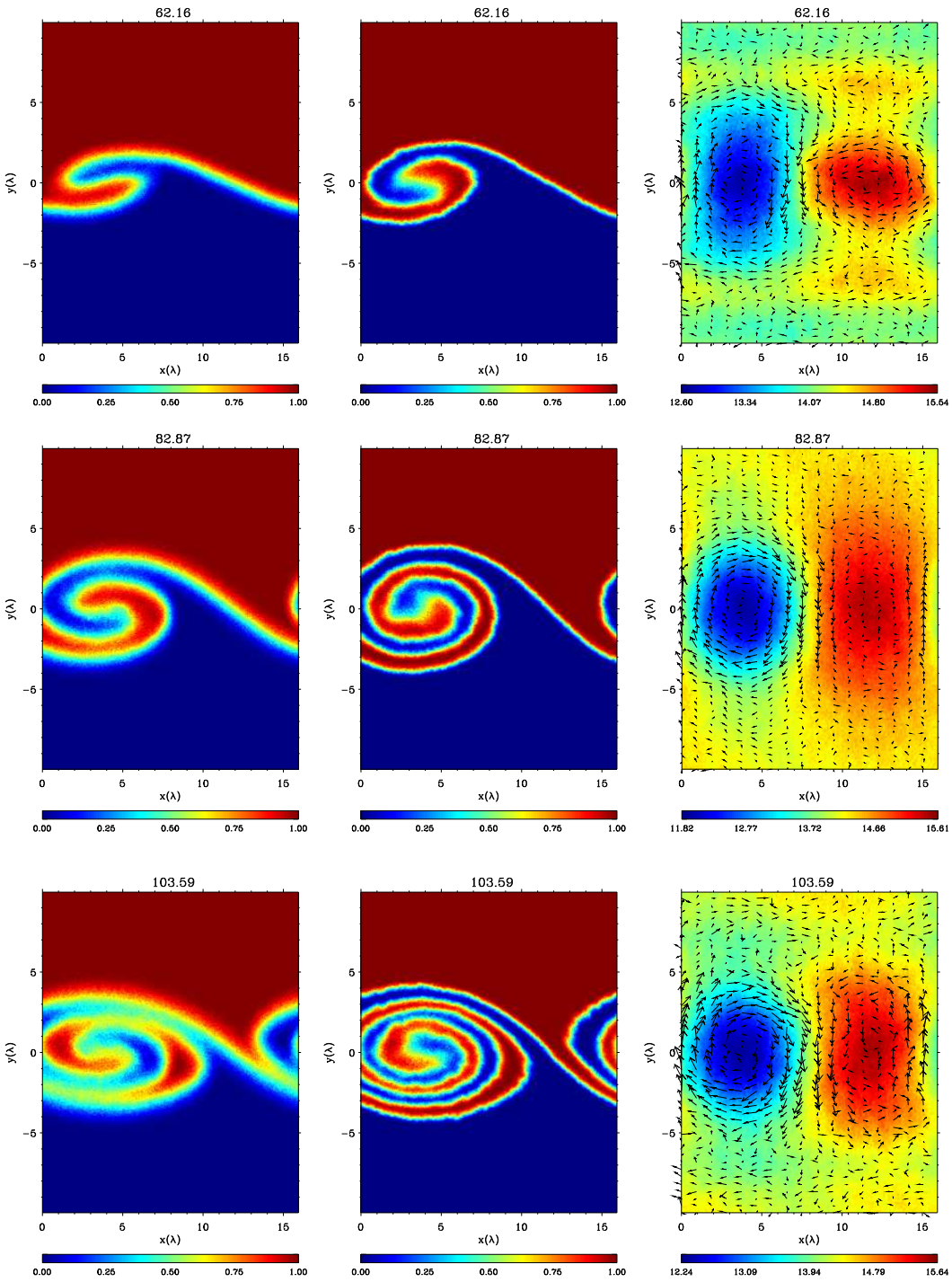

Figure 2.23: The snapshots of the occupation rate of the ion 1 (left column) and the electron 1 (center column) with the z component of the magnetic field (right column). The vector plots of the black arrows in the B_z profiles show the electron velocity difference from the ion's $(\mathbf{V}_i - \mathbf{V}_e)$. From the top to the bottom panel snapshots are taken at $t = 62.16\lambda/V_0$, $t = 82.87\lambda/V_0$, $t = 103.59\lambda/V_0$.

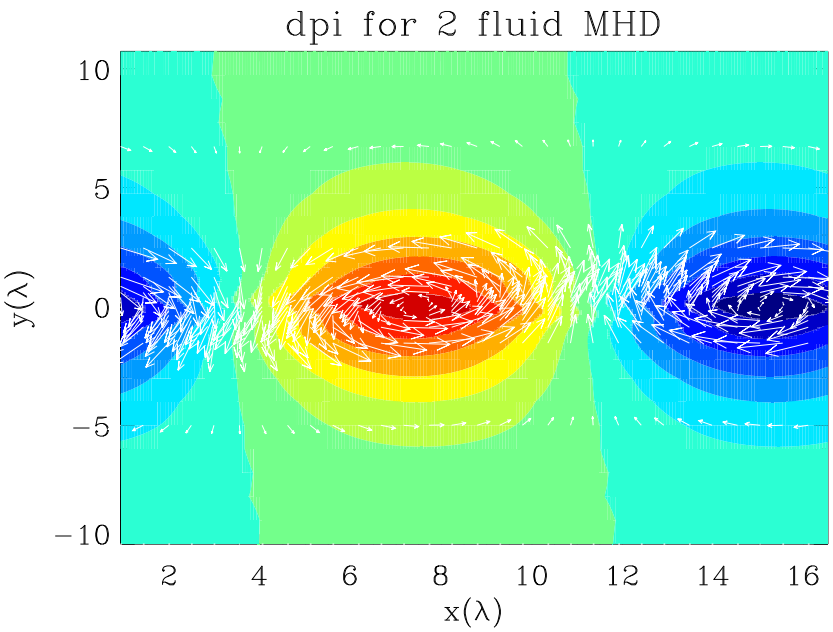

Figure 2.24: The K-H eigen mode structure of the perturbed ion thermal pressure with the vector plot of the perturbed electric current density.

and electron (open square) velocity along with the linear analysis result (dashed line) for $\lambda/r_{gi} = 1.0$. While the eigen mode of both the ion and electron velocity grows with the same rate as expected from the linear analysis, the amplitude of the electron velocity is about 16% larger than that of the ion: the electron gets more speed by the perturbed magnetic field. The pattern of the magnetic field, which shows the hole structure inside the vortex and the built up region at the hyperbolic point, is formed as follows. At first the flow is accelerated by the perturbed pressure of the K-H mode in the y direction and the fluid element starts rotating. Thus the fluid element feels centrifugal force during the rotation which results the rarefaction and makes a hole of magnetic field and thermal pressure. The structure of the vortex is therefore maintained by the force balance between the rotational centrifugal force and the centripetal force of the sum of thermal and magnetic pressure. Built up region at the hyperbolic point is due to the encounter of the two incoming flows which results a compression of plasma. This compressibility in plasma and the development of the instability reproduces the in-homogeneity which separates the motion of the ion and the electron.

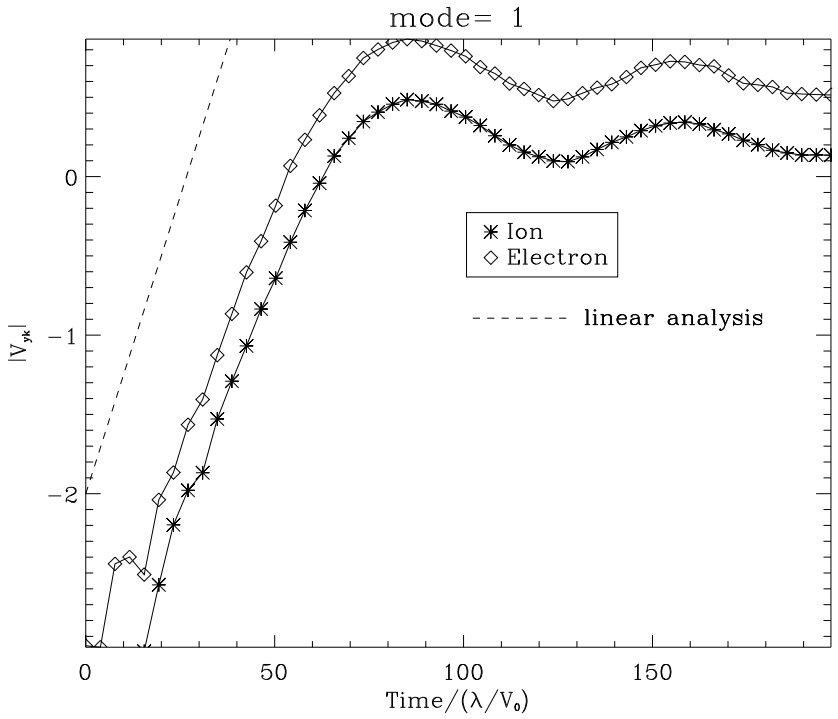

Figure 2.25: The y component of the perturbed ion (asterisk) and electron (open square) velocity along with the linear analysis result (dashed line) for $\lambda/r_{gi} = 1.0$.

2.3.6.2 negative shear

In a strong negative shear layer it has been reported that the K-H instability does not develop easily due to the technical difficulty in finding a exact initial condition for a particle simulation (Cai et al., 1990; Cai et al., 1993a; Pritchett, 1993). Cai et al.[1990] showed that the kinetic equilibrium is different in a positive and a negative shear layer if the velocity shear is strong enough ($\frac{1}{\Omega_{gi}}\frac{dV_x}{dy} >> 1$). They explained that this difference comes from the difference in the potential (non-uniform electric field) structure. Ions in the a positive shear around the origin are in stable equilibrium while ions in negative shear are in unstable equilibrium whose orbits diverge away from the shear layer. Due to its unstable orbit of the ion, the velocity shear is relaxed within a few gyro motions and as a result the K-H mode is stabilized. Pritchett [1993] carried out electrostatic particle simulations for a negative shear case. He used the initial particle loading method developed by Cai et al.[1990] and the modified temperature in the maxwell distribution function proposed by Ganguli et al. [1988]

and compared the linear growth of the K-H instability with the standard particle loading with the maxwell distribution. He found in a negative shear case no development of the K-H mode with the standard loading but found an improvement in the growth of the mode with using methods of Cai et al [1993] and Ganguli et al. [1988] although the resultant growth rate is reduced from that expected from the linear analysis. In the following simulation, Gaunguli's modified temperature is adopted for the initial loading of the ions.

Figure 2.26 shows the time development of the FGM along with the result of the positive shear case. The dashed line shows the linear growth obtained by the linear analysis. As reported by the past researches, the FGM weakly develops as compared to the result in the positive shear case. Figure 2.27 shows the snapshots of the occupation rate of the ion 1 and

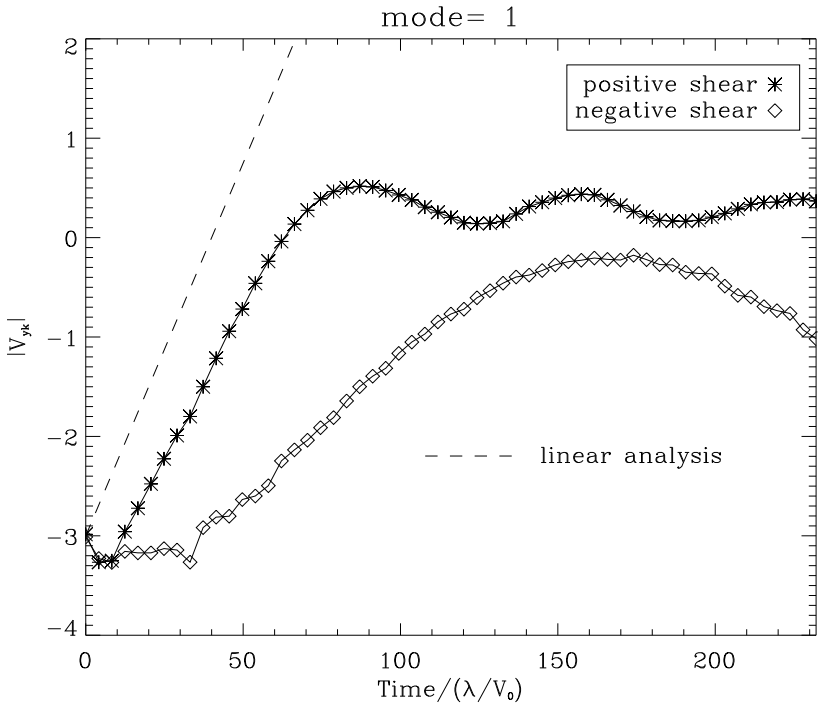

Figure 2.26: Time development of the FGM is shown for positive (asterisks) and negative shear (open diamond) case. The dashed line shows the result obtained in the linear analysis.

the electron 1. As shown in the figure, ions are quickly diffused over the scale of the velocity shear layer due to their unstable orbits. On the other hand electron does not suffer from the potential structure because of its small gyro radius. However, the diverged orbit of the ion

inhibit the development of the K-H instability and therefore electron mixing area does not strongly increase. This nature is clearly shown in Figure 2.28. Figure 2.28 shows shows the time profile of the integrated mixing rate for the (A) ion and (B) electron. The results show the cases for the positive shear (asterisks) and for the negative shear (open diamond). In the ion profile (A) of the negative shear case, ions are quickly diffused in the scale comparable to the K-H vortex size in the positive shear case. This is due to the diverged orbit of the ion. On the other hand, the electron mixing area of the negative shear case is inhibited due to the inhibited K-H vortex size. These results are consistent with the past researches that have indicated that the K-H mode does not strongly develop in the strong negative shear due to the ions' unstable orbits. Furthermore, the electron mixing area is strongly inhibited by the weak development of the K-H mode.

2.4 Summary and discussion

Full particle simulations of the Kelvin-Helmholtz instability in a uniform background field are conducted in this chapter. Although the finite Larmor radius effect of the ion is expected to enhance the mixing rate, the enhancement of the mixing rate in both the ion and the electron suggests that most of the well mixed region is dominated along the interface of the two plasmas which is stretched, folded, and as a result, deformed in the course of the development of the K-H instability.

The plasma mixing process proposed in this chapter consists of two mechanisms. The one is the generation of the new boundary by the development of the K-H instability. The total amount of the mixing area is mainly contributed from this process. At the same time, the cross-field diffusion perpendicular to the boundary is also operative. From the simple modeling of the mixing area, we found that it is scaled to $\sqrt{D_\perp/\lambda V_0}$ and the time dependence as $\sim T^{3/2}$ or higher.

The electron mixing is also investigated. As a result, the electron mixing area follows the ion's, which means that the electrons can mix more effectively. Examining in detail, the energy spectra of the electric field suggest that the modes $k_x\lambda \sim 5$ are slightly enhanced.

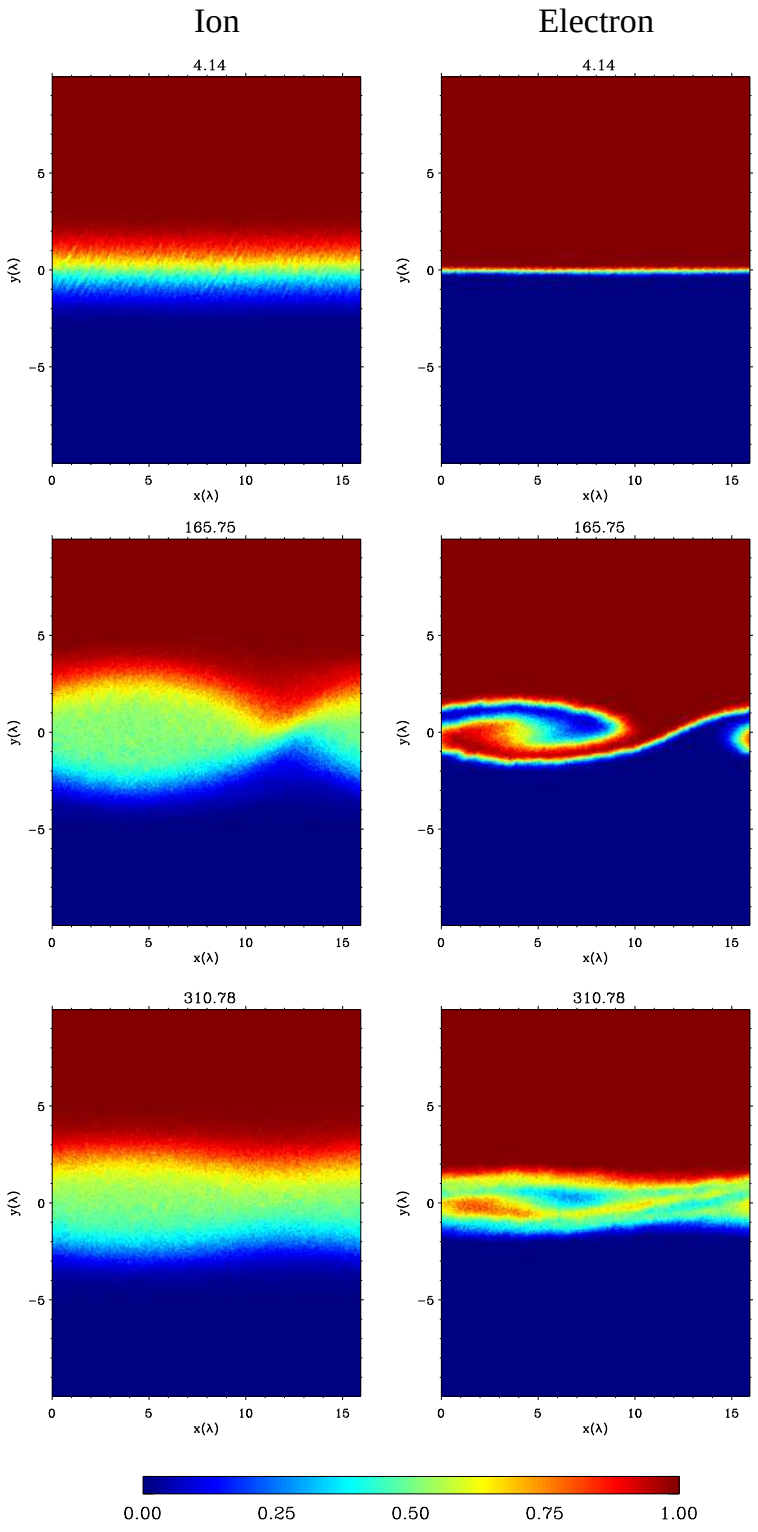

Figure 2.27: Snapshots of the occupation rate for the ion (left column) and electron (right column) for the strong negative shear layer.

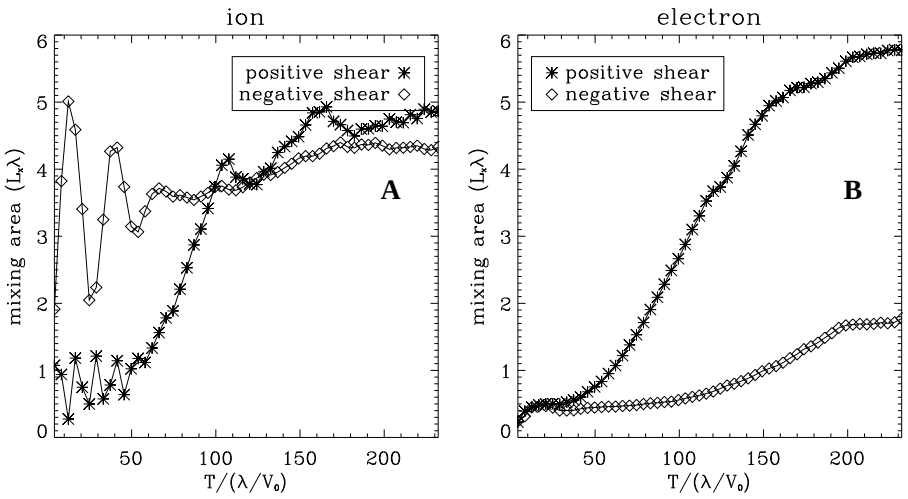

Figure 2.28: Time profile of the integrated mixing rate for (A) the ion and (B)the electron for the negative shear case (open diamond). For the comparison, the results obtained in the positive shear case are also shown in each panels (asterisks). The abscissa shows the time normalized by the factor λ/V_0 and the ordinate shows the integrated mixing rate normalized by the initial shear area $\mathrm{L_x}\lambda$.

The fine structures of the demarcation line appeared inside the vortex, whose characteristic scale likely corresponds to the modes observed in the energy spectra. This deformation of the demarcation line gains the new mixing area that may contribute to follow the ion mixing area. However, the generation mechanisms of the small scale structure which appears only in the electron mixing area could not clearly understood. For this explanation, the numerical heating due to the finite spacial grid size can be operative for the mixing (Birdsall and Langdon, 1991; Hockney, 1971). We estimated the heating time (at which the temperature becomes twice) for the case N=512 and obtained $T_{heat} \approx 3000\lambda/V_0$, which is much larger than the time scale of the present simulations ($T_{KH} \sim 200\lambda/V_0$). Hence the numerical heating is unlikely effective for the mixing process. Alternative explanation can be related to the fundamental cross-field diffusion process of plasmas. Okuda and Dawson [1973] studied the plasma cross-field diffusion for a wide range parameter of ω_{ge}/ω_{pe}, where ω_{pe} and ω_{ge} are the electron plasma and gyro frequency. In a weak magnetic regime, $(\omega_{\mathrm{ge}}/\omega_{\mathrm{pe}})^2 << 1$, which is the case of the present simulations, the diffusion coefficient obeys the classical

collisional theory. In this regime the most of the fluctuated field energy is in the upper- and lower-hybrid waves and in Bernstein waves. Furthermore, they also reported the anomalous electron transport. This process is lead by the convective mode which was derived by the two fluid equations in a thermal equilibrium. The convective motion enhances the electron diffusion whose diffusion coefficient is similar to that obtained in the Bohm diffusion. The identification of this anomalous electron diffusion as a generation mechanism which enhances the electron mixing area, however, was not successful in the present study and the further understanding of this kind of problem will be explored continuously as a future exercises.

CHAPTER 3

Turbulent mixing and transport across a stratified velocity shear layer

3.1 Introduction

Where there is a velocity shear, there is usually a density interface. A representative example, on which the present dissertation is focusing, is the interaction between the shocked solar wind plasma and the tenuous magnetospheric plasma at the Earth. The earth's magnetosphere shields the shocked solar wind plasma which is separated across the boundary, "magnetopause". In-situ observations, however, have revealed that the plasma which fills the plasma sheet is originated mainly from the solar wind (Fig. 1.5) even though the frozen-in condition seems to be valid around the earth. Hence, the route to the magnetosphere has been a major issue in the magnetospheric physics. To explain the magnetospheric interaction with the shocked solar wind, two models have been proposed. One is the "open magnetosphere model" by Dungey [1961], which incorporates the reconnection of the earth's dipole magnetic field lines with the interplanetary magnetic field (IMF) lines (Fig. 1.6, left panel). The other model is the "closed magnetosphere model" by Axford and Hines [1961], which suggested that a viscous interaction along the flanks of the magnetosphere can permit the solar wind momentum to diffuse onto closed magnetospheric field lines and the resultant tail ward flows is closed by the returning earthward flow in the center of the tail(Fig. 1.6). In-situ observations have showed the evidences of the reconnecting field lines (e.g., Phan et al., 2000) and the resultant convecting plasma flows inside the magnetosphere(e.g., Nishida et al., 1996). Nowadays the former has been widely accepted as a standard model in the case of southward IMF while the situation is less clear when the IMF is northward.

Several authors (Fairfield et al., 1996; Baumjohann et al. ,1989; Lennartsson, 1992) have noted that the aspects of the plasma sheet are controlled by the geomagnetic activity, which likely corresponds to the orientation of the IMF. Particularly, the plasma sheet often reveals it's feature which cannot be explained by the Dungey's model in the case of northward IMF (Terasawa et al., 1997, Borovsky et al., 1998, Wing and Newell, 2002; Nishino et al., 2002). Terasawa et al. [1997] studied statistically on the properties of the plasma sheet during the periods when the northward IMF dominates. They reported two important results; (1) the plasma sheet becomes significantly cold and dense, whose aspects resemble the solar wind plasmas (Fig. 3.1). (2) the plasma is colder and denser near the dawn and dusk flanks of the plasma sheet rather than in the central region. Their result (1) suggests that the

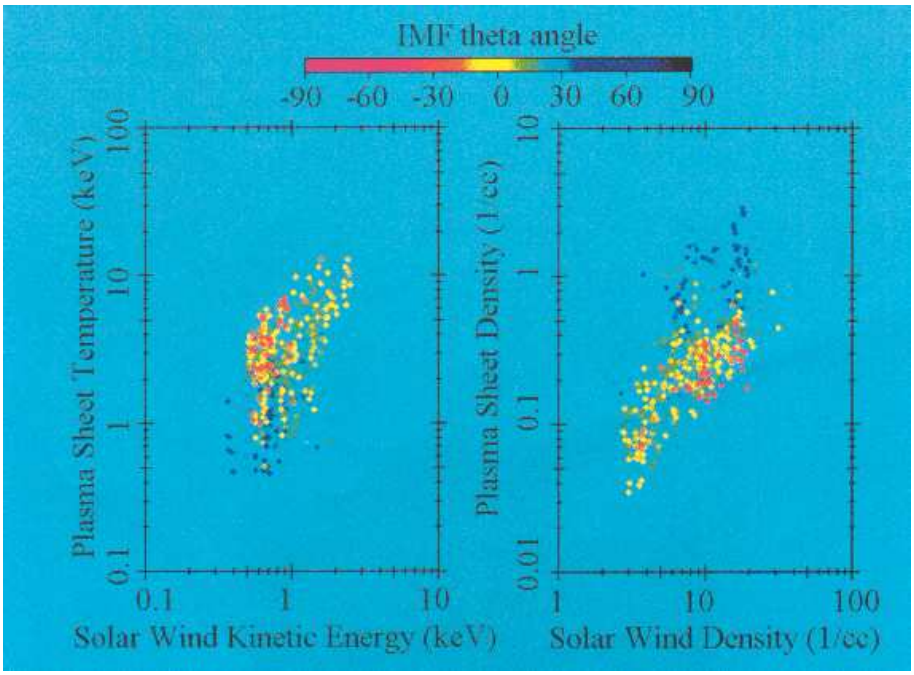

Figure 3.1: IMF dependence of plasma sheet temperature (left) and density (right) as a function of the solar wind kinetic energy is shown. Adopted from Terasawa et al. [1997].

solar wind plasma is transported without heating by the reconnection as Dungey's model proposed, and the result (2) suggests that the solar wind plasma can directly penetrate into the magnetosphere through the flank region of the tail. The idea of the tail flank region as a primary transport region has been proposed by several authors (Eastman et al.,

1985; Lennartsson, 1992; Fujimoto et al., 1998). Fujimoto et al. [1998] reported the in-situ observation of the low-latitude boundary layer (LLBL) in the near-earth tail flanks, where two populations of high and low energy ions are observed simultaneously (Fig. 3.2). The simultaneous observation of high and low energy plasmas indicates the mixture of the plasmas originated from the magnetosphere and the solar wind and the effective transportation across the low-latitude flank magnetopause.

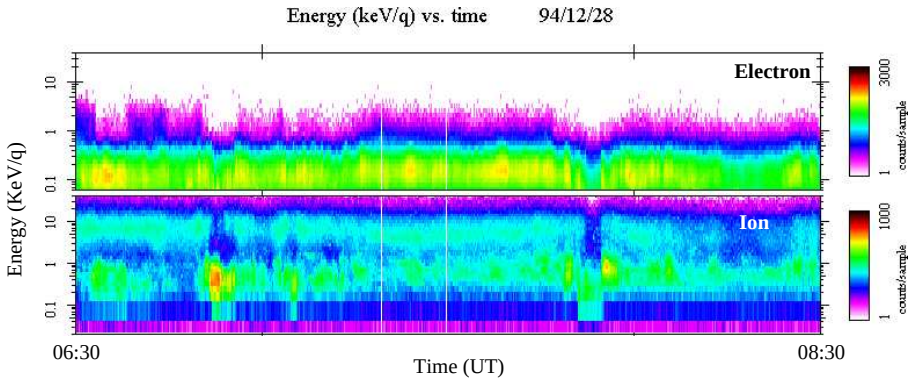

Figure 3.2: The E-t diagram for omni-directional ions (bottom) and electrons (top) observed by Geotail spacecraft. Adopted from Fujimoto et al.[1998].

In contrast to the rich knowledge on the observation of the high-latitude entry process by the reconnection, less is known about the structure of LLBL as well as the entry process via the low-latitude boundary region. Previous crossings of the low-latitude flank magnetopause have indicated the presence of a boundary layer(Sckopke et al., 1981; Mitchell et al., 1987; Phan et al., 1997). Mitchell et al. [1987] pointed out a dependence of the topology of the LLBL on the orientation of the IMF. They found that the LLBL is on closed field lines for northward IMF but is on a combination of closed and open field lines for southward IMF. Sckopke et al. [1981] found that the LLBL is always attached to the magnetopause but its thickness extends to a spatially large scale. They suggested that the boundary layer may be a result of the Kelvin-Helmholtz (K-H) instability at the inner edge of the boundary layer.

The shocked solar wind plasma flowing past the magnetosphere provides a velocity shear whose situation is favorable for the excitation of the K-H instability. Hence, the K-H in-

stability has been considered to be a major contributor to the formation of the LLBL and the mechanism of the direct transportation of the solar wind plasma across the low-latitude boundary. The evidences of the K-H instability growing at the low-latitude boundary have been reported by several authors (Hones et al., 1981; Ogilvie and Fitzenreiter, 1989; Seon et al., 1995; Fairfield et al., 2000). Hones et al. [1981] showed the data indicating the vortical flows which are clockwise in the morning side and counterclockwise in the evening side of the plasma sheet. They believed that the vortical motions are attributed to the excitation of the K-H instability. Recently, Fairfield et al. [2000] reported the detailed event study of the observation of the K-H instability by comparing with their companion paper of the Magneto-Hydro dynamic (MHD) simulation (Otto and Fairfield, 2000). They argued that the multiple crossings of the boundary are due to a K-H wave at the boundary and concluded that the low-latitude boundary of the flanks are K-H unstable and the K-H instability must be an important process for transferring energy, momentum and particles to the magnetotail during times of very northward IMF.

The K-H instability at the magnetospheric boundary has been studied by nonlinear MHD simulations (Miura, 1984, 1992 1995; Wu, 1986; Otto and Fairfield, 2000). Miura [1992] have demonstrated the momentum transport across the boundary by the anomalous (eddy) viscosity which is arisen by the non-linear evolution of the K-H instability and concluded that the K-H instability can be a major contributor for the viscosity as Axford and Hines [1961] suggested. It is only recently that the MHD and kinetic particle simulations have attempted to explain the K-H instability not only as a source of momentum but also as a source of mass (Terasawa et al., 1992; Thomas and Winske, 1993; Fujimoto and Terasawa1994; Fujimoto and Terasawa, 1995; Wilber and Winglee, 1995; Huba, 1996b; Nykyri and Otto, 2001). While the finite gyro radius effect of ions is expected to enhance the mixing rate in time in homogeneous background (Terasawa et al., 1992), in-homogeneity in magnetic field suppresses the mixing which was observed in the homogeneous case (Fujimoto and Terasawa, 1995). Thomas and Winske [1993] also reported the simulation study of a in-homogeneous case and showed the isolated structures on the order of the ion gyro radius are formed which can across the boundary in either direction, although the process cannot explain the diffusive

structure as often observed in the low-latitude boundary layer introduced above. The similar isolated structure was reproduced by the MHD simulation (Nykyri and Otto, 2001) which incorporates the component of the magnetic field parallel to the ambient flow. The detached isolated magnetic island containing the solar wind plasma is produced by the reconnection inside the vortex. Huba [1996] reported the simulation result based on the finite Larmor radius (FLR) MHD equations in a non-uniform background field. The FLR effect introduces the asymmetry in the non-linear development which is dependent on the sign of $\mathbf{B} \cdot \mathbf{\Omega}$, where Ω denotes the vorticity. He suggested an asymmetrical evolution of the K-H instability in the dawn and the dusk side of the magnetotail flanks. In spite of the great challenges by researchers with using both MHD and kinetic particle simulations, no one has succeeded in the transport over the K-H vortex size and the explanation of the broad mixing layer lying in the low-latitude region of the earth magnetosphere.

In this context, the remaining candidate mechanism for explaining more efficient mixing is "turbulence". It is well known that turbulence enhances the mixing and is generated by a three-dimensional hydrodynamical K-H instability (Lasheras and Choi, 1988; Fritts et al., 1996; Palmer et al., 1996). Fritts et al. [1996] demonstrated the comparison of the non-linear development between two- and three-dimensional K-H instability in a stratified shear flow. The stratification introduces the secondary instability in the non-linear stage of the three-dimensional K-H instability. Then longitudinal vortices along with the K-H vortices are generated. Though the numerous experimental studies have shown the excitation of the secondary instability along with the normal K-H vortex (Thorpe, 1985; Lasheras and Choi, 1988), the excitation mechanism is still controversial (Pierrehumbert and Widnall, 1982; Lin and Corcos, 1984) since the huge computational resources are required for the detail study on the onset of turbulence because of its strong non-linearity. In a MHD regime, magnetic field acts for a suppression of a primary and/or secondary instability. In the situation of the low-latitude boundary of the earth introduced above, the tension force of transverse magnetic field is expected to inhibit the generation of the longitudinal vortex. Hence, the problem is fundamentally two dimensional and the generation of turbulence has not been reported in such a situation. In this chapter we show, for the first time, the onset of turbulence from a

normal K-H vortex in a two-dimensional plane. We also propose the mechanism for obtaining the enhanced mixing layer, which can be applied to a variety of situations in particular to the interaction between the solar wind plasma and the earth's magnetosphere.

3.2 Situation in consideration

Figure 3.3 shows the typical crossing of the low-latitude boundary of the earth observed by the Geotail spacecraft (Nishida, 1994). From the top to the bottom panel, shown are the absolute value and three vector components of the magnetic field, the plasma (ion) density, temperature and the x (GSM coordinate) component of velocity. The vertical thick dashed line indicates the boundary which separates the solar wind (specifically, magnetosheath; left side) and the magnetosphere (plasma sheet; right side). In the bottom panel, one can confirm the velocity shear across the boundary which is a free energy for the excitation of the K-H instability. (However, parallel components of the magnetic field, i.e., B_x and B_y are supposed to be suppressing the K-H instability in this event. See more details in chapter 2 on the effect of the parallel component of the magnetic field on the linear growth of the K-H instability.) It is to be noted that the jump in the plasma density and temperature is on the order of two while the strength of the magnetic field fluctuates only in a few nano-teslas across the boundary. This characteristics motivate the author to study how in-homogeneity in plasma affects the non-linear evolution of the K-H instability by using computational approaches. The basic simulation geometry shown in this chapter is summarized in Fig. 2.3. Note that in the present simulations

- the x component of velocity is sheared in the y direction,
- transverse magnetic field is uniform unless otherwise specified,
- and density and temperature vary in the y direction so that the pressure balance is maintained.

The last item is the main topic in this chapter and will be proved to be important for the large extent of the mixing layer as well as for the onset of turbulence.

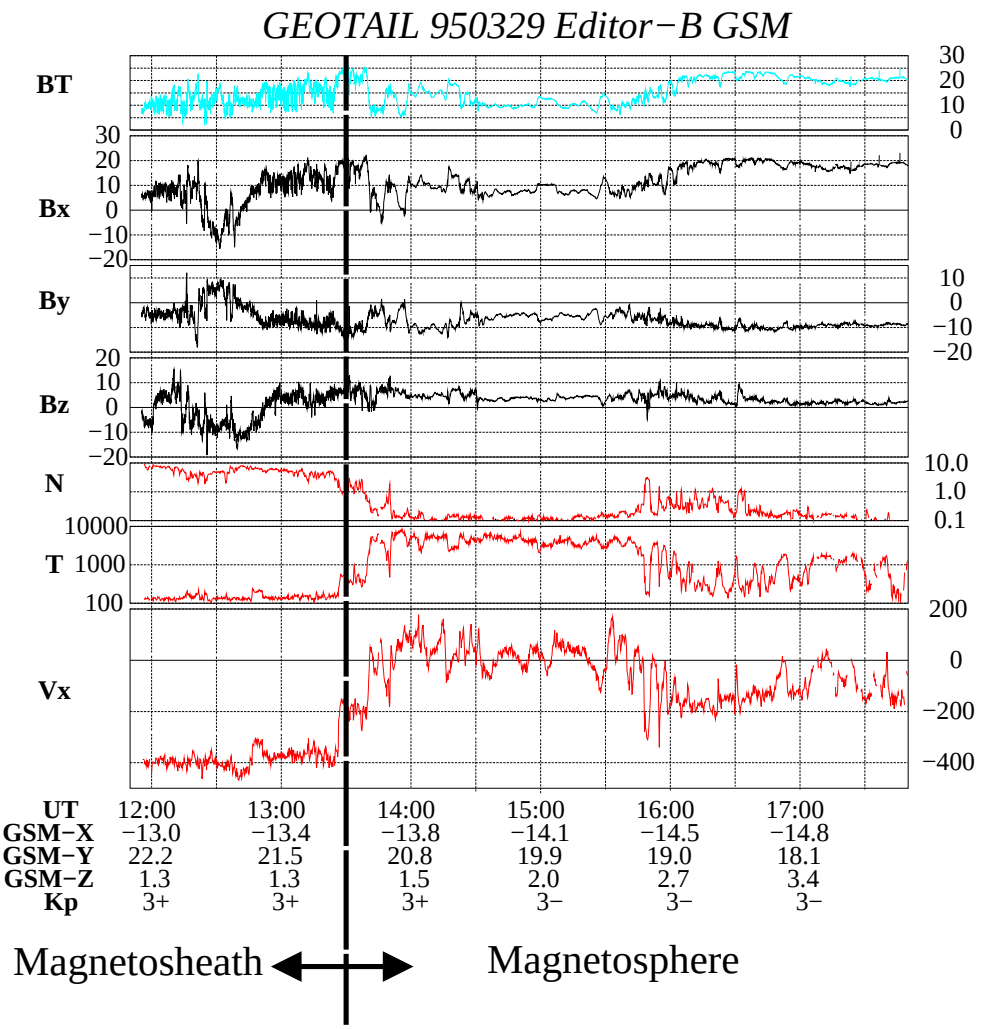

Figure 3.3: An observation of LLBL by Geotail spacecraft on March 29 in 1995. From the top to the bottom panel shown are the absolute value and three vector components of the magnetic field, ion density and temperature, and the x component of the ion velocity. The vertical thick line indicates the boundary which separates the magnetosphere and the solar wind.

3.3 Linear analysis

Here, the effect of in-homogeneity in plasma on the growth rate of the K-H instability is examined in this section. For a zero-thickness boundary layer the growth rate of incompressible K-H instability can be obtained analytically (Chandrasekhar, 1961),

$$\gamma = k_x |\mathrm{V}_1 - \mathrm{V}_2| \sqrt{\mathrm{A}_1 \mathrm{A}_2}, \tag{3.1}$$

where, k_x is a wave number in the direction of the flow, U_1 and U_2 are uniform velocity of the fluids 1, 2 whose uniform density are ρ_1 and ρ_2, respectively, and

$$A_1 = \frac{\rho_1}{\rho_1 + \rho_2}, A_2 = \frac{\rho_2}{\rho_1 + \rho_2}.$$

Compressibility and a finite thickness of a boundary layer, which are not included in the analytic solution, stabilize the growth. Taking account in these effects, the growth rate can be obtained by solving the linearized MHD equations as a eigen value problem (Appendix A) with the following initial conditions.

$$\begin{aligned}
\mathbf{V} &= (V_x(y), 0, 0) \\
\mathbf{B} &= (0, 0, B_z) \\
V_x &= \frac{V_0}{2} \tanh\left(\frac{y}{\lambda}\right) \\
n &= \frac{n_0}{2}\left((1+\alpha) - (1-\alpha)\tanh\left(\frac{y}{\lambda}\right)\right) \\
\beta &= 0.3 \\
V_0 &= -1.0 \\
\alpha &= 0.2, 0.3, 0.4, 0.6, 1.0,
\end{aligned}$$

where λ and α denotes the width of the shear layer and the asymptotic number density ratio relative to the value $n(+\infty)$, respectively. Figure 3.4 shows the results for the different density ratios, α. The growth rate and the wave number are normalized in terms of λ/V_0, and λ, respectively. Since the magnetic field is transverse to the plane which contains the flow motion the only magnetosonic mode is destabilized, whose phase velocity is $\sqrt{c_s^2 + V_A^2}$, where $c_s = \sqrt{\Gamma P/\rho}$ and $V_A = B/\sqrt{4\pi\rho}$ denote the sound speed and the Alfvén speed. Though the

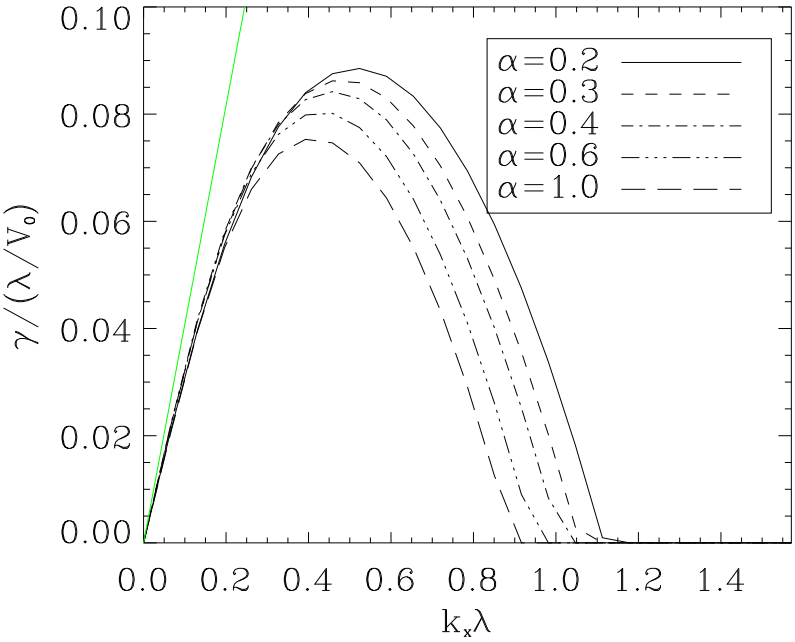

Figure 3.4: The growth rates of the K-H instability for different density profiles. The green line is the growth rate for the incompressible case with the discontinuous velocity profile for α=0.2. (eqn. (3.1))

stratification in density slightly affects on the maximum growth rates, the corresponding wave number, and the eigen mode structure due to the change in the magnetosonic speed or compressibility in the low-density region, the stratification cannot be a new free energy for another instability. (Note that under the gravity force, the stratification acts for the stabilization which is controlled by the Richardson number,

$$R_i = -\frac{g}{\rho}\frac{\partial \rho}{\partial y} \Big/ \left(\frac{\partial V_x}{\partial y}\right)^2 . \tag{3.2}$$

The necessary condition for stability is (cf. Chandrasekhar, 1961)

$$R_i > \frac{1}{4}. \tag{3.3}$$

While in the circumstances now considering the Richardson number is supposed to be quite small ($R_i << 1$) and the stratification does not stabilize the K-H instability, the effect of

the stratification is quite important in the circumstances of the hydrodynamical experiments and in the atmospheric phenomena.)

Figure 3.5 shows the eigen mode structure of the perturbed thermal pressure with the flow vectors of unperturbed and perturbed velocity for (A) $\alpha = 0.2$ and for (B) $\alpha = 1.0$. While the eigen mode structure is symmetric across the boundary (y=0) for $\alpha = 1.0$, a little

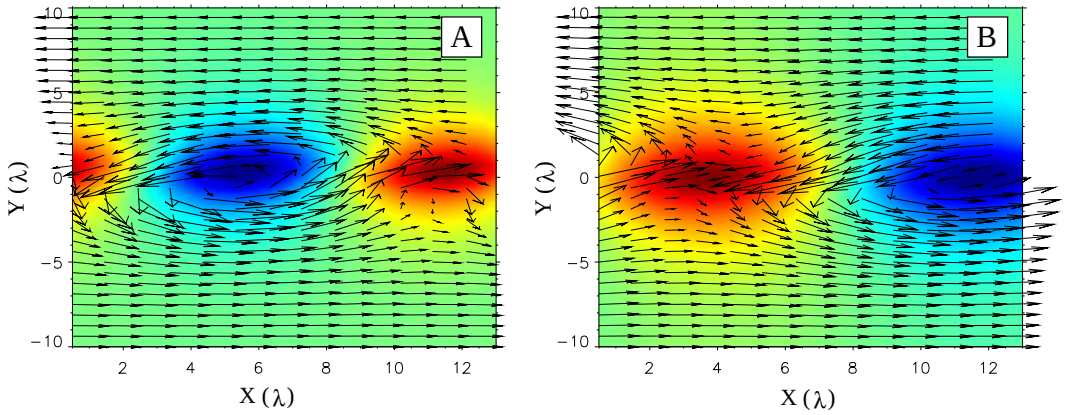

Figure 3.5: The eigen mode structure of the fastest growing mode for (A)$\alpha = 0.2$ and (B)$\alpha = 1.0$. The abscissa and the ordinate shows the x and the y coordinate normalized by the initial shear width λ . The color coded strength shows the power of the thermal pressure of the fastest growing mode. The arrows shows the corresponding perturbed and unperturbed velocity.

asymmetry in the eigen mode structure is confirmed in the result for $\alpha = 0.2$, which is due to the asymmetrical compressibility by the inhomogeneous magnetosonic speed.

3.4 Ideal MHD Simulation

A two-dimensional direct numerical simulation with the conventional MHD equations (Appendix A.1.1) is demonstrated in this section. We solved the equations by 4th-order Runge-Kutta scheme in time and 3rd-order up-wind scheme in space to explore how the stratification affects the non-linear development of the K-H instability.

3.4.1 Simulation parameters and initial conditions

The initial equilibrium is maintained by the constant total (thermal and magnetic) pressure with a sheared velocity profile which varies as $V_x = 0.5V_0\tanh(y/\lambda)$, where λ is a shear scale length and V_0 is a jump in velocity across the shear layer. The 2-D simulation domain has 32 grids per one λ and the dimensions are $L_x = 15.7\lambda, L_y = 20.0\lambda$ so that the system's size in the x approximately corresponds to the wavelength of the fastest growing mode (FGM) (Fig. 3.4, Miura and Pritchett, 1982). The boundary condition is imposed such that there is no mass flow ($V_y = 0$) across the boundaries at $y_b = \pm 10.0\lambda$ and all quantities are periodic in the x direction. In the following simulation runs we adopt Alfvén Mach number $M_A = V_0/V_A = -1.0$, where $V_A = B_0/\sqrt{4\pi\rho_0}$, $\rho_0 = MN_0$, V_A is the Alfvén speed, M, N_0 and B_0 are the ion mass, the equilibrium density and the magnetic field strength at $y_b = +10\lambda$, respectively. The homogeneous transverse magnetic field B_z is set initially so that the initial thermal pressure is constant in the system and plasma beta (β = thermal pressure / magnetic pressure) is set equal to 0.3. The number density profile is provided with a functional form of $N = N_0/2\{(1+\alpha) + (1-\alpha)\tanh(y/\lambda)\}$, where α is the asymptotic number density ratio.

3.4.2 Linear growth

In the linearly growing stage, each simulation runs show the development of the eigen mode with the growth rate as expected from the linear analysis. Fig. 3.6 shows the time development of the FGM (mode 1) integrated in the y direction for (A) $\alpha = 1.0$ and (B) $\alpha = 0.2$. While a good agreement between the simulation result and the linear analysis can be confirmed in the result for $\alpha = 1.0$, the oscillatory behavior of the FGM does not follow simply the linear growth as expected from the linear analysis. This is due to the onset of turbulence which will be introduced in the following subsections.

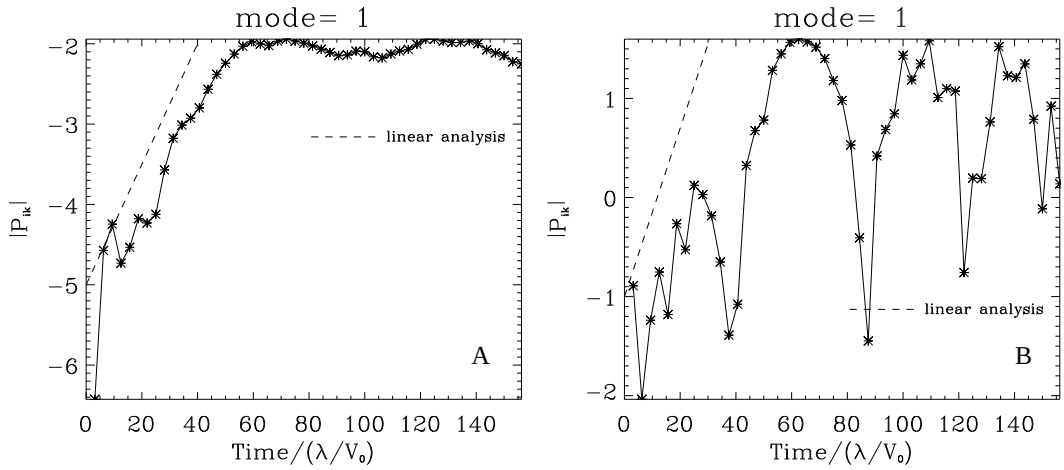

Figure 3.6: The time development of the FGM for (A)$\alpha = 1.0$ and (B)$\alpha = 0.2$. The abscissa shows the time normalized by λ/V_0 and the ordinate shows the power of the Fourier transformed thermal pressure whose mode number corresponds to the K-H instability. The dashed lines in the panels shows the growth rate calculated in the linear analysis in section 3.3

3.4.3 Onset of secondary instabilities in the non-linear stage of the K-H instability

In the non-linear stage, however, the eigen mode develops differently in each run for different α. In the simulation run with $\alpha = 0.2$ the secondary instabilities start growing at a time $t = 84.38\lambda/V_0$ (Fig. 3.7 (B)). At about $X = 8.5\lambda, Y = -2.0\lambda$ and $X = 14.0\lambda, Y = 1.5\lambda$, newly-induced waves grow in the density interface. Furthermore, dense parts of plasma are bent inside the normal K-H vortex. (These two kinds of growing wave are zoomed in the white frame in Fig. 3.7 (B).) As a consequence of such developments of the secondary instabilities the normal vortex structure collapses and the system proceeds to the turbulent flow stage (Fig. 3.7 (C)). In the final stage of the simulation run at $t = 156.25\lambda/V_0$ (Fig. 3.7 (D)) fine structures appear with turbulent flows and the mixing layer approaches the boundary at $y_b = -10\lambda$. In this simulation run two characteristic properties are present: One is the collapse of the normal vortex structure and the other is that the position of the mixing layer moves toward -y direction from the center of the simulation domain. The

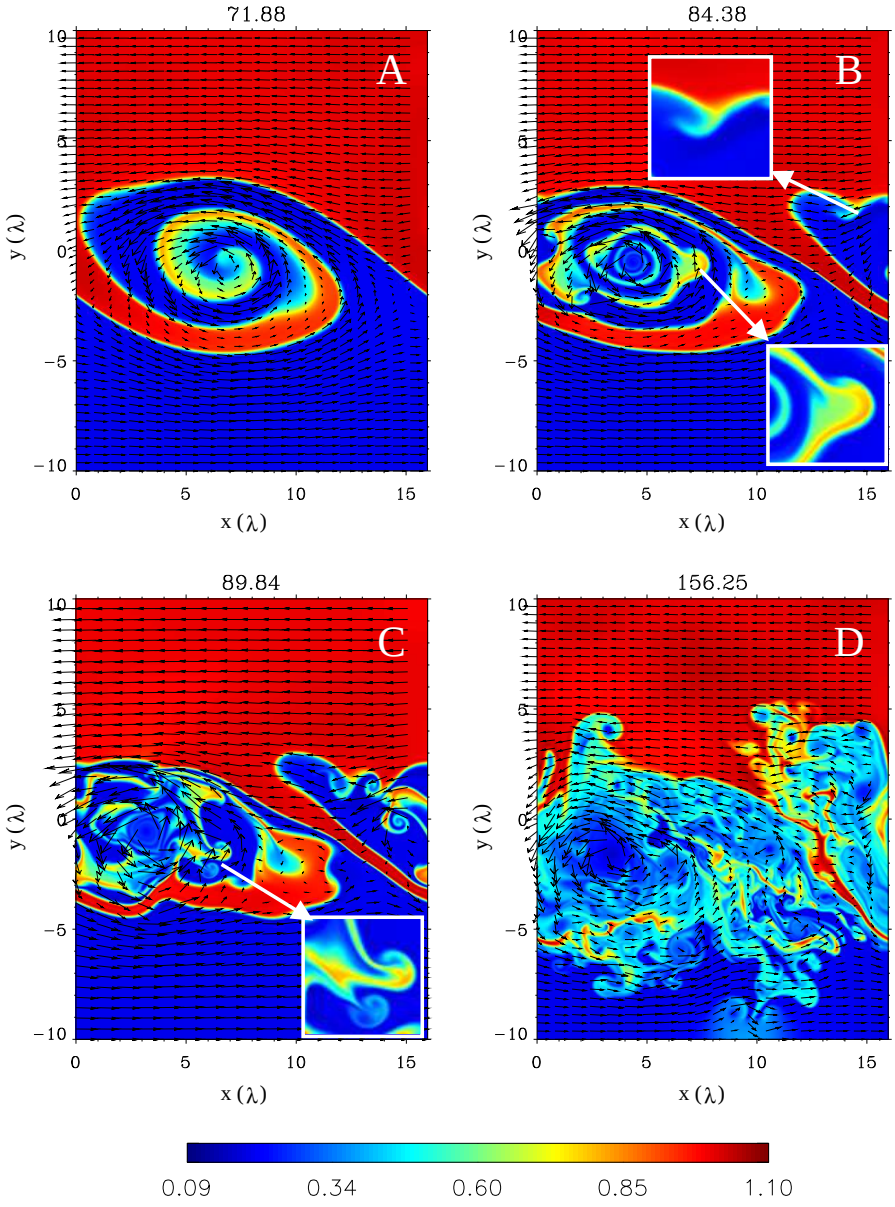

Figure 3.7: Number density profiles with flow vectors for $\alpha = 0.2$ are shown at a time (A) t = $71.88\lambda/V_0$, (B) t = $84.38\lambda/V_0$, (C) t = $89.84\lambda/V_0$, and (D) t = $156.25\lambda/V_0$. The abscissa and the ordinate shows the x and the y coordinate in the unit of the initial shear width, λ. The onset of secondary instabilities are recognized in (B) as zoomed-in the white frames. The mushroom like structure zoomed in (C) reminds the readers of the onset of the secondary Rayleigh-Taylor instability.

former leads the system to the turbulent structure and enhances the mixing in time. The latter introduces the diffusion of fluids from the dense to the tenuous region and enhances the mixing in space.

3.4.4 Energy spectra

The collapse of the normal vortex induces the turbulent flows and enhances the mixing rate in time. To understand the development of the turbulent flows, the energy spectrum is obtained by integrating in the y direction,

$$f(k_x) = \int_{-y_b}^{+y_b} dy \int_0^{L_x} dx (V_x^2(x,y) + V_y^2(x,y)) \exp(-ik_x x). \tag{3.4}$$

As results, the energy spectra (Figs. 3.8 (A) - (C), with time proceeding from the blue to the red line) with the final density profile of each run (Figs. 3.8 (D) - (F), corresponding to thick dark red lines in the spectra) show that their developments depend on α. When $\alpha = 0.2$, while the power of the normal K-H mode remains constant, the energy cascades rapidly to the shorter wave modes as time goes on (Fig. 3.8 (A)). (Note that the strong dissipation in a high wave number region is due to the up-wind scheme.) When $\alpha = 0.6$, the energy also cascades to the shorter wave modes, although their peak values are rather small (Fig. 3.8 (B)). When $\alpha = 1.0$, the energy does not cascade to the shorter wave modes and the normal mode dominates the system (Fig. 3.8 (C)). We fitted the spectra at $t = 156.25\lambda/V_0$ (thick dark red line) with power functions and evaluated the powers for $\alpha = 0.2, 0.6, 1.0$ as -1.32, -1.38, -2.49, respectively.

3.4.5 Baroclinicity inside the K-H vortex

Subsequent small scale vortices born after the onset can be explained by the baroclinic term in the equation of enstrophy in a 2-D transverse magnetic field configuration (Miura, 1997),

$$\frac{\partial}{\partial t} \int\int dxdy (\nabla \times \mathbf{V})^2 = -\int\int dxdy (\nabla \times \mathbf{V})^2 (\nabla \cdot \mathbf{V}) + \int\int dxdy 2 (\nabla \times \mathbf{V}) \cdot \frac{\nabla\rho \times \nabla P_t}{\rho^2}, \tag{3.5}$$

where P_t represents the total pressure which is a sum of thermal and magnetic pressure. The baroclinic term (the second term on the right-hand side of eq. (3.5)) is usually equal to

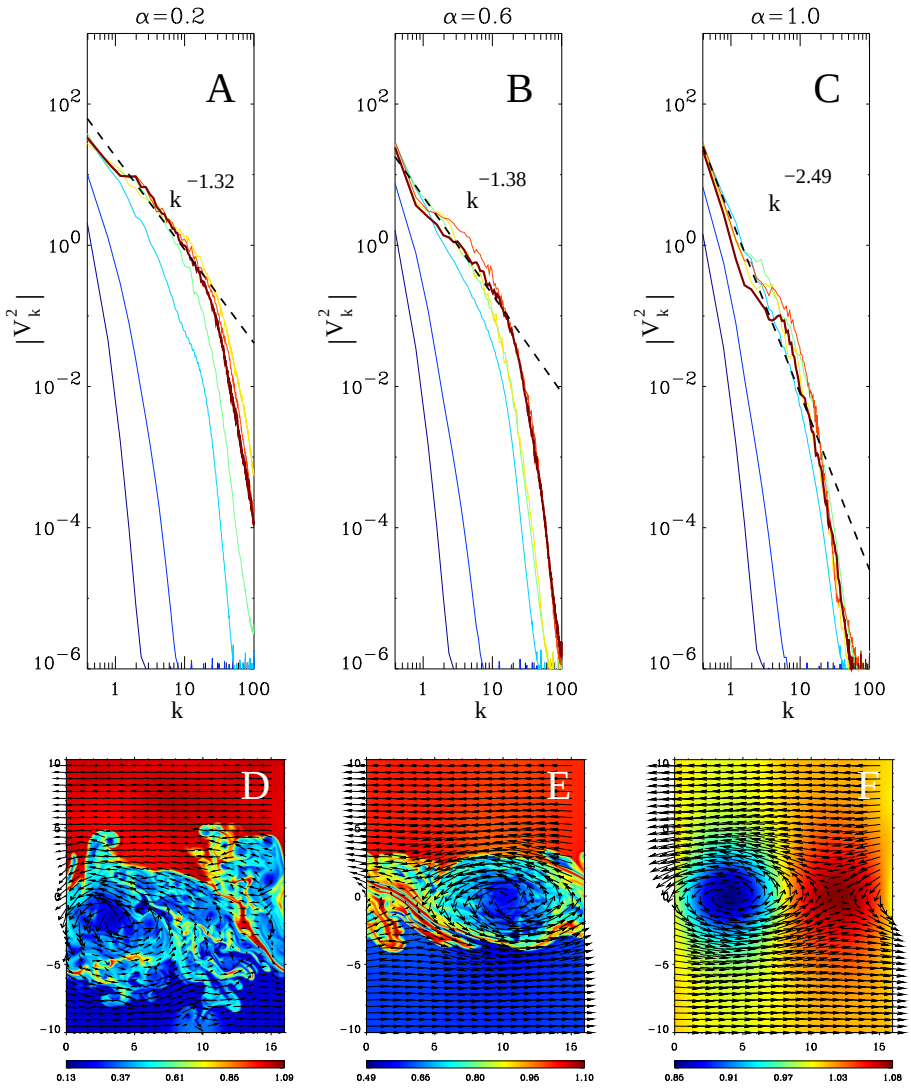

Figure 3.8: The energy spectra are shown in (A) for $\alpha = 0.2$, (B) for $\alpha = 0.6$, and (C) for $\alpha = 1.0$. Time evolution is expressed by the change in color of the line from blue to dark red. (D)-(F) shows the number density profiles with flow vectors which correspond to the energy spectra of the thick dark red lines (t=$156.25\lambda/V_0$) in (A)-(C), respectively. Spectra at $t = 156.25\lambda/V_0$ (thick dark red lines) are fitted with power functions (dash lines in (A)-(C)) and the powers are evaluated as -1.32, -1.38, -2.49, respectively.

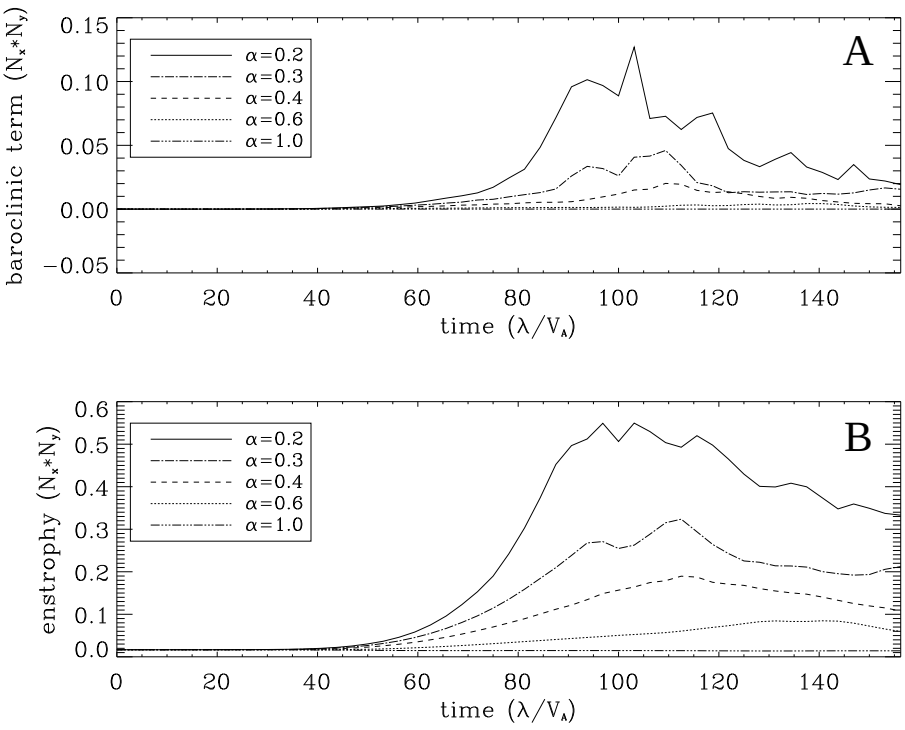

Figure 3.9: Time evolution of (A) baroclinic term and (B) enstrophy in eq. (3.5) are shown for different α. The time and the both two terms are normalized by λ/V_0 and the grid number of the simulation domain ($N_x \times N_y$). Solid, dash-dotted, dash, dotted, and dash-3-dotted lines correspond to the result for $\alpha = 0.2, 0.3, 0.4, 0.6, 1.0$, respectively.

zero (barotropic) as seen in the simulation run with $\alpha = 1.0$ (Fig. 3.9(A)). In such a case the total amount of the enstrophy is slightly reduced by compressibility and the viscosity (eq. (3.5) and Fig. 3.9(B)). In the simulation run with $\alpha = 0.2$ the baroclinic term is also equal to zero initially. As the K-H mode develops, however, the baroclinic term is no longer equal to zero locally because of the rolling up motion and starts increasing in the non-linear stage until $t = 90\lambda/V_0$ (Fig. 3.9(A)). Figure 3.10 shows the profile of (A)number density, (B)baroclinicity, and (C)vorticity taken at $t = 93.75(\lambda/V_0)$. As indicated from eq. (3.5), the vorticity appears associated with the baroclinicity in (B). These behaviors can be seen in other runs, although the intensities are smaller with larger α (smaller heterogeneity). As a result from the equation (3.5), the enstrophy integrated in the simulation domain also increases with time until $t = 100\lambda/V_0$ (Fig. 3.9(B)). These indicate that the violation of the

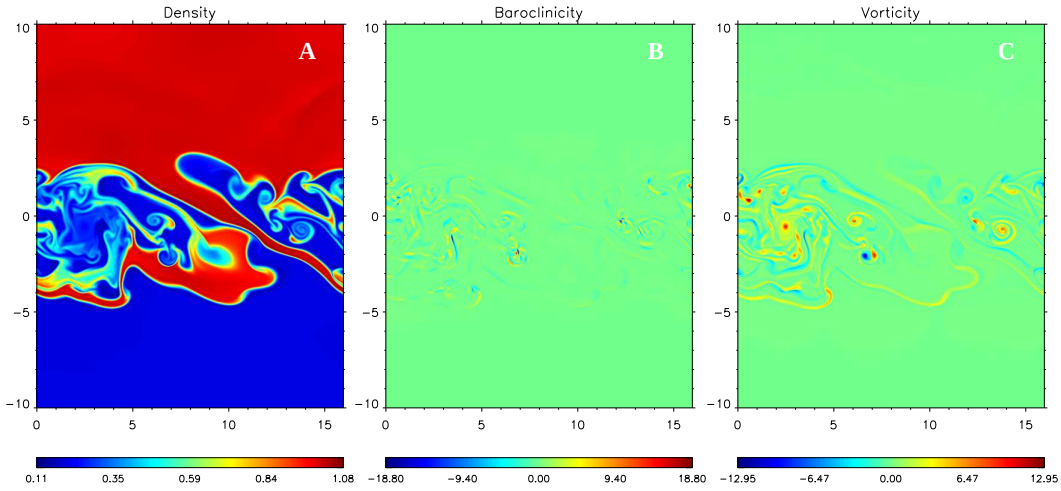

Figure 3.10: The snapshots of (A) Number density, (B) baroclinicity, and (C) vorticity taken at $t = 93.75(\lambda/V_0)$ are shown.

barotropy, or, the new born of baroclinicity inside the normal K-H vortex produces vortices one after another subsequently.

3.4.6 Secondary Kelvin-Helmholtz and Rayleigh-Taylor instability

What violates the barotropy? Examining in detail, it is found that the onsets of the turbulence are triggered by two kinds of secondary-induced instabilities due to the stratification in density (Fig. 3.7 (B)). The one is the K-H instability and the other is, more importantly, the Rayleigh-Taylor (R-T) instability (Chandrasekhar, 1961; Sharp, 1984). (Note also the white small frame in Fig. 3.7 (C) which emphasizes the mushroom like structure that characterizes the non-linear development of the R-T instability.)

The secondary K-H instabilities are excited by the strong shear flows inside the normal vortex. In the linear stage of the normal K-H instability, the unstable eigen mode of the perturbed total pressure accelerates the fluid elements, which makes the tenuous fluid turn faster and the dense fluid turn slower. Note also that one can confirm the sharp stripe pattern of the density interface, across which the flow velocity is sheared, inside the vortex (Fig. 3.7 (A)). This is a result of rarefaction and compression by the fast magnetosonic wave

whose phase velocity is faster in tenuous region and slower in dense region. The quite sharp interface of density (velocity), whose width is maintained by a numerical dissipation, leads the growth rate of the secondary K-H instability to be approximated as in the equation (3.1). The velocity difference is determined from the force balance equation,

$$\rho_1 \frac{V_1^2}{r_1}\hat{r} = \rho_2 \frac{V_2^2}{r_2}\hat{r} = -\nabla_r P_t, \tag{3.6}$$

where $\hat{r}$ denotes a unit vector in radial direction originating at the center of the normal vortex, ∇_r denotes the differential operator with respect to the radial direction, and the subscripts 1 and 2 denote the dense and tenuous parts of the fluid, respectively. Comparing one part with the other by assuming $r_1 \approx r_2$, the velocity difference becomes

$$\frac{V_1}{V_2} = \sqrt{\frac{\rho_2}{\rho_1}} = \sqrt{\alpha}, \tag{3.7}$$

$$\Delta V = V_2 - V_1 = V_2(1 - \sqrt{\alpha}). \tag{3.8}$$

Along with the equation (3.1),

$$\gamma = k_x |\mathrm{V}_1 - \mathrm{V}_2| \sqrt{\mathrm{A}_1 \mathrm{A}_2},$$

$$\mathrm{A}_1 = \frac{1}{1+\alpha}, \mathrm{A}_2 = \frac{\alpha}{1+\alpha},$$

the growth rate of the secondary K-H instability therefore has a functional form of

$$\gamma \propto \frac{1-\sqrt{\alpha}}{1+\alpha}\sqrt{\alpha}, \tag{3.9}$$

which is affected by the stratification in density.

The other secondary instability is also attributed to the vortex motion. The centrifugal force can act as a radial effective gravity force $\mathrm{g_{eff}}$ on the fluid medium. Under the gravity force the well-known Rayleigh-Taylor instability grows when $\nabla\rho \cdot \mathbf{g} < 0$ (Chandrasekhar, 1961). Consequently, the density interface where $\nabla\rho \cdot \mathbf{g}_{\mathrm{eff}} < 0$ inside the vortex is unstable to the R-T instability due to the radial centrifugal force. The growth rate is analytically given for a thin boundary layer as

$$\gamma = \sqrt{\frac{(1-\alpha)}{(1+\alpha)}\mathrm{g_{eff}}\mathrm{k}} \tag{3.10}$$

and it shows that the growth rate of the R-T instability is

$$\gamma \propto \sqrt{\frac{(1-\alpha)}{(1+\alpha)}}, \tag{3.11}$$

which is also a function of the stratification, α. Assuming the normalized effective gravity $g_{\rm eff}$ is

$$\begin{aligned} \left|\frac{g_{\rm eff}}{\Omega_{\rm gi} V_A}\right| &= \frac{V^2}{r} \sim \frac{(V_0/2)^2}{0.25\lambda_{\rm FGM}} \\ &= \frac{V_0^2}{4\pi\lambda} \\ &= 0.08, \end{aligned} \tag{3.12}$$

the linear analysis gives the growth rate of the secondary R-T instability. The other parameters used in the analysis are $\alpha = 0.2$, plasma $\beta = 0.3$ and the width of the boundary layer which is similar to the initial shear layer width λ. This condition can estimate the minimum value of the growth rate. Figure 3.11 shows the result of the linear analysis of the secondary R-T instability (asterisk) along with the growth rate of the normal K-H instability (open square). The solid line shows the analytical result obtained by the equation (3.10). As a result, the growth rate of the secondary R-T instability is more than twice larger than that of the normal K-H instability. Actually, the growth rate of the secondary R-T instability has a value between the minimum (asterisk) and the analytical result (solid line), the result of the linear analysis justifies the R-T instability as a secondary instability observed in the simulation for $\alpha = 0.2$. Figure 3.12 shows the simulation results of the time profiles of the modes $k_x\lambda = 0.39 \sim 2.36$. The red and black solid lines shows the result for $\alpha = 0.2, 1.0$, respectively. As is evident from Figure 3.12, the shorter wave modes grow faster than the normal K-H mode and saturate larger in amplitudes in $\alpha = 0.2$ than in $\alpha = 1.0$.

Both secondary instabilities show that the growth rates depend on the inhomogeneity in density. Furthermore, the growth rates are positive functions of the wave number. This means that the free energy of the inhomogeneity in density is transported to shorter wave modes and as a result, turbulence takes place.

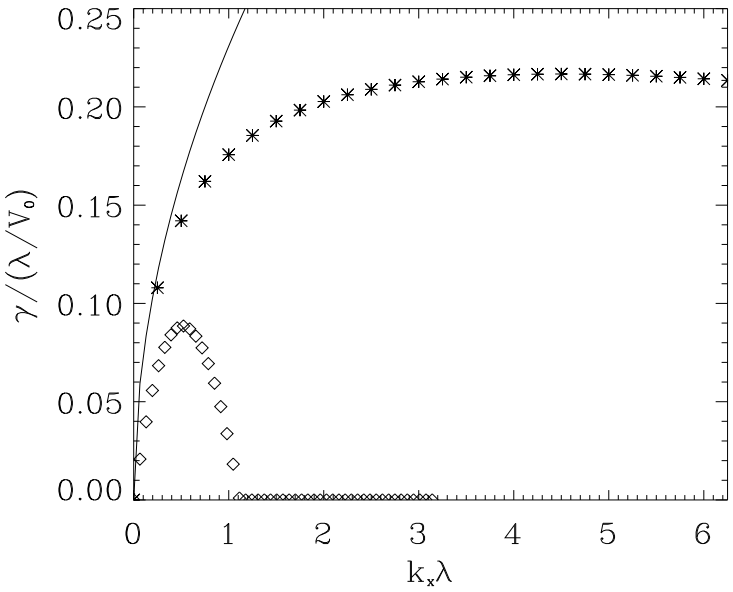

Figure 3.11: Comparison of the growth rate between the normal K-H and the secondary R-T instability. The asterisk shows the result for the secondary R-T instability obtained by the linear analysis. The open square shows the growth rate of the normal K-H instability. The solid line shows the analytical result of eq. (3.10).

3.4.7 Width and position of the mixing layer

Turbulence enhances the mixing of the two media. To estimate the mixing area we fitted the average profile of V_x with a functional form of $0.5V_0\tanh((y-y_0)/\mu)$ with two free parameters of the width μ and the position y_0. The width of the mixing layer increases with time through two phases in the run with $\alpha = 0.2, 0.3$ (Fig. 3.13(A)). The first phase, which can be seen in all simulation runs until $t = 60\lambda/V_0$, corresponds to a linear growth of the normal K-H instability. (Slight differences in time evolution attribute to the slight differences in growth rates. See Fig. 3.4) The second phase is clearly seen in the run with $\alpha = 0.2$ and $\alpha = 0.3$ after the first phase and the beginning of the second phase at $t = 80\lambda/V_0$ in $\alpha = 0.2$ corresponds to the onset of the secondary instabilities (Fig. 3.7(B)). The width of the mixing layer increases from the first saturation level while in other simulation runs

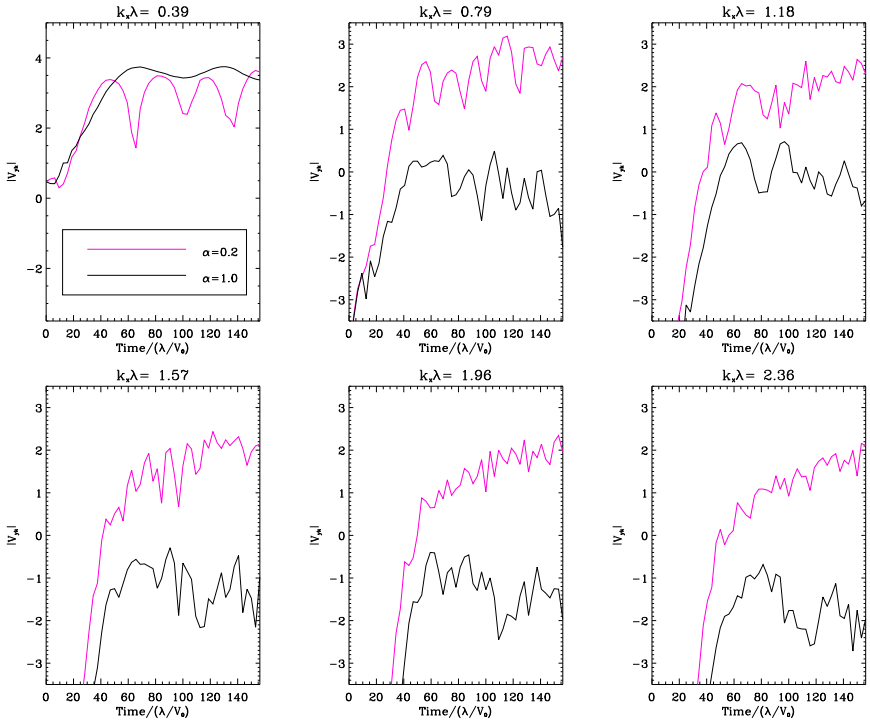

Figure 3.12: Time profiles of the modes $k_x\lambda = 0.39 \sim 2.36$ are shown for the results of $\alpha = 0.2$ (red) and $\alpha = 1.0$ (black).

it oscillates within a certain level. This time profile indicates that turbulence enhances the mixing in space. A second point to be noted is the time development of the position of the mixing layer (Fig. 3.13(B)). In all simulation runs except for $\alpha = 1.0$ the position of the mixing layer shifts toward the -y direction until $t = 60\lambda/V_0$ and the displacement is larger for smaller α. This corresponds to the linear growth of the normal K-H instability whose turning over motion weakly induces the R-T instability at the outer edge of the vortex. The stability condition $\mathbf{g_{eff}} \cdot \nabla n > 0$ introduces the asymmetry in the y direction, that is, it is unstable to the R-T instability in the negative y region of the outer edge of the vortex whereas the opposite side is stable. Hence the mixing layer seems to shift toward the -y direction. After that the displacement again starts increasing in the run with $\alpha = 0.2$ and weakly in $\alpha = 0.3$ at $t = 100\lambda/V_0$ while stays almost constant in other runs. This additional displacement starts after the onset of turbulence. Examining in detail, we find that the displacement is accompanied by the R-T instability at the outer edge of the normal K-H vortex where the

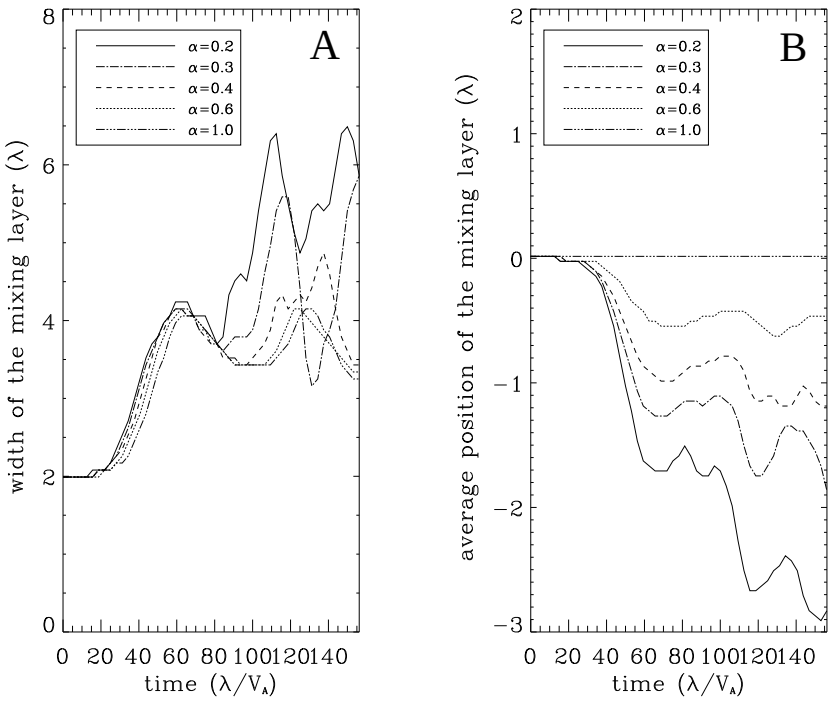

Figure 3.13: Macroscopic properties are shown for different α. The profile of V_x averaged over the x direction is fitted with a functional form of $0.5V_0\tanh((y-y_0)/\mu)$ with two free parameters of width μ and position y_0. Shown are the time evolution of (A) the width μ and (B) the position y_0 in the unit of the initial shear width λ. The second phases at t=$80\lambda/V_0$ in (A) and (B) for $\alpha = 0.2, 0.3$ correspond to the onset of turbulence and indicate that the turbulence effectively enhances the mixing of two media and the transport of dense fluid to the tenuous region.

dense parts of fluid are sandwiched between tenuous fluids (red part between blue colored fluids in Fig. 3.7(B)). At first, the secondary K-H instabilities grow at the two interfaces since there are velocity differences across the interfaces. Accordingly, the flow is bent and the resulting wavy structure induces the R-T instability. Mass exchange is a basic element of the R-T instability and this characteristic introduces the transport of the dense fluid to the tenuous region at the edge of the normal vortex. (There is no mass transport at the opposite side of the normal vortex since $\mathbf{g} \cdot \nabla n > 0$.)

3.4.8 Effect of numerical resolution on the secondary instability

The thinning of the density interface during the non-linear development of the normal K-H instability is a key mechanism for the onset of the secondary instabilities. In MHD regime, only the numerical dissipation of the up-wind scheme used in the simulation preserves the steepening of the density interface. To explore the effect of the numerical resolution on the development of the K-H instability three kinds of MHD simulations with various numerical resolutions are examined. Figure 3.14 shows the similar result of the Figure 3.13 but for $\alpha = 0.2$ with the various numerical resolutions. While in the linearly growing

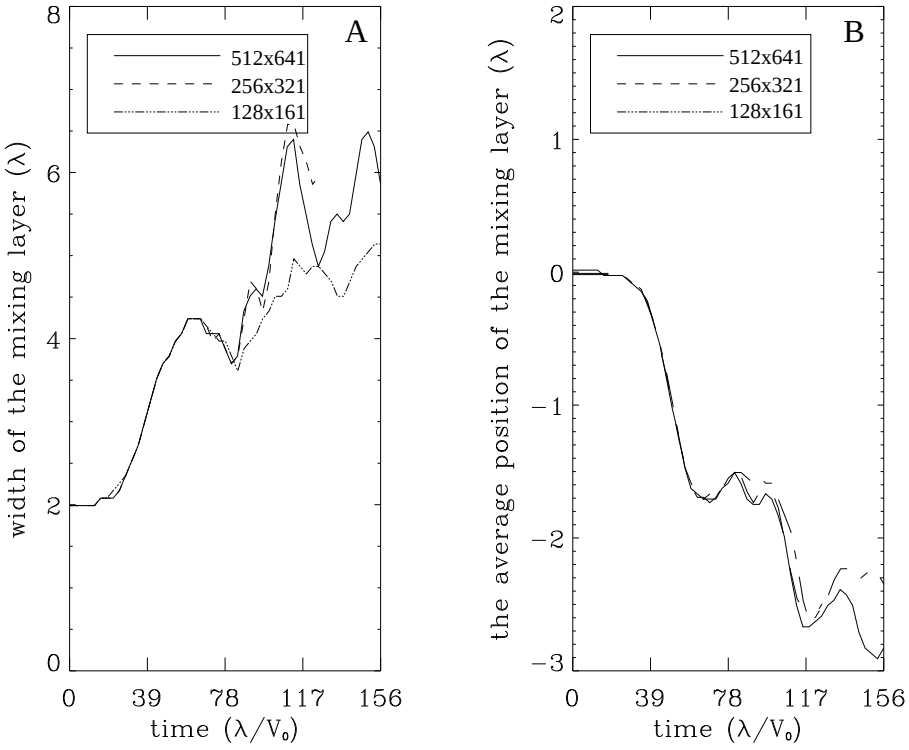

Figure 3.14: Macroscopic properties for $\alpha = 0.2$ are shown for three numerical resolutions in the same format of Fig. 3.13.

stage three simulation results show the same profile, the difference between the result for the resolution 128×161 and the others (256×321 and 512×641) appears from the time $t = 80\lambda/V_0$ at which the secondary instabilities start growing. In the case of the resolution 128×161 the numerical dissipation strongly inhibits the onset of turbulence and as a result,

it macroscopically changes. Although the difference between the result of the resolution 256×321 and 512×641 exists microscopically, the numerical dissipation is small and it does not alters the macroscopic structure.

3.4.9 Effect of inhomogeneity in magnetic field

The mechanism of the onset of the turbulence and the resultant mass transport to the tenuous region shown in this section is fundamentally hydrodynamic since one can obtain the same result if the magnetosonic wave is converted to the sonic wave. In space and astrophysical phenomena, however, there is also a magnetic field interface where there is a velocity shear interface. To elucidate the effect of inhomogeneity in magnetic field (thermal pressure) on the non-linear development we have also carried out the simulation of an in-homogeneous transverse magnetic field case maintained by in-homogeneous temperature fluids with a homogeneous density profile. Initial condition is similar to that of the case in the previous subsections except that the transverse magnetic field is non-uniform in the y direction with the functional form of

$$\mathrm{B_z} = \frac{\mathrm{B_0}}{2}\left((1+\mathrm{br}) + (1-\mathrm{br})\tanh\left(\frac{\mathrm{y}}{\lambda}\right)\right), \tag{3.13}$$

where br denotes the asymptotic ratio of the magnetic field strength relative to the value at $\mathrm{y} = +\infty$. Thermal pressure is given so that the pressure balance

$$\mathrm{P} + \frac{\mathrm{B_z^2}}{8\pi} = \text{constant} \tag{3.14}$$

is satisfied. As a result for $\mathrm{br} = 0.2$ shown in Figure 3.15, we could not obtain any turbulent mixing processes in this parameter regime. The effect of inhomogeneity in magnetic field, however, can be important in a kinetic regime. Recently, Nakamura and Fujimoto reported the importance of the electron inertia on the K-H instability by the two fluid MHD simulation. They pointed out that the current driven instability, current sheet kink instability (Suzuki et al., 2002) triggers the onset of secondary instability and the collapse of the K-H vortex. This mechansim results the enhanced mixing of plasmas. Furthermore, the lower-hybrid drift instability is also expected at the boundary and exploring the coupling of these

micro instabilities with the macroscopic K-H instability is a exciting task. The non-linear development of the K-H instability in arbitrary magnetic field geometries in a kinetic regime is still remained as a future work.

3.5 Full particle simulation

In a MHD regime only the numerical dissipation determines the smallest scale. The steepening of the density interface is maintained by the numerical dissipation, the strong dissipation in the energy spectrum (Fig. 3.8) is also a numerical one, and the mixing shown in the Figure 3.7 is caused by the numerical dissipation. In magnetospheric plasma on which the present dissertation is focusing the mean-free path of the particle is about one AU which is much larger than the scales of the magnetospheric phenomena. Hence, the collision which is a source of energy dissipation cannot be expected and alternatively, the anomalous diffusion by the enhanced electrostatic and/or electromagnetic waves induced by the secondary instabilities is expected in this circumstance. To elucidate what acts as the dissipation that determines the finest scale, the study with the full particle simulation is demonstrated in this section.

3.5.1 Initial condition

Initial conditions of the fluid parameters are similar to that in the ideal MHD simulation as shown in Figure 2.3. The other parameters which are unique in the kinetic treatment are

$$\frac{\mathrm{M}}{\mathrm{m}} = 16, \tag{3.15}$$

$$\frac{\omega_{\mathrm{ge}}}{\omega_{\mathrm{pe}}} = 0.35, \tag{3.16}$$

$$\frac{\lambda}{\mathrm{r_{gi}}} = 4.0, \tag{3.17}$$

$$\frac{\mathrm{r_{gi}}}{\Delta} = 8.0, \tag{3.18}$$

where M and m, ω_{ge}, ω_{pe}, $\mathrm{r_{gi}}$, and Δ denote ion and electron mass, the electron gyro frequency, the electron plasma frequency, the ion thermal gyro radius and the grid size. Each parameters

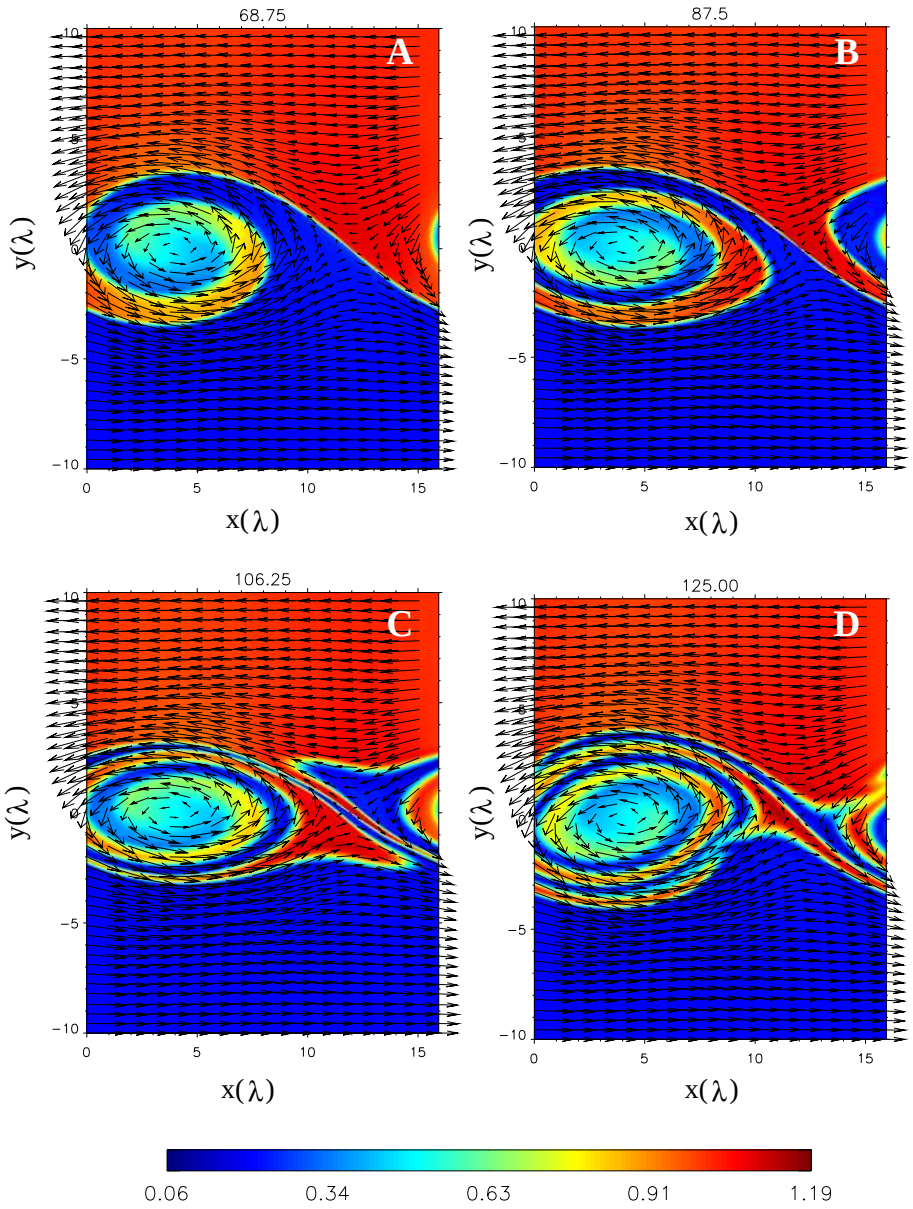

Figure 3.15: Magnetic field profiles with flow vectors for br = 0.2 are shown at a time (A) t = $68.75\lambda/V_0$, (B) t = $87.5\lambda/V_0$, (C) t = $106.25\lambda/V_0$, and (D) t = $125.00\lambda/V_0$ in the same format of the Fig. 3.7. No development of the turbulence is confirmed in the absence of the stratification.

of ω_{ge}, ω_{pe}, and r_{gi} are the values calculated in the region $y_b = +10\lambda$. Parameters adopt in the above equations indicate that

- the small mass ratio as compared to the real mass ratio of 1836 is due to the limited computational resources (eqn. (3.15)),
- weak magnetic field condition is expressed by the eq. (3.16) which is on the order of 10^{-2} in the earth magnetosphere,
- and equation (3.17) guarantees the scales of the system to be hydrodynamic.

On loading particles of ion and electron;

- Particles of both ion and electron are loaded according to the maxwell distribution function, whose first moment reveals the velocity profile, $V_x(y) = V_0/2 \tanh(y/\lambda)$ and the second moment satisfies the pressure balance.
- Particles are distributed in the simulation domain so that the density profile becomes as $N = N_0/2\{(1+\alpha)+(1-\alpha)\tanh(y/\lambda)\}$ by using the cumulative distribution function of the density profile (Birdsall and Langdon, 1991)
- Small charge is added inside the shear layer so as to satisfy the Gauss' law since the y component of the electric field $E_y(y) = -V_x(y)B_z$ is not uniform in the y direction.

The number density along with the plasma parameters are summarized for each simulations in table 3.1, in which N_{SW} and N_{MSP} denote the number density at the boundary $y_b = +10\lambda$ and $y_b = -10\lambda$ modeling the solar wind and the magnetosphere. As in the ideal MHD case the parameter α is used to explore how the stratification affects the non-linear development of the K-H instability in a kinetic regime.

3.5.2 Linear growth

In the linearly growing stage, the K-H mode does not behave simply as expected from the linear theory because of the kinetic effects of the ions. Figure 3.16 shows the time

Table 3.1: Plasma parameters used in the simulations in this chapter.

λ/r_{gi}	V_0/V_A	α	N_{SW}	N_{MSP}	β_{ion}	$\beta_{electron}$	M/m	ω_{ge}/ω_{pe}
4.0	-1.0	0.1	160	16	0.15	0.15	16	0.35
4.0	-1.0	0.2	80	16	0.15	0.15	16	0.35
4.0	-1.0	1.0	128	128	0.15	0.15	16	0.35

development of the y component of the perturbed velocity whose mode number corresponds to the FGM for (A) $\alpha = 1.0$ and (B) $\alpha = 0.2$ (solid lines) along with the results obtained in the linear analysis (dashed lines). While the simulation result for $\alpha = 1.0$ shows a good

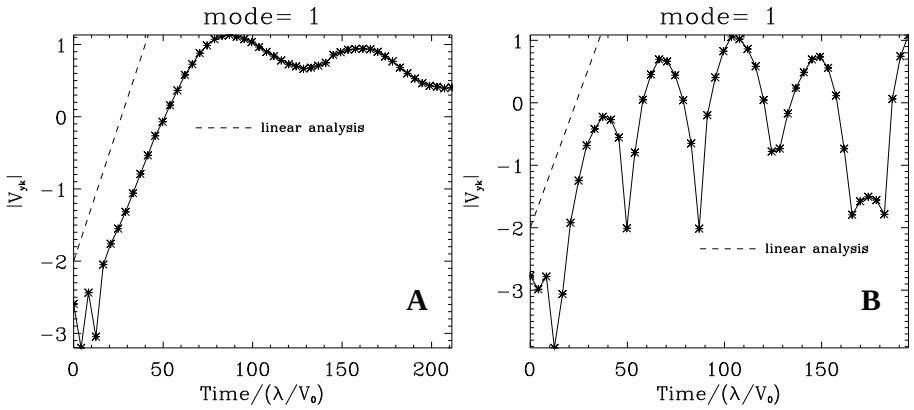

Figure 3.16: The time development of the FGM for (A)$\alpha = 1.0$ and (B)$\alpha = 0.2$ in the same format of the Fig. 3.6 except that the ordinate shows the power of the y component of the Fourier transformed perturbed ion velocity. The dashed lines in the panels shows the growth rate calculated in the linear analysis in section 3.3

agreement with the linear analysis (Fig. 3.16(A)), a little difference between the result for $\alpha = 0.2$ and the analytic one can be seen in Fig. 3.16(B). Although the stabilization of the K-H instability by the finite gyro radius effect (Pritchett and Coroniti, 1984; Huba, 1996b) of hot ions in the tenuous region can be operative, less numbers of hot ions do not stabilize the K-H mode substantially.

3.5.3 Onset of the secondary R-T instability

In the non-linear stage of the K-H instability, the difference from the ideal MHD appears. Figure 3.17 shows the snapshots of the simulation result for $\alpha = 0.2$. Color intensity reveals the ion number density and the contour lines are of the electrostatic potential which approximately correspond to stream lines of the fluid. At a time $t = 62.15\lambda/V_0$ during the first turning over motion of the K-H instability the secondary instability grows at the outer edge of the vortex. The fact that the secondary instability grows at only the density interface where the effective gravity acceleration, $g_{\rm eff}$, by the centrifugal force satisfies the condition $\mathbf{g}_{\rm eff} \cdot \nabla\rho < 0$ justifies the secondary instability as a Rayleigh-Taylor instability which is also observed in the previous MHD simulation. It is also to be noted that the particles initially located in the region $y > 0$ reach the opposite boundary. Since the density stratification triggers the onset of the R-T instability (eq. (3.10)), the particles are transported radially toward the tenuous region.

The effective transport by the secondary R-T instability can also be confirmed by the orbits of an ion and an electron for $\alpha = 0.2$ which are shown in Figure 3.18 and 3.19. Both the ion and the electron initially follow the motion of the K-H instability which is characterized by the circuit of the orbit (Fig. 3.18(A) and Fig. 3.19(A)). In the later part of the simulation both two particles suddenly changes their direction on the way in the circuit and move toward the radial direction centered on the middle of the vortex. The time, $t \sim 80\lambda/V_0$, when the particles abruptly change the direction is corresponds to the onset of the secondary R-T instability.

3.5.4 Mixing rate

As a result of the onset of the turbulence, mixing of the plasmas which initially located in the region $y > 0$ and $y < 0$ is enhanced. Figure 3.20 shows the time profiles of the mixing rate for $\alpha = 1.0, 0.2, 0.1$. The mixing rate for $\alpha = 1.0$ shows the same result in Chapter 2 indicating that the well mixed region is located along the boundary, which is stretched and deformed by the evolution of the K-H instability and the mixing scales of time and space are

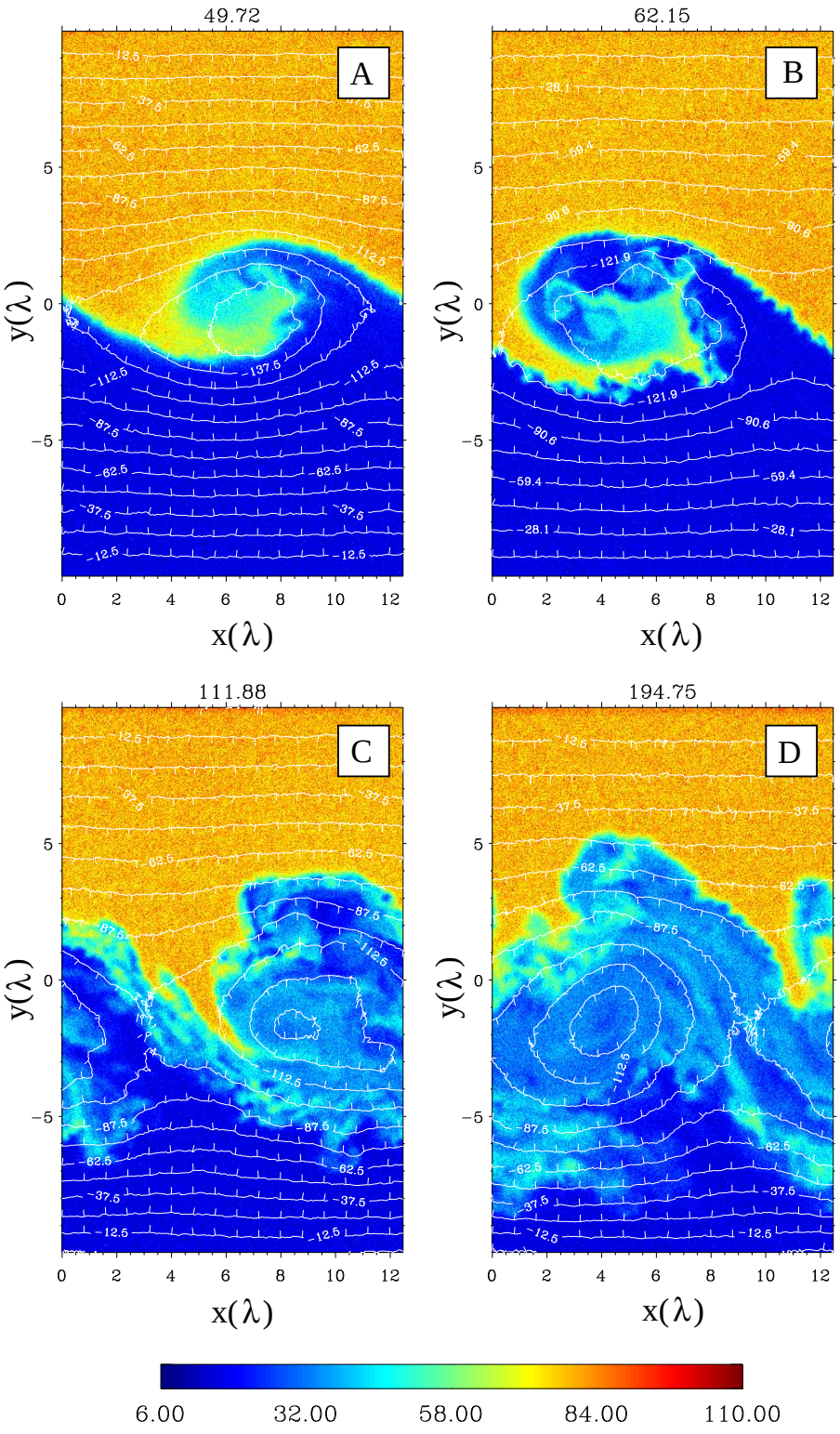

Figure 3.17: Number density profiles with contour lines of the electrostatic potential for $\alpha = 0.2$ are shown at a time (A) t $= 49.72\lambda/V_0$, (B) t $= 62.15\lambda/V_0$, (C) t $= 111.88\lambda/V_0$, and (D) t $= 194.75\lambda/V_0$ in the same format of the Fig. 3.7

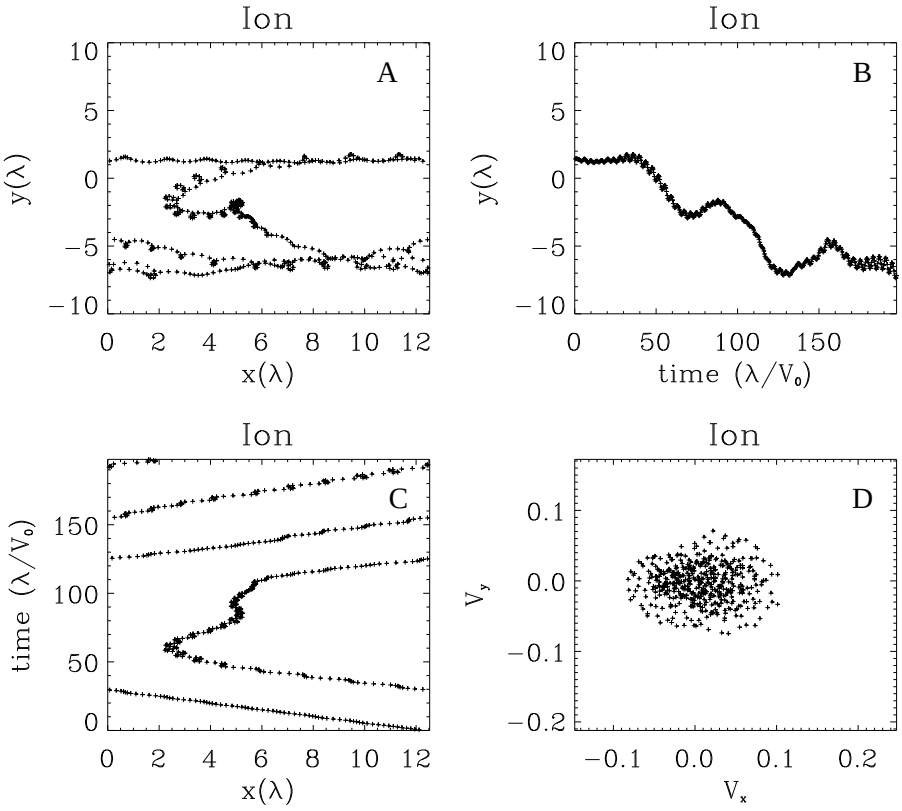

Figure 3.18: (A)The orbit in the simulation domain, (B) the time development of the y coordinate and (C)the x coordinate, and (D)the orbit in a phase space are shown. The coordinate x and y are normalized by the initial shear width λ, the time is normalized by the parameter λ/V_0, and the velocity is in the unit of the speed of light.

determined by the K-H instability. In the case of $\alpha = 0.2$ and $\alpha = 0.1$, however, much faster and broader mixing profiles are obtained in Figure 3.20. In the result of both the ion and the electron, sudden increases in the mixing rate are observed from $t = 50\lambda/V_0$ and their slopes are much steeper than that in the homogeneous case ($\alpha = 1.0$).

At a time $t = 50\lambda/V_0$ corresponds to the onset of small scale modes whose time developments are shown in Figure 3.21. The y component of the Fourier transformed perturbed ion velocity is integrated in the y direction to obtain the power of the wave propagating in the x direction. As can be seen from Figure 3.21, waves of small mode numbers from 4 to 6 start growing at about $t = 30\lambda/V_0$ which almost coincide with the strong increases in the

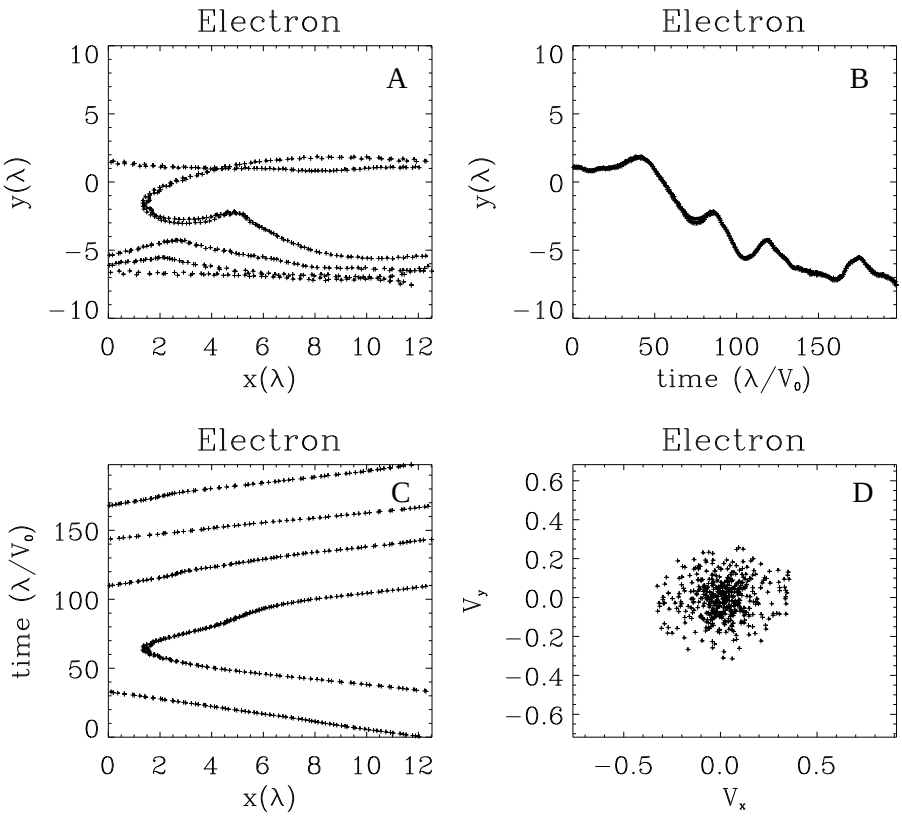

Figure 3.19: Same profiles as shown in Fig. 3.18 but for the electron.

mixing rate. Hence the new born of the small scale waves are expected to be an efficient mixing mechanism.

In a collision-less plasma transverse magnetic field confines the plasma and mixing area of two plasmas should be within a scale of particle's gyro radius. The mixing rates of ion's and electron's integrated in the simulation domain, however, reveal almost the same profile as shown in Figure 3.20. Figure 3.22 shows the mixing rate of ion and electron snapshotted at $t = 66.3\lambda/V_0$, which is just after the onset of the secondary R-T instability. Macroscopically, well mixed regions are concentrated in the contact interface of the density and the spread of the mixing area is on the scales of the particle's gyro radius. Microscopically, however, the electron density interface are strongly deformed with fine scale structures as if they fill in the cloud of the ions' mixing area.

Deformation of the electron density interface is caused by the strong electric field excited

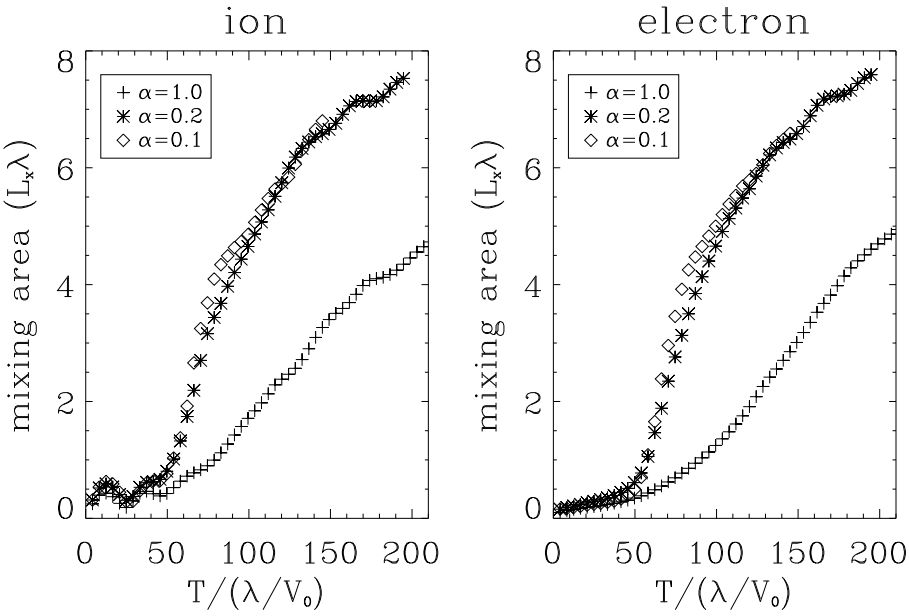

Figure 3.20: The time profiles of the mixing rates for (A) the ion and (B) the electron in the same format of Fig. 2.9. In each panels cross(+), asterisk(*), and open diamond mark the result for $\alpha = 1.0, 0.2, 0.1$, respectively.

by the secondary R-T instability. In a two fluid MHD regime the R-T instability becomes a electrostatic mode which excites electric field along the density interface, that causes an exchange of mass by $\mathbf{E} \times \mathbf{B}$ drift. (The two fluid approximation on the linear growth of the R-T instability is summarized in Appendix B, in which the linear analysis shows that the difference in the growth rate between the ideal and the two fluid MHD regime is negligible in this situation.) Figure 3.23 shows the absolute value of the electric field normalized by the convection electric field $V_0 B_0/2c$ and the electrostatic potential obtained at $t = 66.3\lambda/V_0$. The strong electric field which is about 4 times larger than $B_0V_0/2c$ is excited along the density interface and the accompanying deformation in the electrostatic potential indicates that the electric field is electrostatic, which is caused by a difference in the response to the centrifugal force between ions and electrons. This electric field deforms the electron density boundary into fine structures so that the mixing rate follow the ion's.

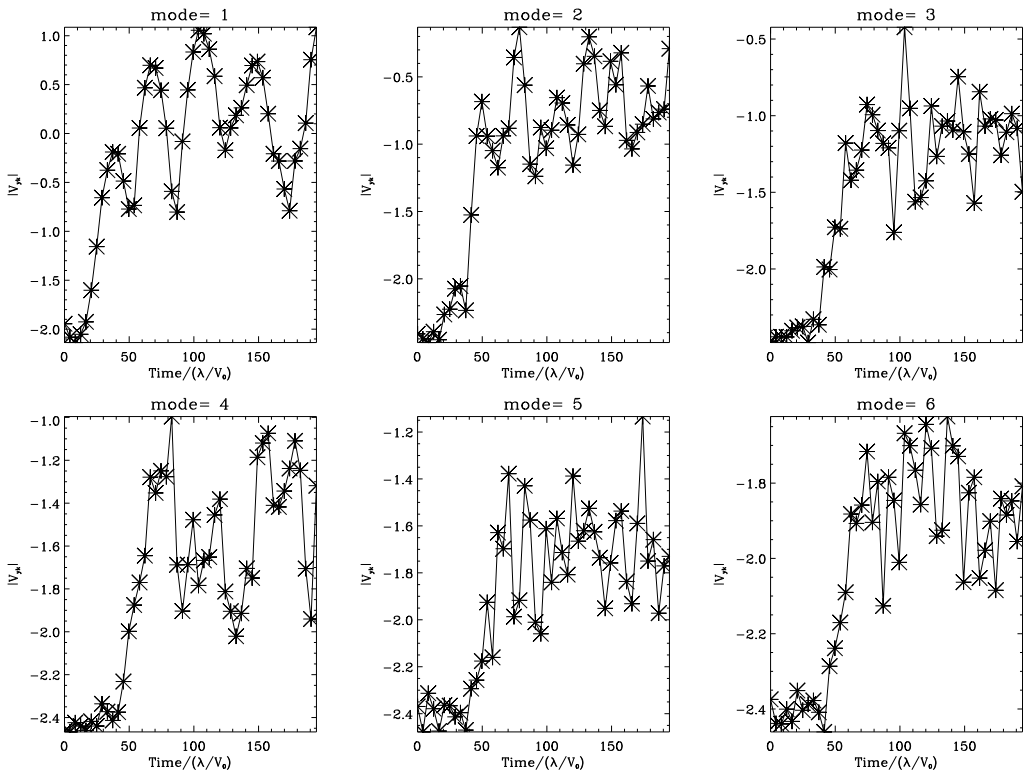

Figure 3.21: The time developments of the power of the waves whose mode number ranges from one(K-H mode, top left) to six(bottom right) are shown. The y component of the perturbed ion velocity is taken to be Fourier transformed in the x direction and then integrated in the y direction.

3.5.5 Width of density interface

In ideal MHD simulation the width of the density interface which is a key for the onset of the secondary instability is preserved by the numerical dissipation as shown in Figure 3.14. In a kinetic regime, however, the spatial scale of the density interface is on the order of ion's gyro radius. Figure 3.24 shows the ion density profiles as a function of the y coordinate in the unit of an ion thermal gyro radius. The left column shows the initial density profiles. From the top to the bottom, the initial widths of the density are $\lambda/r_{gi} = 1.0, 2.0, 4.0$, respectively. The right column shows the snapshot of the density profiles just before the onset of the secondary R-T instability for each initial density widths at $t = 59.67, 57.45, 49.72\lambda/V_0$, respectively. The steepening of the ion density are observed at the outer edge of the K-H vortex in each

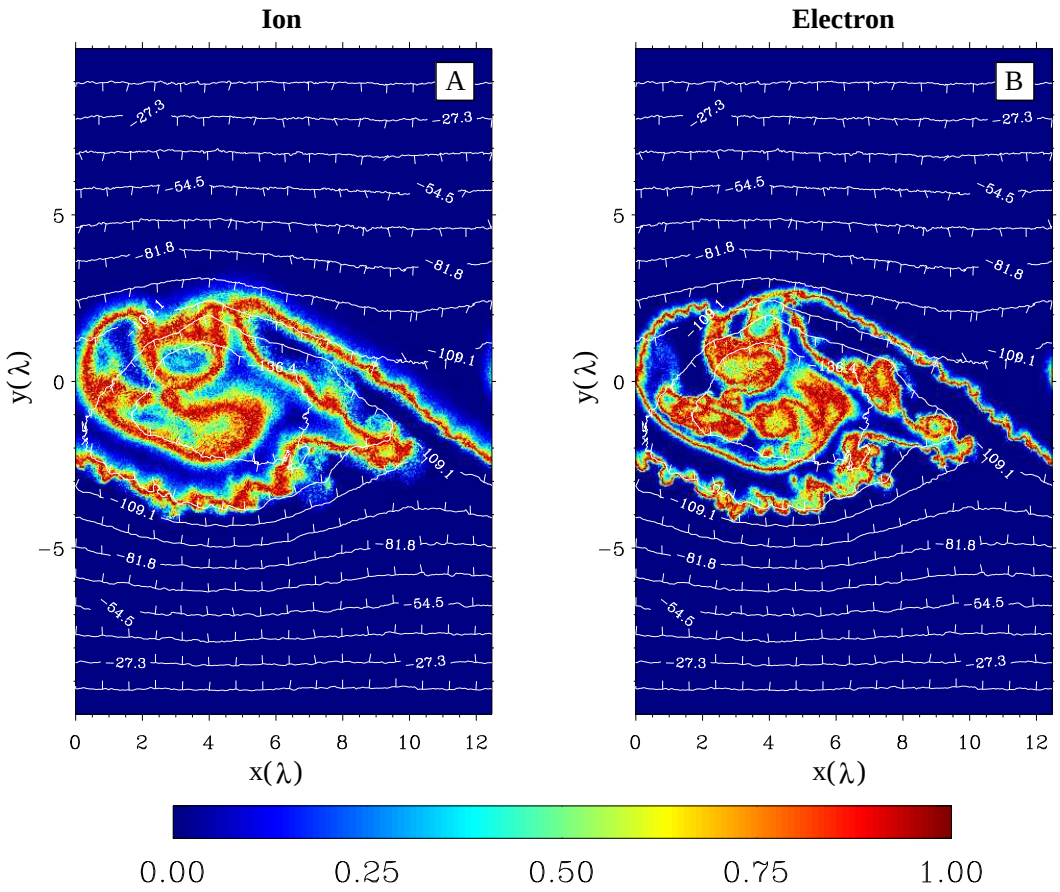

Figure 3.22: The mixing rate of (A) the ion and (B) the electron is snapshotted at $t = 66.3\lambda/V_0$ is shown in the same format of Figure 3.17.

simulations and the final width is same even though the initial width is different. The snapshot of the density profile whose initial width λ/r_{gi} is 4.0 (bottom right in Fig. 3.24) is zoomed in the Figure 3.24. The width of the density interface between the thick arrow shown in Fig. 3.25 is estimated as

$$L_N = \frac{1}{\frac{1}{N}\frac{\partial N}{\partial y}}. \tag{3.19}$$

As a result, the width of the density interface is estimated as about the ion's gyro radius. Hence, regardless of the initial width of the density interface the density interface becomes as thin as the ion gyro radius by the time of the onset of the secondary R-T instability.

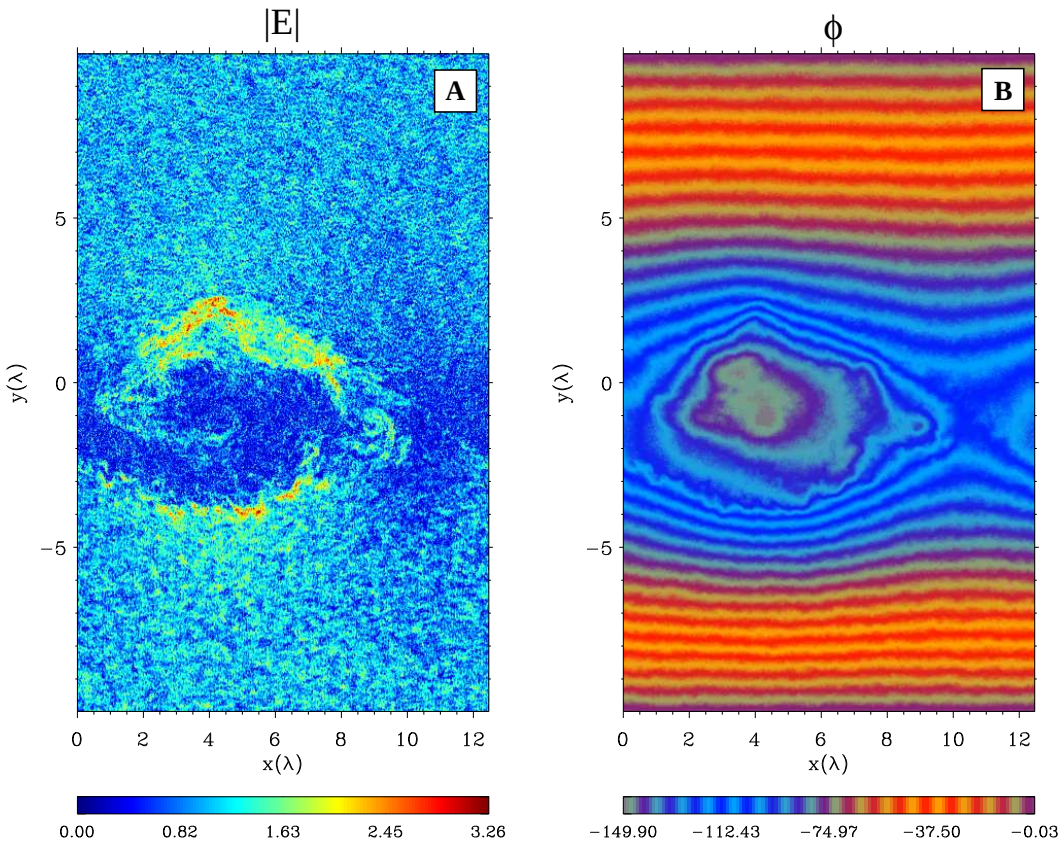

Figure 3.23: The snapshots of (A) the absolute value of the electric field and (B) the electrostatic potential at t = $66.3\lambda/V_0$ are shown in the same format of Figure 3.17.

3.5.6 Energy spectrum

In MHD simulation the onset of the turbulence makes the kinetic energy spectrum cascades to the shorter wave modes and the dissipation region of the spectrum is determined by the numerical dissipation. To explore what determines the scale of the dissipation region in a collision-less plasma Figure 3.26 and 3.27 show the time development of the power spectrum of the x component of the electric field obtained in the simulation for $\alpha = 1.0$ and $\alpha = 0.2$, respectively. In the simulation of the homogeneous case ($\alpha = 1.0$), the longest wave mode of the K-H mode dominates (Fig. 3.26). In the simulation of the in-homogeneous density case ($\alpha = 0.2$), however, the energy is transported to the shorter waves from about t = $20\lambda/V_0$. At the time t = $60\lambda/V_0$ the elongated power spectrum reached the scale of the ion gyro

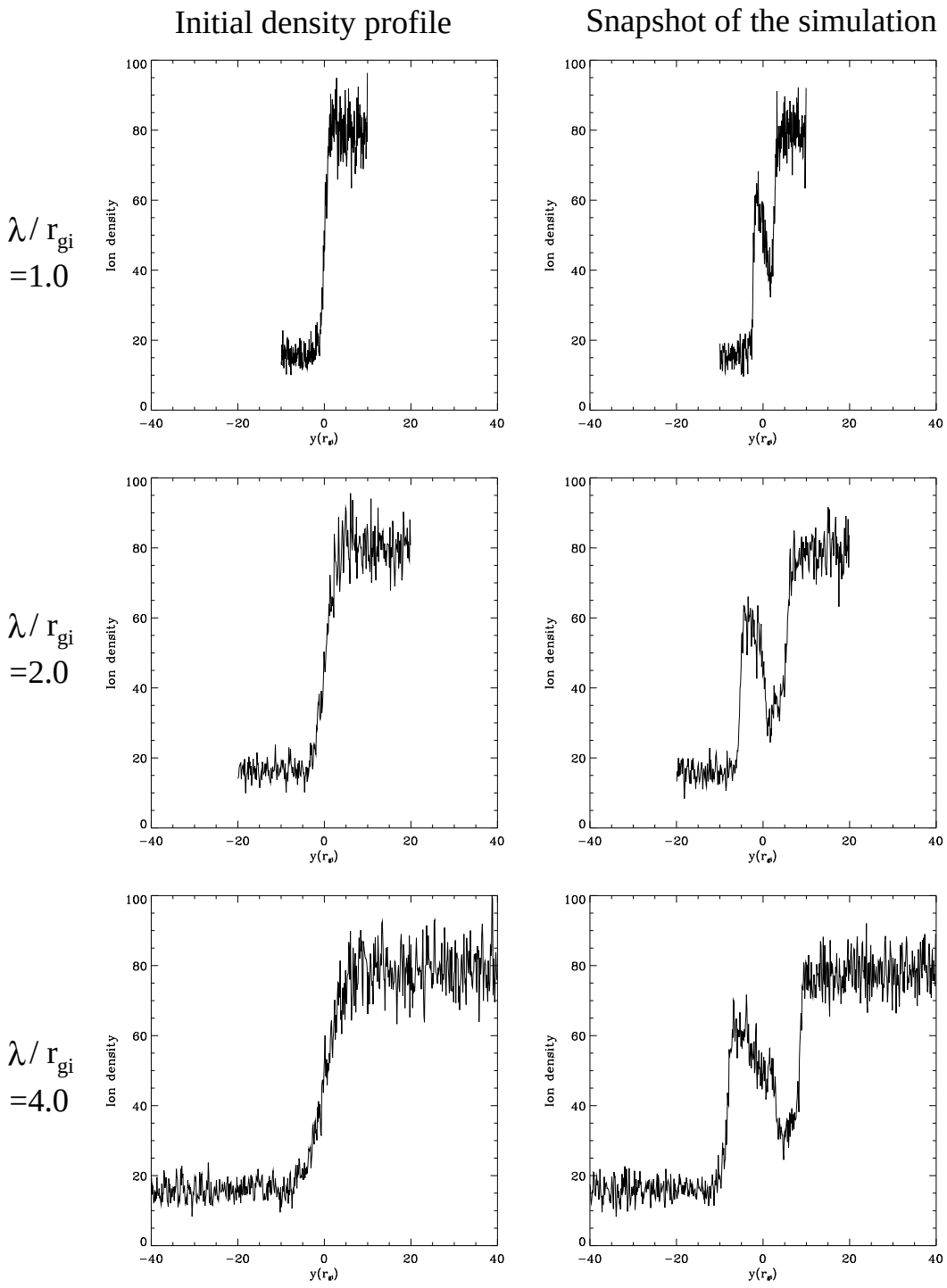

Figure 3.24: The initial (left column) and the snapshot (right column) of the ion density profiles are shown for different initial shear widths λ/r_{gi}. The abscissa shows the y coordinate in the unit of ion gyro radius r_{gi} and the ordinate shows the ion number density. From the top to the bottom the results for $\lambda/r_{gi} = 1.0, 2.0, 4.0$ are shown which are obtained at the time $t = 59.67, 57.45, 49.72\lambda/V_0$, respectively.

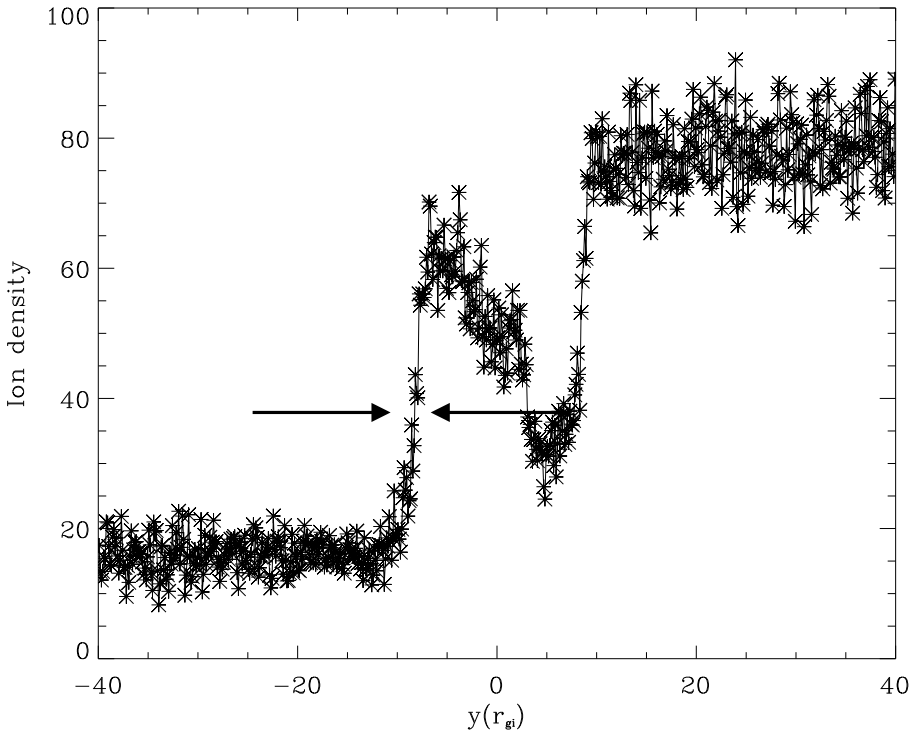

Figure 3.25: The snapshot of the density profile which is similar to the bottom right panel of Fig. 3.24 is shown in the same format of Fig. 3.24. The width of the density interface between the two horizontal arrows is estimated.

radius over which the elongation of the spectrum is inhibited. After the time $t = 60\lambda/V_0$ from the longest K-H mode to the shortest ion scale mode all waves of the scales coexist in the later part of the simulation. At the time when the energy transport to the shorter wave modes starts corresponds to the onset of the secondary R-T instability and justifies the R-T instability as a seed for the turbulence.

The power spectrum is averaged in the interval $t = 50 \sim 199\lambda/V_0$ and is shown in Figure 3.28. The solid line shows the result for $\alpha = 1.0$ and the solid red line shows the result for $\alpha = 0.2$. An energy cascade to shorter waves is evident in the result for $\alpha = 0.2$ while the longest K-H mode dominates in the result for $\alpha = 1.0$. The elongation of the spectrum reaches the scale of ion thermal gyro radius beyond which the power of the wave is slightly damped as compared to the result for $\alpha = 1.0$.

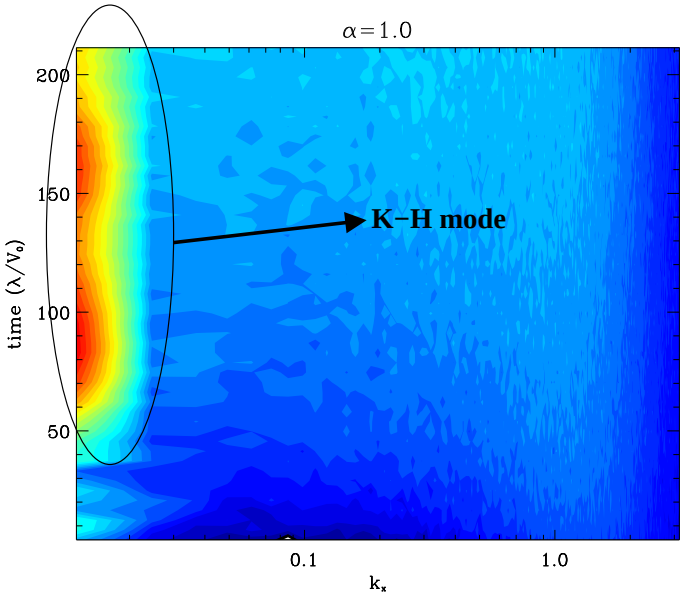

Figure 3.26: The time profile of the kinetic spectrum obtained by eq. (3.4) in the simulation for $\alpha = 1.0$ is shown. The abscissa shows the wave number in the x direction and the ordinate shows the time.The strength in color indicate the power of the wave.

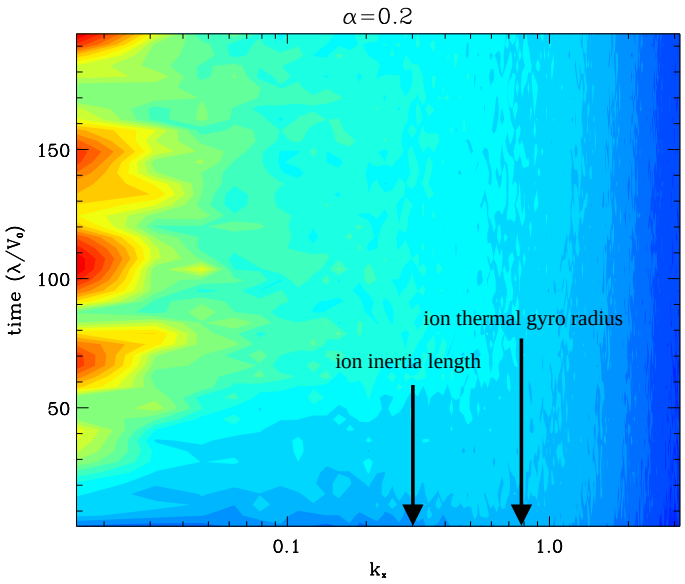

Figure 3.27: The time profile of the kinetic spectrum in the simulation for $\alpha = 1.0$ is shown in the same format of Fig. 3.26.

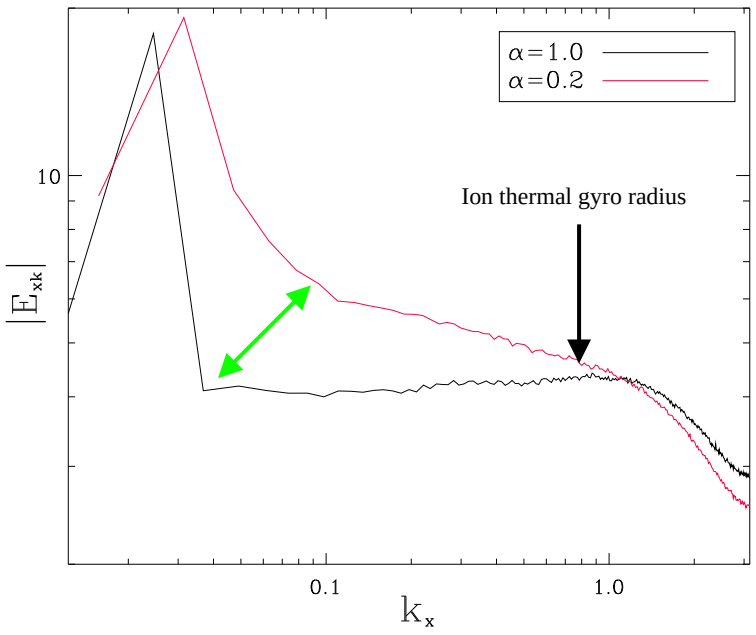

Figure 3.28: Power spectrum of the x component of the electric field averaged in the interval $t = 50 \sim 199\lambda/V_0$. The solid line shows the result for $\alpha = 1.0$ and the solid red line shows the result for $\alpha = 0.2$.

3.6 Summary and Discussion

Two-dimensional MHD and full particle simulation of the Kelvin-Helmholtz instability have shown that the inhomogeneity in fluid induces turbulence and enhances mixing of two media.

In the ideal MHD simulations the triggers of the onset are the secondary K-H and the Rayleigh-Taylor instabilities which grow inside the normal K-H vortex. Furthermore, the R-T instability also plays an important role in the mass transport to the tenuous region while the secondary K-H instability is just a seed for the turbulence. Although these two secondary instabilities themselves are classical, the excitation of secondary instabilities, in particular, the R-T instability by a normal K-H instability in a two-dimensional plane is a new concept. Once the onset is triggered turbulence is generated since the subsequent higher order instabilities are induced by the pre-excited K-H and R-T (Youngs, 1984; Jun et al., 1995) instabilities. This chain-reaction continues until the dissipation overcomes the instabilities (Fig. 3.29). The mechanism is therefore a strong non-linear coupling and the

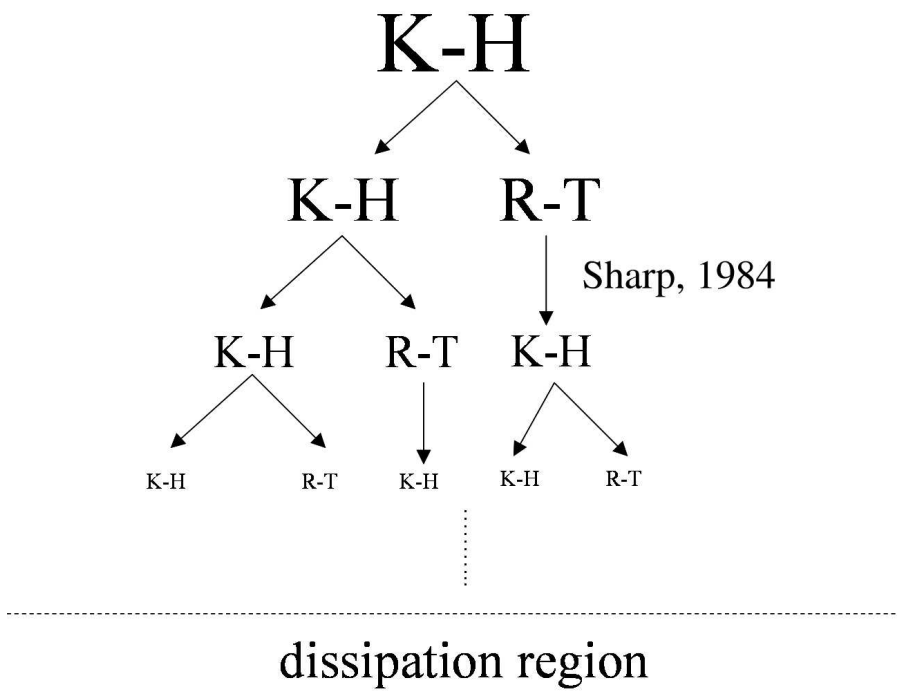

Figure 3.29: Schematic view of the self-similar system obtained by the ideal MHD simulation.

system has a self-similarity which can be related to the power law spectrum of the kinetic energy.

In a full particle simulation the similar onset of the secondary instability induces the turbulence and as a result the particles initially located in the dense region are transported across the boundary and reach at the opposite boundary, except that the only R-T instability owes as a seed for the turbulence since the secondary R-T instability grows in the first turning over motion at the outer edge of the vortex. The difference from the result in ideal MHD's is that there always exists thermal fluctuations of hot plasma at the density interface in the full particle simulation. The finest scales which is determined by a numerical dissipation in a ideal MHD is characterized by ion dynamics. The steepening of the density interface at the outer edge of the vortex is inhibited by the ion gyro motion, and the energy cascade by the turbulence is elongated to the scale of ion gyro radius beyond which the power of the waves are slightly damped.

The present study implies a significant suggestion that can be applied to a variety of

fields as well as to the interaction between the solar wind and the earth magnetosphere since the density interface with a velocity shear can be seen anywhere and the mechanism is fundamentally hydrodynamic.

CHAPTER 4

Dawn-dusk asymmetry

4.1 Introduction

The dawn-dusk asymmetry in the property of the ion components in the low latitude boundary layer (LLBL) was reported by Fujimoto et al.[1998]. In the dusk side of the LLBL, two components of the magnetospheric and magnetosheath origin are observed with clearly separated two peaks in energy as shown in Figure 3.2. On the other hand, the less clear distinction in energy are observed in the dawn side. They explained that this asymmetry is originated from the cross tail magnetic drift of the plasma sheet ions, bringing more energetic ions to the dusk side (Sarafopoulos et al., 2001).

This kind of asymmetry has also been recognized as a problem of the initial loading of the particles in a non-uniform electric field for a particle simulation (Cai et al., 1990; Cai et al., 1993a; Pritchett, 1993). Cai et al.[1990] showed that the kinetic equilibrium is different in a positive (dusk) and a negative (dawn) shear layer, both of which are modified from that in MHD if the velocity shear is strong enough ($\frac{1}{\Omega_{gi}}\frac{dV_x}{dy} >> 1$). They explained that this difference comes from the difference in the potential (non-uniform electric field) structure as indicated in Figure 4.1. Ions in a positive shear around the origin are in stable equilibrium (left in Fig. 4.1) while ions in a negative shear are in unstable equilibrium (right in Fig. 4.1) whose orbits diverge away from the shear layer. Hence, the ions in a negative velocity shear layer have effectively larger gyro radii, which can be a stabilizing effect on the linear growth of the K-H instability.

It has been also reported that the non-linear development of the K-H instability reveals a dawn-dusk asymmetry. Wilber and Winglee[1995] demonstrated the full particle simulation

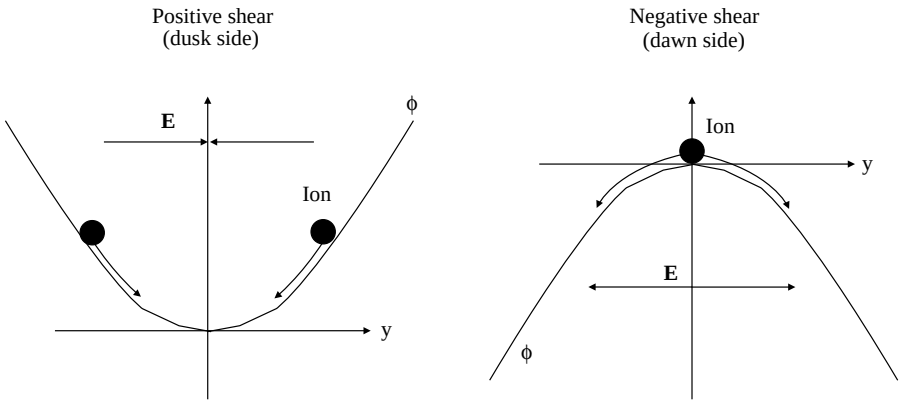

Figure 4.1: Schematic view of the ion motions in the positive (left) and negative (right) shear layer. Adopted and modified from Fig. 7 in Cai et al.[1990].

of the K-H instability modeling the dawn and the dusk LLBL. They pointed out a dawn-dusk asymmetry in the non-linear development of the K-H instability which showed the vortex formation in the dusk side and the tongues of magnetosheath plasma penetrating into the magnetosphere in the dawn side. This asymmetry increases with decreasing the initial velocity shear width. Huba[1996b] showed that the linear and the non-linear development of the K-H instability are dependent on the sign of $\mathbf{B} \cdot \mathbf{\Omega}$, where $\mathbf{\Omega} = \nabla \times \mathbf{V}$ denotes the vorticity. The finite Larmor radius (FLR) effect of the ion increases or decreases the linear growth rate when $\mathbf{B} \cdot \mathbf{\Omega} > \mathbf{0}$ (dusk side) or $\mathbf{B} \cdot \mathbf{\Omega} < \mathbf{0}$ (dawn side). Furthermore, the non-linear development of the K-H instability is also different and they suggested that the K-H turbulence may be asymmetric with respect to the dawn and dusk flanks of the solar wind interaction with a planetary or cometary plasma if the boundary layer is sufficiently thin.

While the dawn-dusk asymmetry in the initial equilibrium and the linear growth of the K-H instability have been studied and understood, the physical process which causes the asymmetry in the non-linear stage has been unclear. In this chapter the full particle simulation of the K-H instability for a negative velocity shear layer explains what causes the asymmetry in the non-linear development of the K-H instability and shows that it does not strongly depend on the width of the initial shear layer and is a unique feature of collision-less plasmas that cannot be found in the MHD regime.

4.2 Initial condition

Simulation parameters used in the following results are similar to that in Section 3.5 except that the velocity profile is given as

$$V_x(y) = \frac{V_0}{2}\tanh\left(\frac{y}{\lambda}\right), \tag{4.1}$$

$$M_A = \frac{V_0}{V_A} = +1.0, \tag{4.2}$$

so that the structure of the potential is bell-shaped one as shown in the right of Figure 4.1. (Convective electric field, $E_y(y) = V_x(y)B_z$, diverges.) Plasma paramters used in the simulations shown in the following section are summarized in Table 4.1.

Table 4.1: Plasma parameters used in the simulations in this chapter.

λ/r_{gi}	V_0/V_A	α	N_{SW}	N_{MSP}	β_{ion}	$\beta_{electron}$	M/m	ω_{ge}/ω_{pe}	section
4.0	+1.0	0.2	80	16	0.15	0.15	16	0.35	4.3
4.0	-1.0	0.2	80	16	0.15	0.15	16	0.35	3.5, 4.3 (for comparison)

4.3 Non-linear development for $\lambda/r_{gi} = 4.0$ and $\alpha = 0.2$

In this section, the full particle simulation with the thick initial velocity shear layer ($\lambda/r_{gi} = 4.0$) is conducted and shows an asymmetry in the non-linear stage of the K-H instability between the negative and the positive shear cases.

In the linearly growing stage, the K-H mode develops as seen in the positive shear case (Fig. 3.16(B)) since the potential structure does not strongly affect on the ion orbits and thus the linear growth rate of the K-H instability if the width of the velocity shear layer is sufficiently thick. In the non-linear stage, however, clear differences are obtained. Figure 4.2 shows the snapshots of the density profiles in the same format of Figure 3.17 in the right column. Comparing with the result of the positive shear case in the left column, the significant onset of the secondary instability cannot be found and the mixing region is restricted within

the K-H vortex size. As have been discussed, the transition from the laminar to the turbulent flows is strongly dependent on the existence of the secondary instabilities, particularly, of the secondary R-T instability. In the present simulation, however, the significant development of the secondary instabilities cannot be found in the first turn over motion of the K-H vortex as was seen in the positive shear case (Fig. 3.17(B)). This can be also confirmed in the time developments of the mode amplitudes. Figure 4.3 shows the time development of the wave amplitudes of the modes (1 (K-H) to 6) for the positive (black solid line) and the negative (red solid line) shear cases. The K-H mode (mode 1, top left) stands longer in the negative shear case than in the positive shear case. The smaller modes (4-6) in the negative shear case start growing later and saturate in the smaller amplitudes than in the positive shear case. As a result, the mixing rates of both the ion and the electron increase slower than in the positive shear case as shown in Figure 4.4. These results suggest that some stabilizing effects might be operating at the outer edge of the vortex and inhibit the onset of strong turbulence.

Figure 4.5(A) shows the profile of the x component of ion velocity at $t = 72.93\lambda/V_0$. At the outer edge of the vortex sharp velocity shear boundaries are newly formed in both the positive and negative y region. The origin of the velocity difference is explained in section 3.4, that is, the heavier fluid turns slowly and the lighter fluid turns fast since the fluid elements feel the same force of the perturbed pressure gradient of the K-H mode. The convective electric field also exhibits a sharp transition at the edge of the vortex. Figure 4.5(B) and (C) shows the profile of the y component of the electric field and the plot of the cross-section in the y direction averaged in the region from $x = 1.56\lambda$ to 3.13λ (solid black box). As indicated by two pairs of arrows, the velocity shear boundary in the negative y region corresponds to a negative shear and the other corresponds to a positive one. We therefore think that the thin and negatively sheared boundary has a stabilizing effect on the secondary instability.

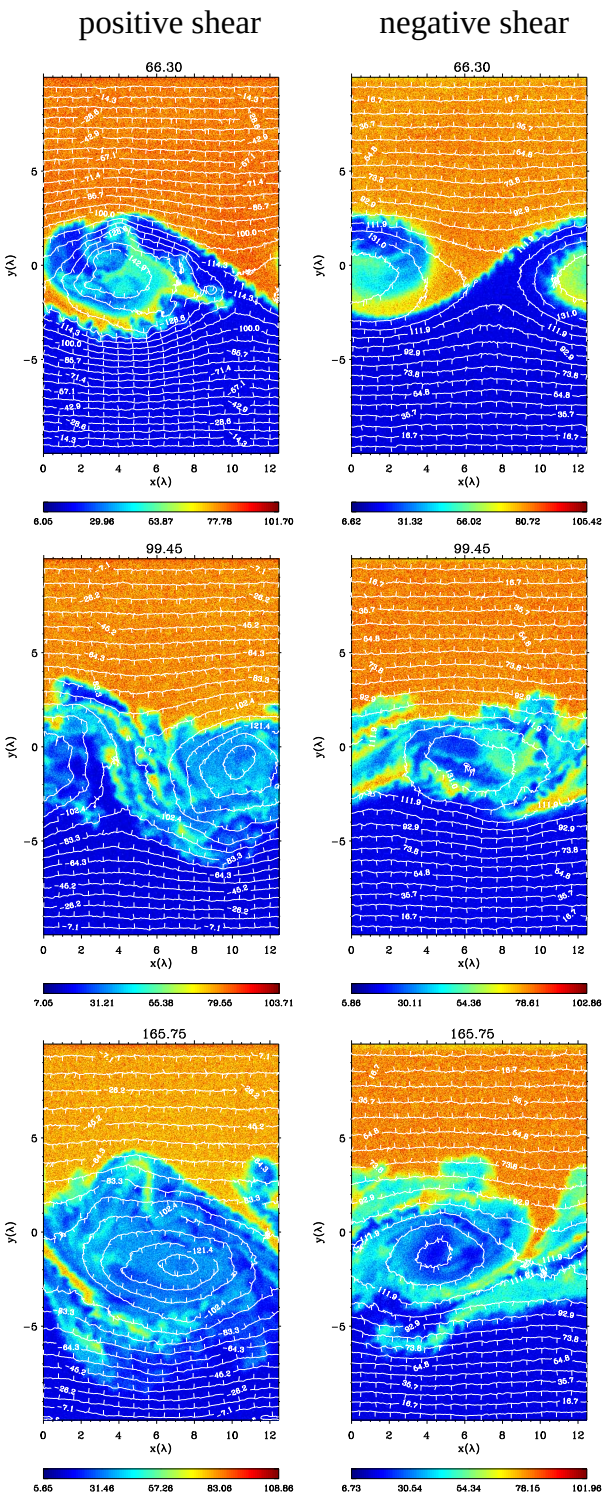

Figure 4.2: Number density profiles are shown in the right column. The left column shows the result obtained in the positive shear case for the comparison. Snapshots are taken from the top to the bottom at t=66.30, 99.45, and 165.75λ/V_0.

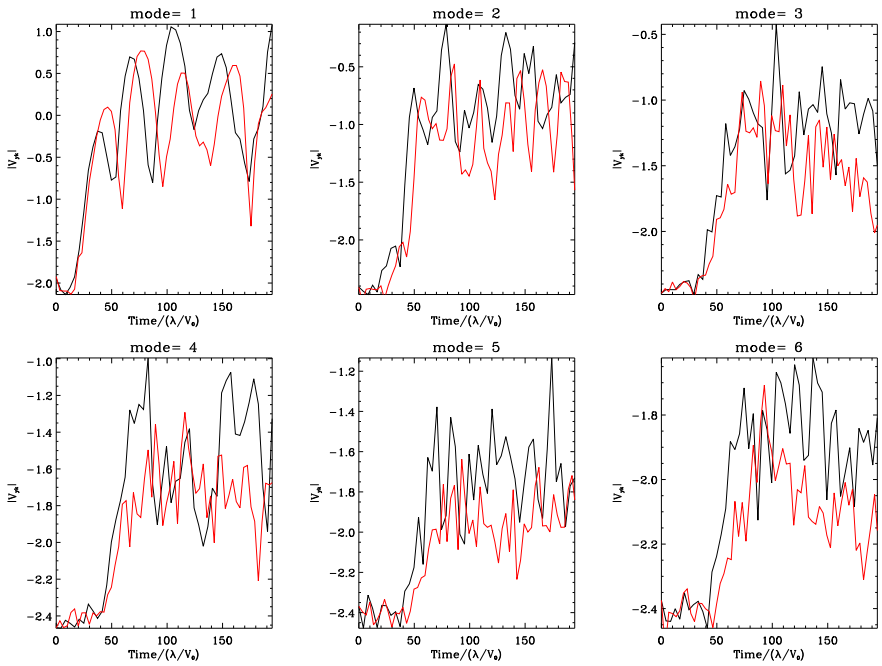

Figure 4.3: The time developments of the wave amplitudes whose mode number ranges from one(K-H mode, top left) to six(bottom right) are shown in the same format of Fig.3.21. The black and red solid lines show the result for the positive and the negative shear case, respectively.

4.4 Ion orbits in a strong velocity shear layer

The finite Larmor radius (FLR) effect of ions modifies the orbits inside a thin velocity shear (non-uniform electric field) layer. In a positively sheared layer ($\mathbf{B}\cdot\mathbf{\Omega} > 0$, where $\mathbf{\Omega} = \nabla \times \mathbf{V}$) ion orbits converge inside the shear layer while in a negatively sheared layer($\mathbf{B}\cdot\mathbf{\Omega} < 0$) they diverge away from the center of the shear layer (Cai et al.[1990]). This difference in the orbit of the ion comes from the difference in the potential structure which is shown in the following derivation.

Let the magnetic field direct to the z direction and be uniform in the x-y plane. Thus, particles move in a two-dimensional x-y plane, with velocity v_x and v_y. The electric field has only the y component which is non-uniform in the y direction. With these initial conditions,

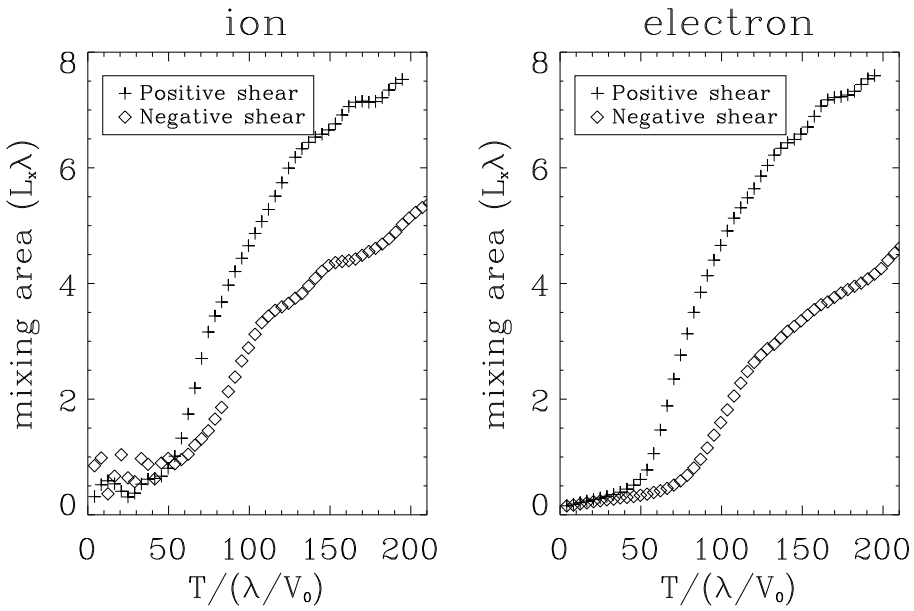

Figure 4.4: The time development of the mixing rate of (A) the ion and (B) the electron for the positive (cross) and the negative (open diamond) shear layers are shown in the same format of Fig. 2.9.

the constant of motion is obtained from the equation of motion in the x direction,

$$\frac{dv_x}{dt} = \frac{q}{mc} v_y \mathrm{B_z} = \frac{q}{mc}\frac{dy}{dt}\left(\frac{dA_x}{dy}\right) = -\frac{q}{mc}\frac{dA_x}{dt}, \tag{4.3}$$

where q and m denote the charge and the mass of the particle, c denotes speed of the light and we used the vector potential $\mathbf{A}$ in the relation

$$\mathrm{B_z} = \nabla \times \mathbf{A}|_z = -\frac{\partial \mathrm{A_x(y)}}{\partial y}. \tag{4.4}$$

From eq. (4.3), we obtain

$$\begin{aligned} \frac{d}{dt}\left(v_x + \frac{q\mathrm{A_x}}{mc}\right) &= 0, \\ v_x + \frac{q\mathrm{A_x}}{mc} &= \text{const.} \equiv p_x. \end{aligned} \tag{4.5}$$

The equation of motion in the y direction can be transformed to

$$\frac{dv_y}{dt} = \frac{q}{m}\mathrm{E_y} - \frac{q\mathrm{B_z}}{mc} v_x$$

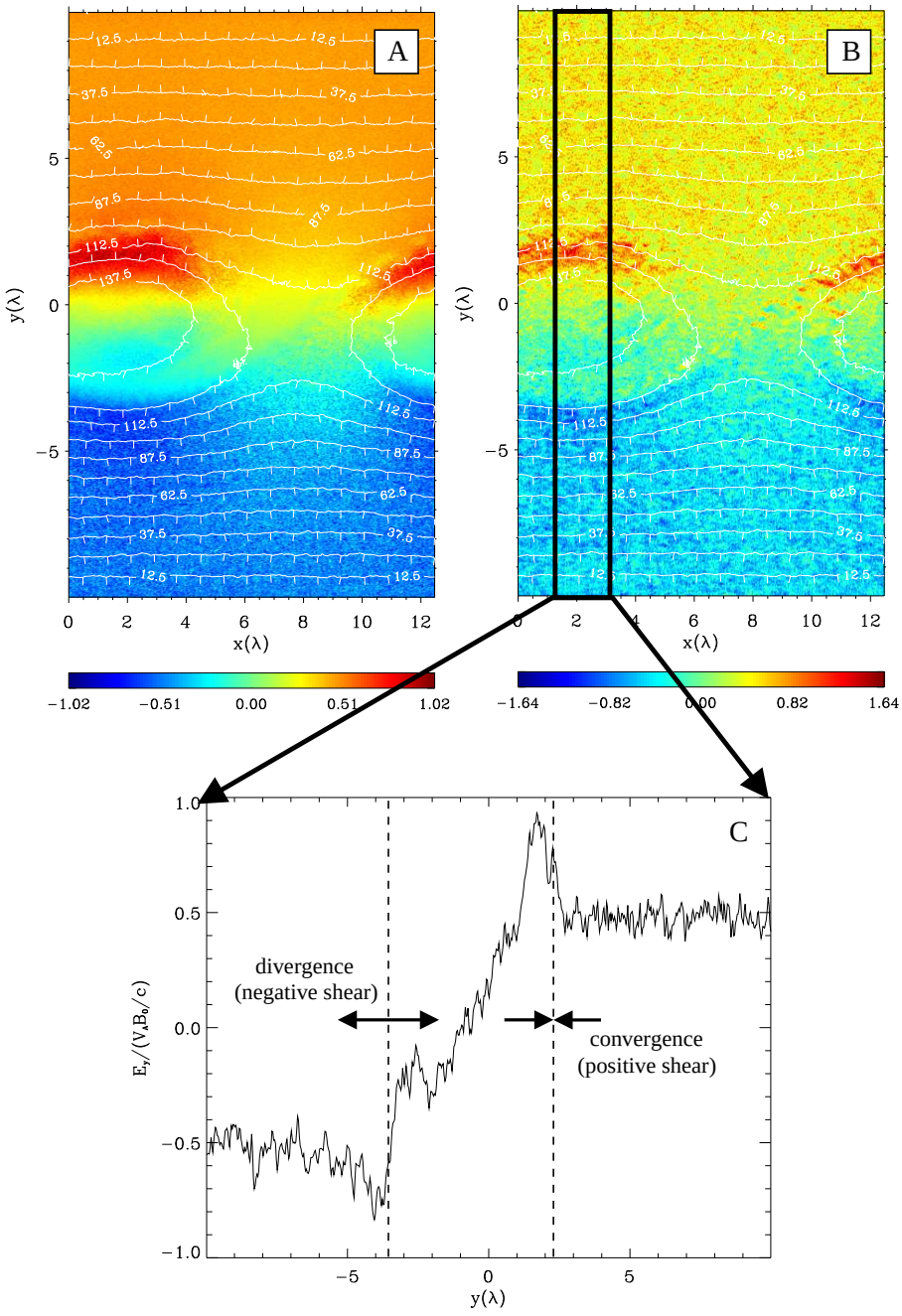

Figure 4.5: (A) The x component of the ion velocity and (B) the y component of the electric field are shown at a time $t = 72.93\lambda/V_0$, which are normalized by Alfvén speed defined in the region $y = +10\lambda$ and $V_A B_0/c$, respectively. The contour lines show the electrostatic potential. The cross-section profile of the y component of the electric field in the y direction averaged over the region from $x = 1.56\lambda$ to 3.13λ (solid black box) is shown in (C).

$$
\begin{aligned}
&= -\frac{q}{m}\frac{\partial\phi}{\partial y} - \frac{q}{mc}\left(-\frac{\partial \mathrm{A_x}}{\partial y}\right)\left(p_x - \frac{q\mathrm{A_x}}{mc}\right) \\
&= -\frac{q}{m}\frac{\partial\phi}{\partial y} - \frac{1}{2}\frac{\partial}{\partial y}\left(p_x - \frac{q\mathrm{A_x}}{mc}\right)^2 \\
&= -\frac{\partial\Phi}{\partial y}, \qquad (4.6)
\end{aligned}
$$

where we used the relations

$$
\mathrm{E_y} = -\frac{\partial\phi}{\partial y},
$$

$$
v_x = p_x - \frac{q\mathrm{A_x}}{mc},
$$

and defined the "effective potential" as

$$
\Phi = \frac{q\phi}{m} + \frac{1}{2}\left(p_x - \frac{q\mathrm{A_x}}{mc}\right)^2. \qquad (4.7)
$$

The "effective potential" determines the motion of the particle which moves around the bottom of the potential well.

In the simulation runs, the electrostatic potential is given as

$$
\phi = -\frac{\mathrm{V_0 B_0}\lambda}{2c}\log\left(\cosh\left(\frac{y}{\lambda}\right)\right) + C_1 \qquad (4.8)
$$

so that the y component of the electric field becomes

$$
\mathrm{E_y} = \frac{\mathrm{V_0 B_0}}{2c}\tanh\left(\frac{y}{\lambda}\right), \qquad (4.9)
$$

or, equivalently, the x component of the fluid velocity becomes

$$
\mathrm{V_x} = \frac{\mathrm{V_0}}{2}\tanh\left(\frac{y}{\lambda}\right). \qquad (4.10)
$$

Also, the x component of the vector potential is given as

$$
\mathrm{A_x} = \mathrm{B_0}y \qquad (4.11)
$$

so that the z component of the magnetic field is uniform in the x-y plane. Inserting eqn. (4.8) and eqn. (4.11) into eqn. (4.7), we obtain the effective potential structure for the present particle simulations as

$$
\Phi = -\frac{\Omega_{\mathrm{gs}}\lambda\mathrm{V_0}}{2}\log\left(\cosh\left(\frac{y}{\lambda}\right)\right) + \frac{1}{2}\left(p_x - \Omega_{\mathrm{gs}}y\right)^2 + \frac{q_s}{m_s}C_1, \qquad (4.12)
$$

where $\Omega_{gs} = q_s B_0/m_s c$ is a gyro frequency of the particle and the subscript 's' denotes the particle species (ion and electron). The constant value, $q_s/m_s C_1$, determines the position of the origin of the potential. To model the velocity shear layer, which appeared at the outer edge of the K-H vortex (Fig. 4.5), the structures of the potential well are obtained for the ion by giving

$$\frac{V_0}{\Omega_{gi}\lambda} = \pm 2.58, \tag{4.13}$$

where $V_0/(\Omega_{gi}\lambda)$ is a control parameter which expresses the strength of the velocity shear. (Note + (-) sign stands for the negative (positive) shear layer.) Here we assumed that the constant of motion of the ion is given as

$$\begin{aligned} p_x &= v_x + \frac{qA_x}{m_i c} \sim < v_x > + \frac{qB_0 y}{m_i c} \\ &= V_x(y) + \frac{qB_0 y}{m_i c} \\ &= \frac{V_0}{2}\tanh\left(\frac{y}{\lambda}\right) + \frac{qB_0 y}{m_i c}. \end{aligned} \tag{4.14}$$

For the ions initially located at y=0, the potential structures are obtained for the positive and the negative velocity shear layer in Figure 4.6. Comparing with the result for the case

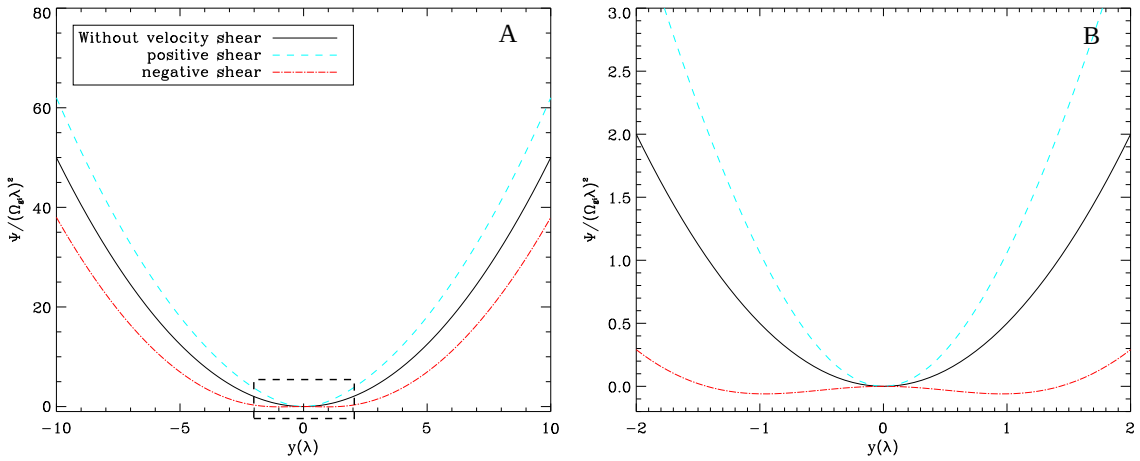

Figure 4.6: (A) Potential structures calculated from eqn. (4.12) for the case without velocity shear (black), the positive shear case (blue) and the negative shear case (red). (B) The potential profiles around the center of the velocity shear layer are zoomed in the right panel.

without velocity shear, the ions feel stronger potential that confines them at the origin for

the positive shear case. On the other hand, the negative velocity shear relaxes the potential structure which has the minimum values around $y = \pm 1\lambda$ and ions initially located at y=0 can freely moves over the velocity shear scale. From these result, the strong velocity shear effectively increases or decreases the ion gyro radius which is strongly dependent on the sign of $\mathbf{B} \cdot \mathbf{\Omega}$.

4.5 Modeling the outer edge of the vortex

Extracting the outer edge of the vortex where the positive and the negative velocity shears are newly induced, the ion motion is investigated by the full particle simulation. The initial conditions used in the simulation runs are

- $\mathrm{V_0}/(\Omega_{\mathrm{gi}}\lambda) = \pm 2.58$
- $\lambda/\mathrm{r_{gi}} = 1.0$
- $|\mathrm{V_0}|/\mathrm{V_A} = 1.0$
- $\alpha = 0.2$
- $\beta_{\mathrm{ion}} = \beta_{\mathrm{electron}} = 0.15$
- $\mathrm{L_x} = 0.25\lambda_{\mathrm{FGM}}$

The last item indicates that no K-H mode develops during the simulation runs. Figure 4.7 shows the time development of the occupation rate of the ion defined in eq. (2.3) for (A) the positive and (B) the negative shear cases. As predicted in Fig. 4.6, the ions in the negative shear layer diffuse in the spatially broader area as compared to the positive shear case during a few gyro motions. The standard deviation of the position in the y direction is also calculated by

$$\mathrm{sdv}(t) = \sqrt{< (y_i(t) - y_i(0))^2 > - < y_i(t) - y_i(0) >^2}, \tag{4.15}$$

where <> denotes the ensemble average. Figure 4.8 shows the time development of the standard deviation for the ions initially located inside the layer ($y = -1\lambda \sim 1\lambda$) for the

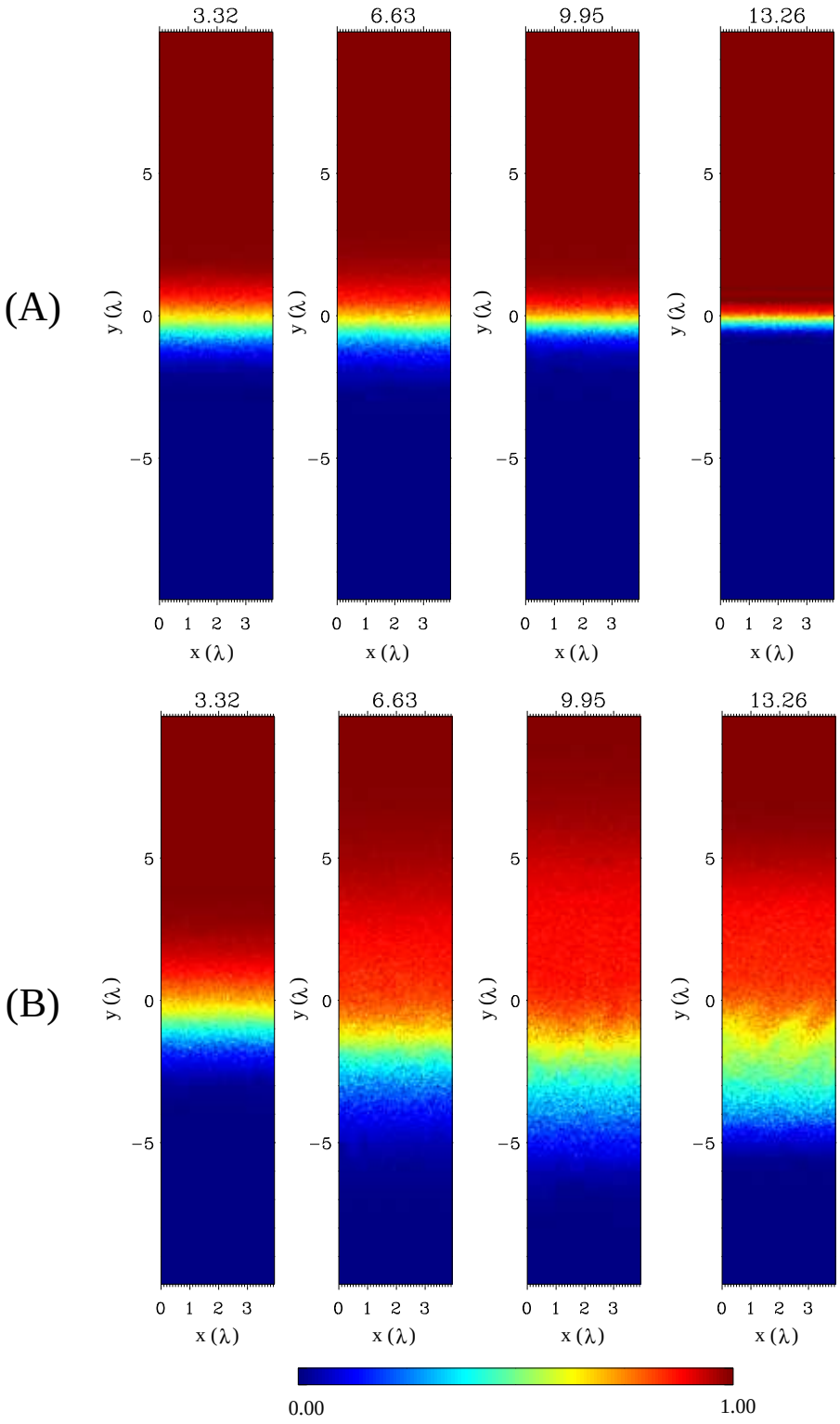

Figure 4.7: The time development of the occupation rate for (A) the positive and (B) the negative shear cases. Time proceeds from the left to the right. Four snapshots are taken at $t = 3.32, 6.63, 9.95, 13.26\lambda/\mathrm{V}_0$.

positive (solid line) and the negative (dashed line) shear cases. The ions in the positive

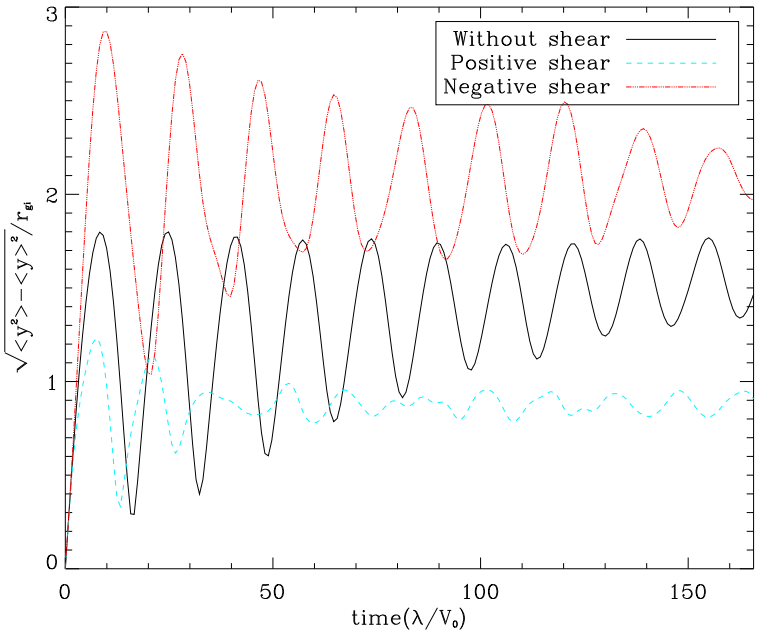

Figure 4.8: The time development of the standard deviation calculated from eqn. (4.15). The standard deviation is normalized by the thermal ion gyro radius defined in the region y=+10 λ.

shear layer spread within a scale which is slightly smaller than the thermal gyro radius defined in the region $y = +10\lambda$. On the other hand, the ions in the negative shear layer quickly diffuse in a scale which is about twice larger than the thermal gyro radius. These results indicate that the ions in the velocity shear newly induced at the outer edge of the vortex are weakly or strongly scattered.

Returning to the result shown in Fig. 4.5, one recalls that the K-H instability induces the strong velocity shears at the outer edge of the vortex in the non-linear stage. In the negative y region the shear layer corresponds to the negative shear and the opposite side corresponds to the positive one. (For the sake of simplicity, the outer edge of the vortex in the negative y region is mainly focused since that region is important for the triggering mechanism of the strong turbulence. Hereinafter, we call this region 'the region N'.) According to the previous results, the ions have effectively larger gyro radii in the negative shear layer while they are

confined in the center of the positive shear layer. This characteristic is clearly indicated in Figure 4.9 in which a sum of the ion and the electron mixing rate (eqn. (2.4)) is shown for (A) the positive ($\mathbf{B_0} \cdot \mathbf{\Omega_0} > 0$) and (B) the negative ($\mathbf{B_0} \cdot \mathbf{\Omega_0} < 0$) shear cases. (For avoiding any confusions, 'positive (negative) shear case' notes the initial velocity shear condition, i.e., a sign of $\mathbf{B_0} \cdot \mathbf{\Omega_0}$, and 'positive (negative) shear layer' notes the newly induced velocity shear at the outer edge of the vortex in the non-linear stage of the K-H instability.) The profile is snapshotted just prior to the onset of the secondary instability in the positive shear case (A), and the corresponding profile is taken for the negative shear case (B). The number density profiles are also shown for comparison in (C) and (D) for each simulation runs. In the positive shear case (A), the sum of the mixing rate takes a value 2 in the region N, indicating that the mixing region of the ion is likely to coincide with the that of the electron. In this case, the region N corresponds to the positive shear layer which effectively decreases the ion gyro radius. The FLR effect of the ions therefore weakly operates to stabilize the secondary instability, say, the R-T instability and thus the region N is destabilized even though the scale of the density interface is of the order of the ion thermal gyro radius as shown in Fig. 3.25. On the other hand, in the negative shear case (B), the sum of the mixing rate in the region N reveals more diffusive profile, indicating that the ions are scattered in the broader area. This region corresponds to the negative shear which effectively increases the ion gyro radius. Hence, the increased FLR effect of the ion with respect to the density interface strongly operates to stabilize the secondary instability, and accordingly, the onset of the strong turbulence.

4.6 Summary and Discussion

The full particle simulations of the K-H instability in the stratified shear layer have shown the asymmetry in the non-linear development between the positive and the negative velocity shear cases. In the positive shear case the onset of the secondary instability which leads the system to the turbulence appears in the early non-linear stage of the K-H instability (Chapter 3). On the other hand, the apparent transition from the laminar to the turbulent

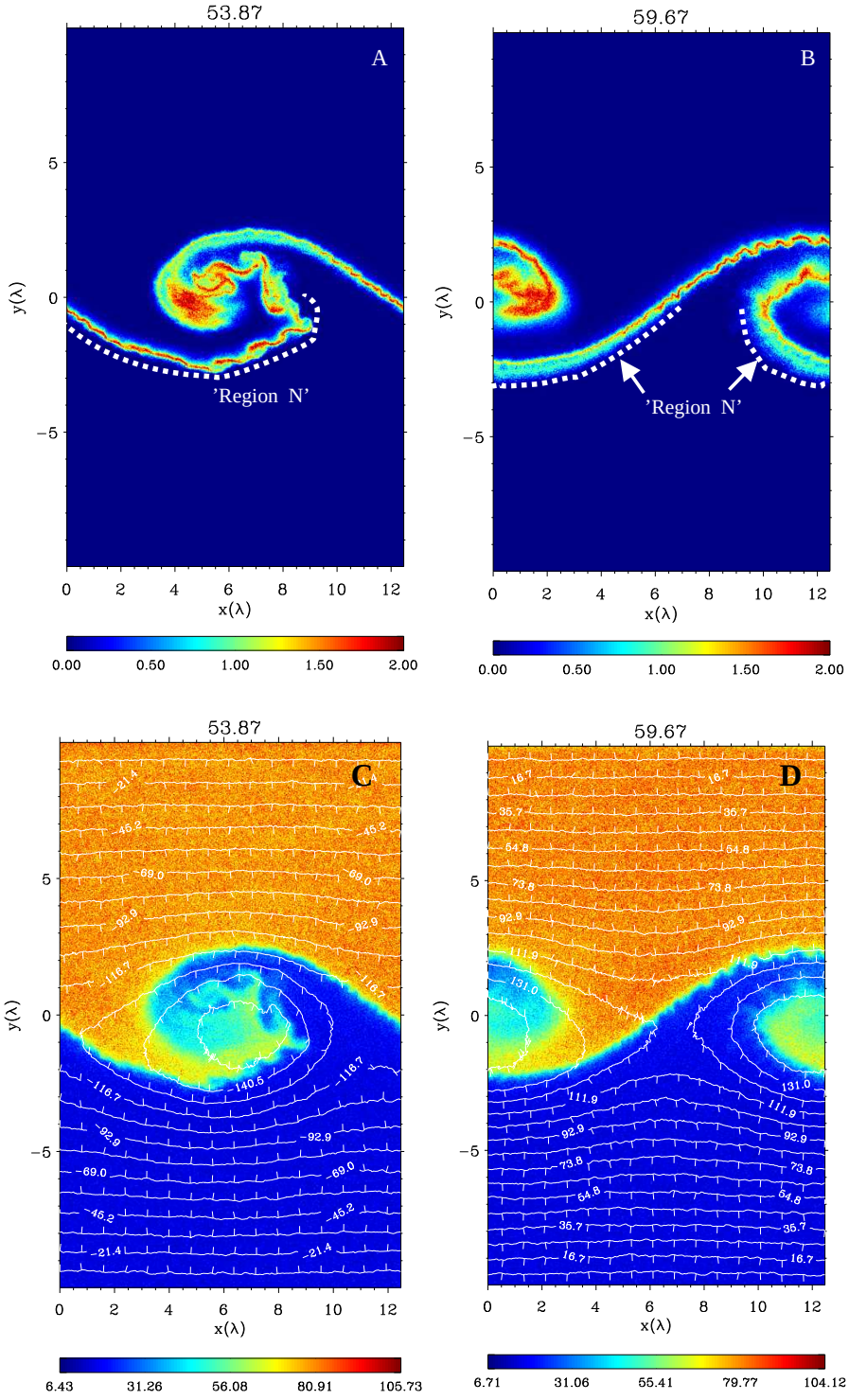

Figure 4.9: A sum of the ion and the electron mixing rate is snapshotted at (A)t = $53.87\lambda/V_0$ for the positive shear case and (B) t = $59.67\lambda/V_0$ for the negative shear case. For comparison, number density profiles are shown in (C) and (D) for each simulation runs.

flows does not appear in the negative shear case. This asymmetry was interpreted as a result of an asymmetry in the finite Larmor radius (FLR) effect at the outer edge of the vortex. A strong velocity shear layer modifies the ion orbit. In a positively sheared layer ($\mathbf{B}\cdot\mathbf{\Omega} > 0$), a sum of scalar (electric field) and vector (magnetic field) potential acts to confine the ions at the center of the shear layer, which effectively decreases the ion gyro radius. In contrast to the positive shear layer, the scalar potential acts to relax the slope of vector potential inside the negatively sheared layer ($\mathbf{B}\cdot\mathbf{\Omega} < 0$), which makes the ions freely move over a scale of the velocity shear layer. This cancellation between the scalar and the vector potential effectively increases the ion gyro radius.

The difference in the FLR effect appears at the newly induced velocity shear layer in the non-linear stage of the K-H instability. In the positive shear case ($\mathbf{B_0}\cdot\mathbf{\Omega_0} > 0$) the outer edge of the vortex in the negative y region, where is R-T unstable, becomes a positive shear. The FLR effect weakly stabilize the onset of the secondary instability, particularly the R-T instability. On the other hand, in the negative shear case ($\mathbf{B_0}\cdot\mathbf{\Omega_0} < 0$), the R-T unstable region becomes a negative shear layer that increases effectively the ion gyro radius. The enhanced FLR effect strongly stabilizes the onset of the secondary R-T instability.

The FLR effect on the growth of the R-T instability was discussed by Roberts and Taylor [1962] and extended by Huba [1996a] by using FLR MHD theory (Roberts and Taylor, 1962). Huba [1996a] showed the dispersion relation including the FLR effect in the short wavelength limit ($k\mathrm{L_n} >> 1$) as

$$\omega^2 + \frac{1}{2} v_{thi} \frac{\mathrm{r_{gi}}}{\mathrm{L_n}} k\omega + \frac{\mathrm{g}}{\mathrm{L_n}} = 0, \tag{4.16}$$

where $\mathrm{r_{gi}}$, v_{thi} and 'g' denotes ion thermal gyro radius, ion thermal speed, and gravitational acceleration, respectively. $\mathrm{L_n}$ is the density gradient scale length. In this limit the FLR stabilize the instability when

$$k\mathrm{L_n} > 4 \frac{\sqrt{\mathrm{gL_n}}}{v_{thi}} \frac{\mathrm{L_n}}{\mathrm{r_{gi}}}. \tag{4.17}$$

In the long wavelength limit ($k\mathrm{L_n} << 1$), the dispersion relation becomes

$$\omega^2 + \frac{1}{2} v_{thi} \mathrm{r_{gi}} A k^2 w + kgA = 0, \tag{4.18}$$

where A is the Atwood number defined as $\mathrm{A} = (n_1 - n_2)/(n_1 + n_2)$. The FLR effect stabilizes the instability when

$$(k\mathrm{L_n})^3 > \frac{16}{A}\frac{g\mathrm{L_n}}{v_{thi}^2}\left(\frac{\mathrm{L_n}}{\mathrm{r_{gi}}}\right)^2 \tag{4.19}$$

In both limits, the FLR effect with respect to the density gradient scale has a stabilizing effect and limits the unstable wave number region. This effect must be operating strongly at the density interface where the secondary R-T instability is expected to grow in the negative velocity shear case.

The present mechanism shown in this chapter is caused by the ion dynamics in the non-linear stage of the K-H instability which cannot be obtained in a MHD regime. Although the newly induced velocity shears at the outer edge of the vortex are obtained in both MHD and kinetic simulations of the stratified K-H instability, the kinetic effect of the ions alters the non-linear development and produces the asymmetry between the positive and the negative velocity shear cases. This mechanism can be applied to Sun and the earth interaction at the dawn and the dusk flank of the earth magnetosphere. Assuming and simplifying that the magnetic field directs to northward, the dawn (dusk) side becomes a negatively (positively) sheared layer interacting with the fast tail ward solar wind. Therefore, the transport mechanism of the solar wind plasma into the earth magnetosphere may reveal asymmetry between in the dawn and the dusk side flank.

CHAPTER 5

Concluding remarks

5.1 Summary and Conclusions

The Kelvin-Helmholtz instability has been studied extensively in the interdisciplinary fields. In the present dissertation the interaction between the solar wind and the earth magnetosphere is the objective to elucidate how the K-H instability plays a role in the mass transport into the earth magnetosphere. For that purpose, the non-linear development of the K-H instability for the transverse magnetic field case was studied in the view point of the mixing and transport of the collision-less plasmas by means of the computational experiments.

In chapter 2 the development of the K-H instability in a uniform background field was studied. Kinetic effects of electrons as well as of ions on the mixing process of collision-less plasmas across the transverse magnetic field were explored by means of full particle simulation. The results indicated that the most mixed region was restricted within the interface of two plasmas. The interpretation of the time profile of the mixing area was that the interface at which two plasmas face was stretched, folded, and deformed in the course of the development of the K-H instability and as a result, the increase in the length of the interface mainly contributed to the increase in the mixing area. The cross-field diffusion in the direction perpendicular to the interface was also operative at the same time. Incorporating these two mechanisms, the mixing area was found to be scaled to the dimensionless parameter $\sqrt{D_\perp/\lambda V_0}$. The other point to be noted is the effective electron mixing. Electrons were found to follow the ion mixing area in spite of the small gyro radius. This mechanism was caused by the electric field fluctuations. The fluctuated electric field deformed the structure of the demarcation line of the electron into fine structures and as a result, stretched path

length of the demarcation line mainly contributed to follow the ion mixing area.

In chapter 3 the development of the K-H instability in a stratified shear layer modeling the low latitude boundary at the earth magnetosphere was studied by means of MHD and full particle simulation. What is newly found in this chapter is that the stratification in density effectively enhances the mixing area both in time and spatial extent.

Ideal MHD simulation showed that two kinds of secondary instabilities which start growing in the non-linear stage of the K-H instability triggered the onset of the turbulence. One of them was identified as a secondary K-H instability and the other, which was the more important finding, was identified as a secondary Rayleigh-Taylor instability. While the secondary K-H instability was just a seed for the turbulence, the secondary R-T instability played not only as a seed but also as a mass transporter to the tenuous region. Once the turbulence was initiated by these secondary instabilities, the normal K-H vortex no longer maintained its structure and the system proceeded to turbulent structure. In the final stage of the simulation run the mixing layer extended deeply in the tenuous region and the width of the mixing layer was much thicker than the size of the normal K-H vortex.

Full particle simulation in the same configuration shown in the ideal MHD simulation was also carried out for the first time. The result obtained in the ideal MHD simulation was reproduced except that the secondary R-T instability grew in the early stage of the normal K-H instability. The first turning over motion of the K-H instability made the fluid element feel centrifugal force that induced the secondary R-T instability since the thermal fluctuation which was absent in the ideal MHD simulation existed anywhere at the density interface.

To explore the effect of in-homogeneity in magnetic field on the onset of turbulence, the ideal MHD simulation was conducted with a in-homogeneous temperature profile without the density stratification. As a result no development of the turbulence was confirmed in the ideal MHD regime, and we conclude that the density stratification is important for the effective mass transport across the velocity shear layer.

In chapter4, the full particle simulations of the K-H instability in the stratified shear layer showed the asymmetry in the non-linear development between the positive and the

negative velocity shear cases. In the positive shear case the onset of the secondary instability, which lead the system to the turbulence, appeared in the early non-linear stage of the K-H instability (Chapter 3). On the other hand, the apparent transition from the laminar to the turbulent flows did not appear in the negative shear case. This asymmetry was interpreted as a result of an asymmetry in the finite Larmor radius (FLR) effect at the outer edge of the vortex. The difference in the FLR effect appeared at the newly induced velocity shear layer in the non-linear stage of the K-H instability. In the positive shear case ($\mathbf{B_0} \cdot \mathbf{\Omega_0} > 0$) the outer edge of the vortex in the negative y region, where is R-T unstable, became a positive shear. The FLR effect weakly stabilized the onset of the secondary instability, particularly the R-T instability. On the other hand, in the negative shear case ($\mathbf{B_0} \cdot \mathbf{\Omega_0} < 0$), the R-T unstable region became a negative shear layer that increased effectively the ion gyro radius. The enhanced FLR effect strongly stabilized the onset of the secondary R-T instability and thus the effective plasma mixing by the strong turbulence.

5.2 Important issues for future works

Since the model used in the present simulations was quite simple as compared to the actual situation in the magnetosphere, some important issues are remained for the complete understanding of the mass transport by the K-H instability.

The onset mechanism of turbulence presented in this dissertation is fundamentally hydrodynamic. For the case of a inhomogeneous magnetic field geometry, however, a coupling between the K-H and the plasma micro instabilities is expected to alter the non-linear development. Specifically, the lower-hybrid drift instability in the current sheet is expected to grow faster than the K-H instability and the modified density interface will affect the development of the turbulence shown in this dissertation.

We have revealed the enhanced electric field excited by the secondary R-T instability inside the K-H vortex. The mechanism is attributed to the centrifugal force by the rotation motion, which causes a difference in motion between the ion and electron. This different responses to the acceleration cause the electrostatic field which deforms the electron mixing

area. Hence, the lager mass ratio of the ion to the electron will excite the larger amplitude of the electrostatic field. Therefore, the simulation with the larger mass ratio is expected to show heatings of plasma by the strong electrostatic field inside the K-H vortex and will be possible in the near future.

The present simulations were restricted within the 2-D plane. Extending our results to the three-dimensional K-H instability, some important issues appear to be addressed. In a three-dimensional hydrodynamical K-H instability, it is known that the stratification in density causes a secondary instability and turbulence. Because of the strong nonlinearity, the detail exploration requires huge computer resources and therefore the onset mechanism is still controversial. Elucidating the onset mechanism in the three-dimensional K-H instability is a challenging task and remained for the future work. For the application to the magnetospheric issues, the magnetic field should also comes into play. Exploring the three-dimensional K-H instability in a MHD regime will also give us a new understanding of the magnetospheric interactions, in particular, the coupling between the low latitude boundary layer and the ionosphere.

The results of the turbulent mixing of plasmas by the K-H instability suggest a new transport mechanism of the solar wind plasma into the earth magnetosphere. This suggestion will be verified by the in situ observation by the spacecrafts. The stratification in plasma density is a key point to explore the turbulent mixing across the low latitude boundary layer. More detailed structure of the turbulent flows will also be clear from the in situ observation by the multiple spacecrafts of the present and upcoming missions. Observations by the spacecraft will ensure our model and will again feed us a new issue which always excites us to explore.

APPENDIX A

Linear Analysis

A.1 Basic equations

A.1.1 Ideal MHD equations

Linear analysis is examined by solving as an eigen value problem by linearizing the following normalized forms of MHD equations: equation of continuity,

$$\frac{\partial n}{\partial t} = -\nabla \cdot (n\mathbf{V}) \tag{A.1}$$

momentum equation,

$$\frac{\partial \mathbf{V}}{\partial t} = -(\mathbf{V} \cdot \nabla)\mathbf{V} - \frac{1}{2n}\nabla(P + B^2) + (\mathbf{B} \cdot \nabla)\mathbf{B} + \mathbf{g} \tag{A.2}$$

equation of state,

$$\frac{\partial P}{\partial t} = -(\mathbf{V} \cdot \nabla)P - \Gamma P(\nabla \cdot \mathbf{V}) \tag{A.3}$$

and, Faraday's law with the frozen-in condition ($\mathbf{E} = -\mathbf{V} \times \mathbf{B}$)

$$\frac{\partial \mathbf{B}}{\partial t} = \nabla \times (\mathbf{V} \times \mathbf{B}), \tag{A.4}$$

where Γ is a polytropic constant, which is equal to 2 throughout the dissertation. The number density n and the magnetic field $\mathbf{B}$ are normalized by the characteristic value n_0 and B_0, the velocity $\mathbf{V}$ by the jump in velocity across the boundary, V_0, the pressure P by $B_0^2/8\pi$, spatial scale L by initial shear width λ, the time by λ/V_0, and the gravity acceleration $\mathbf{g}$ by $\Omega_{\rm gi} \mathrm{V_A}$.

A.1.2 Two fluid MHD equations

Two fluid approximation including the electron inertia can be obtained by the following normalized form of the equations: For species s (s=i:ion, e:electron), equation of continuity,

$$\frac{\partial n_s}{\partial t} = -\nabla \cdot (n_s \mathbf{V_s}) \tag{A.5}$$

momentum equation,

$$\frac{\partial \mathbf{V}_s}{\partial t} = -(\mathbf{V}_s \cdot \nabla)\mathbf{V}_s - \frac{M_i}{M_s}\frac{1}{2n_s}\nabla P_s + \frac{M_i}{M_s}\frac{q_s}{q_i}(\mathbf{E} + \mathbf{V}_s \times \mathbf{B}) + \mathbf{g} \tag{A.6}$$

and, equation of state

$$\frac{\partial P_s}{\partial t} = -(\mathbf{V}_s \cdot \nabla)P_s - \Gamma P_s(\nabla \cdot \mathbf{V}_s), \tag{A.7}$$

where M_s and q_s denote the mass and the charge of species s (=ion, electron). Along with the plasma equations, electric and magnetic field are solved with maxwell equations,

$$\frac{\partial \mathbf{B}}{\partial t} = -\nabla \times \mathbf{E} \tag{A.8}$$

$$\frac{\partial \mathbf{E}}{\partial t} = \left(\frac{c}{V_A}\right)^2 \left(\nabla \times \mathbf{B} - \Sigma_s \frac{q_s}{q_i} n_s \mathbf{V}_s\right), \tag{A.9}$$

where c denotes the speed of light. Normalizations are similar to the ideal MHD's except the velocity by the Alfvén speed V_A, the time by ion gyro-frequency Ω_{gi}, the scale length L by ion inertia V_A/Ω_{gi}, and the electric field by $V_A B_0/c$. The system of the equations (A.5 - A.9) can express all modes of plasma waves except the kinetic effects, such as, landau damping and Bernstein modes.

A.2 Linearization and solution

Physical parameters are perturbed from the equilibrium values of the number density $n_0 = n_0(y)$, the velocity $\mathbf{V_0} = (V_x(y), 0, 0)$, the pressure $P_0 = P_0(y)$, the gravity acceleration $\mathbf{g} = (0, 0, -g)$ and the magnetic field $\mathbf{B} = (B_x(y), 0, B_z(y))$ as,

$$\begin{aligned} n &= n_0 + \delta n \\ \mathbf{V} &= \mathbf{V_0} + \delta \mathbf{v} \end{aligned}$$

$$P = P_0 + \delta p$$

$$\mathbf{B} = \mathbf{B_0} + \mathbf{b}$$

with the form, $\delta A = \tilde{A}(y)\exp\left(i(k_x x - \omega t)\right)$, where A, k_x and ω denote a physical parameter, the wave number in the x direction and the angular frequency, respectively.

A.2.1 Ideal MHD

Linearizing the above Ideal MHD equations(A.1-A.4), one obtains

$$\begin{aligned}
\omega\delta n &= k_x V_x \delta n + k_x n_0 \delta v_x - i n_0 \frac{\partial \delta v_y}{\partial y} - i\frac{\partial n_0}{\partial y}\delta v_y \\
\omega\delta v_x &= k_x V_x \delta v_x - i\frac{\delta_V x}{\partial y}\delta v_y + \frac{k_x}{2n_0}\delta p + k_x \frac{B_z}{n_0} b_z + \frac{i}{n_0}\frac{\partial B_x}{\partial y} b_y \\
\omega\delta v_y &= k_x V_x \delta v_y - \frac{i}{2n_0}\frac{\partial}{\partial y}(\delta p + 2\mathbf{B}\cdot\mathbf{b}) - k_x \frac{B_x}{n_0} b_y + i\frac{g}{n_0}\delta n \\
\omega\delta v_z &= k_x V_x \delta v_z - k_x \frac{B_x}{n_0} b_z + \frac{i}{n_0}\frac{\partial B_z}{\partial y} b_y \\
\omega\delta p &= k_x V_x \delta p - i\delta v_y \frac{\partial P_0}{\partial y} + \Gamma P_0 k_x \delta v_x - i\Gamma P_0 \frac{\partial \delta v_y}{\delta y} \\
\omega bx &= k_x V_x b_x - i B_x \frac{\partial \delta v_y}{\partial y} - i\delta v_y \frac{\partial B_x}{\partial y} + i b_y \frac{\partial V_x}{\partial y} \\
\omega by &= k_x V_x b_y - k_x B_x \delta v_y \\
\omega bz &= k_x V_x b_z + k_x B_z \delta v_x - i B_z \frac{\partial \delta v_y}{\partial y} - i\delta v_y \frac{\partial B_z}{\partial y} - k_x B_x \delta v_z .
\end{aligned} \tag{A.10}$$

Solving these equations as a eigen value problem of

$$\omega \begin{pmatrix} \delta n \\ \delta v_x \\ \delta v_y \\ \delta v_z \\ \delta p \\ b_x \\ b_y \\ b_z \end{pmatrix} = \begin{pmatrix} & & & & & & & \\ & & & & & & & \\ & & & M_{i,j} & & & & \\ & & & & & & & \\ & & & & & & & \\ & & & & & & & \\ & & & & & & & \\ & & & & & & & \end{pmatrix} \begin{pmatrix} n \\ \delta v_x \\ \delta v_y \\ \delta v_z \\ \delta p \\ b_x \\ b_y \\ b_z \end{pmatrix}, \tag{A.11}$$

one can obtain the eigen values of ω and the corresponding eigen functions for any k_x.

A.2.2 Two fluid MHD

Linearizing a set of the two fluid MHD and Maxwell equations ((A.5) - (A.9)), one obtains

$$
\begin{aligned}
\omega\delta n_i &= k_x V_{xi}\delta n_i + k_x n_{0i}\delta v_{xi} - in_{0i}\frac{\partial \delta v_{yi}}{\partial y} - i\frac{\partial n_{0i}}{\partial y}\delta v_{yi} \\
\omega\delta n_e &= k_x V_{xe}\delta n_e + k_x n_{0e}\delta v_{xe} - in_{0e}\frac{\partial \delta v_{ye}}{\partial y} - i\frac{\partial n_{0e}}{\partial y}\delta v_{ye} \\
\omega\delta v_{xi} &= k_x V_{xi}\delta v_{xi} - i\frac{\delta V_{xi}}{\partial y}\delta v_{yi} + \frac{k_x}{2n_{0i}}\delta p_i + i(e_x + \delta v_{yi}B_z) \\
\omega\delta v_{xe} &= k_x V_{xe}\delta v_{xe} - i\frac{\delta V_{xe}}{\partial y}\delta v_{ye} + \frac{k_x}{2n_{0e}}\delta p_e - iR(e_x + \delta v_{ye}B_z) \\
\omega\delta v_{yi} &= k_x V_{xi}\delta v_{yi} - \frac{i}{2n_{0i}}\frac{\partial \delta p_i}{\partial y} + i(e_y + \delta v_{zi}B_x - V_{xi}b_z - \delta v_{xi}B_z) + i\frac{g}{n_{0i}}\delta n_i \\
\omega\delta v_{ye} &= k_x V_{xe}\delta v_{ye} - i\frac{R}{2n_{0e}}\frac{\partial \delta p_e}{\partial y} - iR(e_y + \delta v_{ze}B_x - V_{xe}b_z - \delta v_{xe}B_z) + i\frac{g}{n_{0e}}\delta n_e \\
\omega\delta v_{zi} &= k_x V_{xi}\delta v_{zi} + i(e_z + V_{xi}b_y - \delta v_{yi}B_x) \\
\omega\delta v_{ze} &= k_x V_{xe}\delta v_{ze} - iR(e_z + V_{xe}b_y - \delta v_{ye}B_x) \\
\omega\delta p_i &= k_x V_{xi}\delta p_i - i\delta v_{yi}\frac{\partial P_{0i}}{\partial y} + \Gamma P_{0i}k_x\delta v_{xi} - i\Gamma P_{0i}\frac{\partial \delta v_{yi}}{\delta y} \\
\omega\delta p_e &= k_x V_{xe}\delta p_e - i\delta v_{ye}\frac{\partial P_{0e}}{\partial y} + \Gamma P_{0e}k_x\delta v_{xe} - i\Gamma P_{0e}\frac{\partial \delta v_{ye}}{\delta y} \\
\omega e_x &= i\left(\frac{c}{V_A}\right)^2\left[\frac{\partial b_z}{\partial y} - n_{0i}\delta v_{xi} - \delta n_i V_{xi} + n_{0e}\delta v_{xe} + \delta n_e V_{xe}\right] \\
\omega e_y &= \left(\frac{c}{V_A}\right)^2[k_x b_z - i(n_{0i}\delta v_{yi} - n_{0e}\delta v_{ye})] \\
\omega e_z &= \left(\frac{c}{V_A}\right)^2\left[-k_x b_y - i\frac{\partial b_x}{\partial y} - i(n_{0i}\delta v_{zi} - n_{0e}\delta v_{ze})\right] \\
\omega bx &= -i\frac{\partial e_z}{\partial y} \\
\omega by &= -k_x e_z \\
\omega bz &= k_x e_y + i\frac{\partial e_x}{\partial y},
\end{aligned}
\tag{A.12}
$$

where R denotes a mass ratio of ion's to electron's. As have been done for the ideal MHD case, these equations are solved as an eigen value problem of

$$\omega \begin{pmatrix} \delta n_i \\ \delta n_e \\ \delta v_{xi} \\ \delta v_{xe} \\ \delta v_{yi} \\ \delta v_{ye} \\ \delta v_{zi} \\ \delta v_{ze} \\ \delta p_i \\ \delta p_e \\ e_x \\ e_y \\ e_z \\ b_x \\ b_y \\ b_z \end{pmatrix} = \begin{pmatrix} & & & & & & & & & & & & & & & \\ & & & & & & & & & & & & & & & \\ & & & & & & & & & & & & & & & \\ & & & & & & & & & & & & & & & \\ & & & & & & & & & & & & & & & \\ & & & & & & & & & & & & & & & \\ & & & & & & & & & & & & & & & \\ & & & & & & & M_{ij} & & & & & & & & \\ & & & & & & & & & & & & & & & \\ & & & & & & & & & & & & & & & \\ & & & & & & & & & & & & & & & \\ & & & & & & & & & & & & & & & \\ & & & & & & & & & & & & & & & \\ & & & & & & & & & & & & & & & \\ & & & & & & & & & & & & & & & \end{pmatrix} \begin{pmatrix} \delta n_i \\ \delta n_e \\ \delta v_{xi} \\ \delta v_{xe} \\ \delta v_{yi} \\ \delta v_{ye} \\ \delta v_{zi} \\ \delta v_{ze} \\ \delta p_i \\ \delta p_e \\ e_x \\ e_y \\ e_z \\ b_x \\ b_y \\ b_z \end{pmatrix}, \tag{A.13}$$

to obtain the eigen values of ω and the corresponding eigen functions for any k_x.

APPENDIX B

Rayleigh-Taylor instability

Rayleigh-Taylor instability induced by the normal K-H instability is a important process for the effective plasma mixing and transport as shown in Chap. 3. Here a basic nature and the linear analysis of the R-T instability are shown.

B.1 Rayleigh-Taylor instability

Consider the situation of the heavy fluid superposed onto the light fluid under the presence of the gravity force. Such a density interface is unstable and is well known as Rayleigh-Taylor instability. Early efforts have analyzed the linear properties of the R-T instability (Chandrasekhar, 1961; Sharp, 1984). The linear growth rate of the R-T instability for a sharp density interface can be obtained analytically. Let the density profile to be

$$\begin{aligned} n_i(x) &= n_1, \quad \text{where } x < 0, \\ n_i(x) &= n_2, \quad \text{where } x \geq 0, \end{aligned} \tag{B.1}$$

one can obtain the growth rate

$$\gamma = \sqrt{kgA}, \tag{B.2}$$

where k is the wave number along the interface (y direction) and A is the Atwood number,

$$A = \frac{n_1 - n_2}{n_1 + n_2}. \tag{B.3}$$

For the magnetized plasma applications the R-T instability have also been studied in the framework of ideal MHD. As in the K-H instability the orientation of the magnetic field acts for the stabilization if it aligns with the density interface and does not affect the growth

if it directs perpendicular to both the direction of the density gradient and the interface. Recently Huba and Winske[1998] showed that the kinetic effects of the ion affect the growth rate for a non-uniform magnetic field configuration. While the hall term in the generalized Ohm's law enhances the growth rate in the large wave number region, the finite Larmor radius (FLR) effect stabilizes.

To check the linear growth of the R-T instability in the full particle simulation result shown in Chap. 3, the linear analysis based on the two fluid MHD equations (Appendix A) is conducted in this section. Parameters used in the analysis is as follows:

- $\beta_i = \beta_e = 0.15$
- $\lambda/\lambda_i = 1.0$
- A = 0.6667
- $g/(\Omega_{gi} V_A) = -0.08$
- $\omega_{ge}/\omega_{pe} = 0.35$
- $n(y) = 0.5 n_0 [(1 + 5.0) - (1 - 5.0) \tanh (y/\lambda)]$

Figure B.1 shows the initial condition of (A)the z component of the magnetic field , (B)the sum of ion and electron thermal pressure, and (C)the ion density. Figure B.2 shows the growth rate of the R-T instability with respect to the wave number in the x direction in the two fluid MHD regime. The result of ideal MHD case is also shown. While a finite boundary width stabilize the large wave number modes, the significant difference between the two fluid and ideal MHD results cannot be found in the present configuration, which can be applied to the result of full particle simulation in Chap. 3.

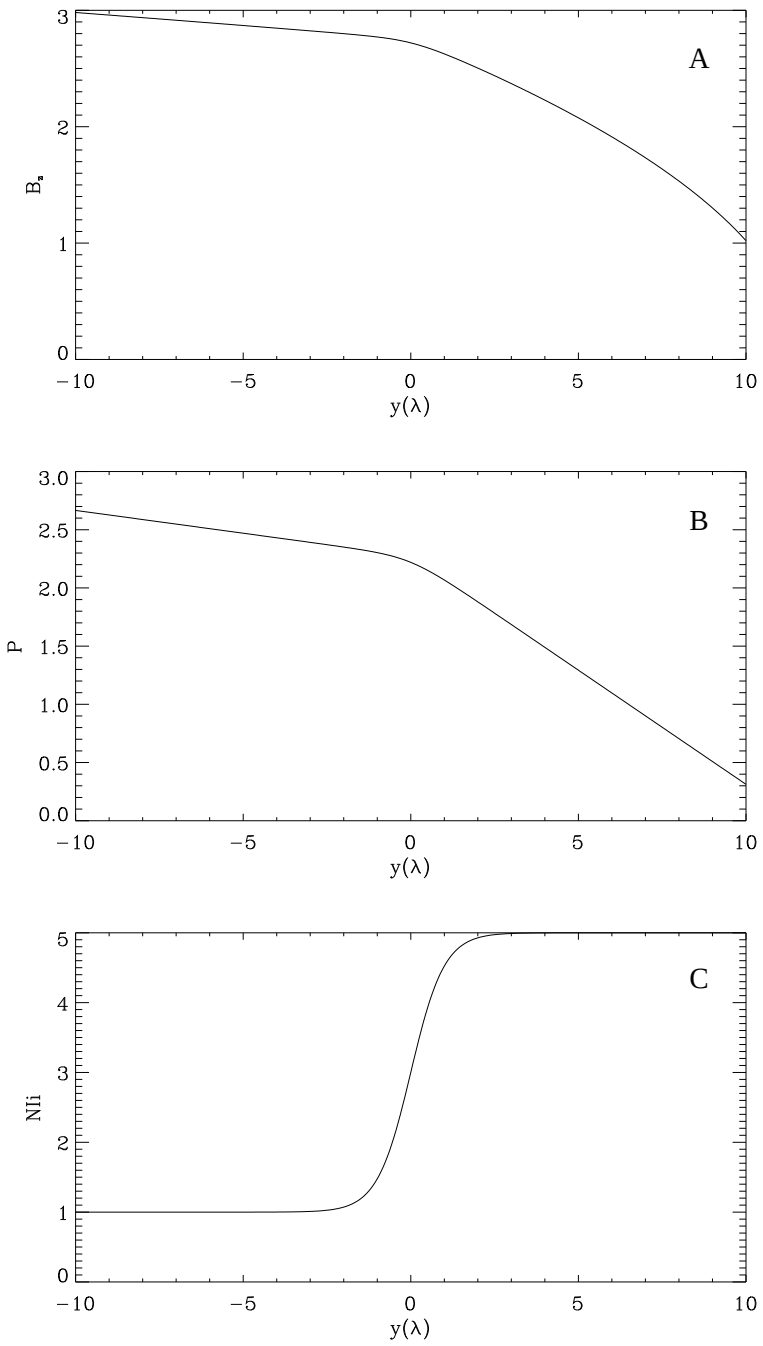

Figure B.1: Initial setting for the linear analysis. From the top to the bottom panel shown are (A)the z component of the magnetic field, (B)the sum of ion and electron thermal pressure, and (C)the ion density with respect to the y coordinate.

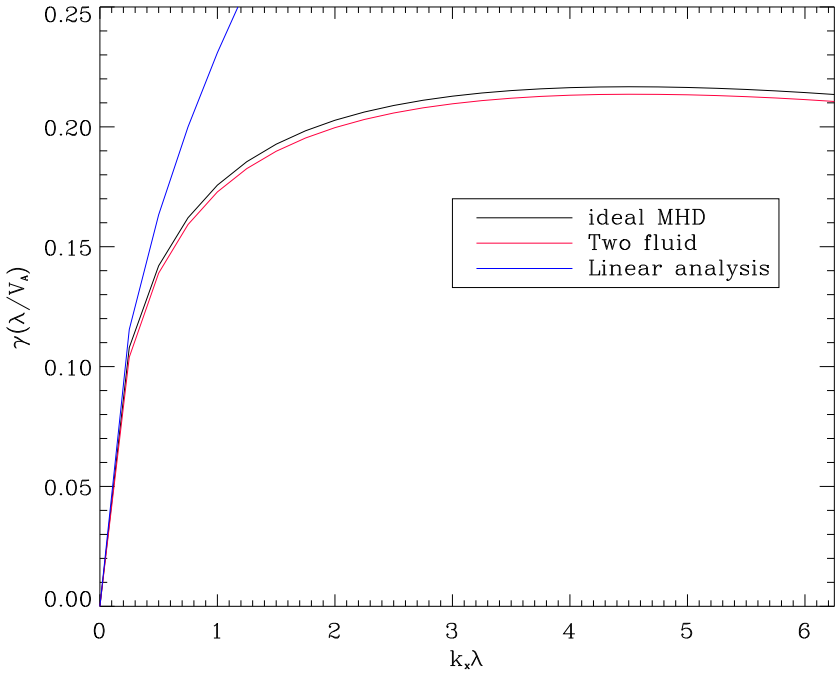

Figure B.2: Growth rate of the R-T instability in the two fluid MHD regime (solid red line). The abscissa shows the wave number in the x direction normalized by the initial boundary width and the ordinate shows the growth rate normalized by a factor λ/V_A. Along with the two fluid MHD result ideal (black) and the analytic solution of eq.(B.2) are shown.

References

[1] W. I. Axford and C. O. Hines. A unifying theory of high-latitude geophysical phenomena and geomagnetic storms. *Canad. J. Phys.*, 39:1433, 1961.

[2] W. Baumjohann, G. Paschmann, and C. A. Cattell. Average plasma properties in the central plasma sheet. *J. Geophys. Res.*, 94(A6):6597–6606, 1989.

[3] J. Berchem and C. T. Russell. The thickness of the magnetopause current layer:. *J. Geophys. Res.*, 87(A4):2108–2114, 1982.

[4] C. K. Birdsall and A. B. Langdon. *PLASMA PHYSICS VIA COMPUTER SIMULATION*. Adam Hilger, 1991.

[5] J. E. Borovsky, M. F. Thomnsen, and R. C. Elphic. The driving of the plasma sheet by the solar wind. *J. Geophys Res.*, 103(A8):17,617–17,639, 1998.

[6] D. Cai, L. R. O. Storey, and T. Itoh. Particle simulation of the kinetic kelvin-helmholtz instability in a magnetoplasma. *Phys. Fluids*, 5(10):3507–3523, Oct 1993.

[7] D. Cai, L. R. O. Storey, and T. Neubert. Kinetic equilibria of plasma shear layers. *Phys. Fluids*, 2(1):75–85, Jan 1990.

[8] D. Cai, L. R. O. Storey, and T. Neubert. Particle loading for a plasma shear layer in a magnetic field. *J. Comput. Phys.*, 107:84–97, 1993.

[9] S. Chandrasekhar. *Hydrodynamic and Hydromagnetic Stability*. Dover, 1961.

[10] J. W. Dungey. Interplanetary magnetic field and the auroral zones. *Phys. Rev. Lett.*, 6(47), 1961.

[11] T. E. Eastman, L. A. Frank, and C. Y. Huang. The boundary layers as the primary transport regions of the earth's magnetotail. *J. Geophys. Res.*, 90(NA10):9541–9560, 1985.

[12] D. H. Fairfield, R. P. Lepping, L. A. Frank, K. L. Ackerson, W. R. Paterson, S. Kokubun, T. Yamamoto, K. Tsuruda, and M. Nakamura. Geotail observation of an unusual magnetotail under very northward imf conditions. *J. Geomag. Geoelectr.*, 48(5-6):473–487, 1996.

[13] D. H. Fairfield, A. Otto, T. Mukai, S. Kokubun, R. P. Lepping, J. T. Steinberg, A. J. Lazarus, and T. Yamamoto. Geotail observations of the kelvin-helmholtz instability at the equatorial magnetotail boundary for parallel northward fields. *J. Geophys. Res.*, 105(A9):21159–21173, 2000.

[14] D. C. Fritts, T. T. Palmer, O. Andreassen, and I. Lie. Evolution and breakdown of kelvin-helmholtz billows in stratified compressible flows. part 1: Comparison of two- and three-dimensional flows. *J. Atmos. Sci.*, 53(22):3173–3191, 1996.

[15] M. Fujimoto and T. Terasawa. Ion inertia effect on the kelvin-helmholtz instability. *J. Geophys. Res.*, 96(A9):15,725–15,734, 1991.

[16] M. Fujimoto and T. Terasawa. Anomalous ion mixing within an mhd scale kelvin-helmholtz vortex. *J. Geophys. Res.*, 99(A5):8601–8613, 1994.

[17] M. Fujimoto and T. Terasawa. Anomalous ion mixing within an mhd scale kelvin-helmholtz vortex 2. effects of inhomogeneity. *J. Geophys. Res.*, 100(A7):12,025–12,033, 1995.

[18] M. Fujimoto, T. Terasawa, T. Mukai, Y. Saito, T. Yamamoto, and S. Kokubun. Plasma entry from the flanks of the near-earth magnetotail: Geotail observations. *J. Geophys. Res.*, 103(A3):4391–4408, 1998.

[19] Y. Fujita, Craig L. Srazin, Joshua C. Kempner, L. Rudnick, O. B. Slee, A. L. Roy, H. Andernach, and M. Ehle. Chandra observations of the disruption of the cool core in a133. *Astrophys. J.*, 575(2):764–778, 2002.

[20] G. Ganguli, Y. C. Lee, and P. J. Palmadesso. Kinetic theory for electrostatic waves due to transverse velocity shears. *Phys. Fluids*, 31(4):823–838, 1988.

[21] P. E. Hardee, D. A. Clarke, and A. Rosen. Dynamics and structure of three-dimensional poloidally magnetized supermagnetosonic jets. *Astrophys. J.*, 485(2):533–551, 1997.

[22] H. Helmholtz. On discontinuous movements of fluids (translated from german by f. guthrie.). *Philos. Mag.*, 36:337–346, 1868.

[23] R. W. Hockney. Measurements of collision and heating times in a two-dimensional thermal computer plasma. *J. Comp. Phys.*, 8:19–44, Aug. 1971.

[24] E. W. Hones JR., J. Birn, S. J. Bame, J. R. Asbridge, G. Paschmann, and N. Sckopke G. Haerendel. Further determination of the characteristics of magnetospheric plasma vortices with isee 1 and 2. *J. Geophys. Res.*, 86(A2):814–820, 1981.

[25] M. Hoshino. *Theoretical and Computational Studies of Plasma Kinetic Phenomena: Tearing Mode Instability and Foreshock Cyclotron Interaction.* PhD thesis, Univ. of Tokyo, 1986.

[26] J. D. Huba. Finite larmor radius magnetohydrodynamics of the rayleigh-taylor instability. *Phys. Plasmas*, 3(7):2523–2532, Jul 1996.

[27] J. D. Huba. The kelvin-helmholtz instability:finite larmor radius magnetohydrodynamics. *Geophys. Res. Lett.*, 23(21):2907–2910, Oct 1996.

[28] J. D. Huba and D. Winske. Rayleigh-taylor instability: Comparison of hybrid and nonideal magnetohydrodynamic simulations. *Phys. Plasmas*, 5(6):2305–2316, Jun 1998.

[29] Byung-il Jun, Michael L. Norman, and James M. Stone. A numerical study of rayleigh-taylor instability in magnetic fluids. *Astrophys. J.*, 453:322–349, 1995.

[30] W. Kelvin. The influence of wind on waves in water supposed frictionless. *Philos. Mag.*, 42:368–374, 1871.

[31] D. A. Knoll and J. U. Brackbill. The kelvin-helmholtz instability, differential rotation, and three-dimensional, localized, magnetic reconnection. *Phys. Plasmas*, 9(9):3775–3782, 2002.

[32] J. C. Lasheras and H. Choi. Three-dimensional instability of a plane free shear layer: An experimental study of the formation and evolution of streamwise vortices. *J. Fluid Mech.*, 189:53–86, 1988.

[33] W. Lennartsson. A scenario for solar wind penetration of earth's magnetotail based on ion composition data from the isee 1 spacecraft. *J. Geophys. Res.*, 97(A12):19,221–19,238, 1992.

[34] S. J. Lin and G. M. Corcos. The mixing layer: Deterministic models of turbulent flow. part 3. the effect of plane strain on the dynamics of streamwise vortices. *J. Fluid Mech.*, 141:139–178, 1984.

[35] A. P. Lobanov and J. A. Zensus. A cosmic double helix in the archetypical quasar 3c273. *Science*, 294:128–131, 2001.

[36] D. G. Mitchell, D. J. Williams, T. E. Eastman, L. A. Frank, and C. T. Russel. An extended study of the low-latitude boundary layer on the dawn and dusk flanks of the magnetosphere. *J. Geophys. Res.*, 92(A7):7394–7404, 1987.

[37] A. Miura. Anomalous transport by magnetohydrodynamic kelvin-helmholtz instabilities in the solar wind - magnetosphere interaction. *J. Geophys. Res.*, 89(A2):801–818, 1984.

[38] A. Miura. Kelvin-helmholtz instability at the magnetospheric boundary: Dependence on the magnetosheath sonic mach number. *J. Geophys. Res.*, 97(A7):10,655–10,675, 1992.

[39] A. Miura. Dependence of the magnetopause kelvin-helmholtz instability on the orientation of the magnetosheath magnetic field. *Geophys. Res. Lett.*, 22(21):2993–2996, 1995.

[40] A. Miura. Compressible magnetohydrodynamic kelvin-helmholtz instability with vortex pairing in the two dimensional transverse configuration. *Phys. Plasmas*, 4(8):2871–2885, 1997.

[41] A. Miura. Self-organization in the two-dimensional magnetohydrodynamic transverse kelvin-helmholtz instability. *J. Geophys. Res.*, 104(A1):395–411, 1999.

[42] A. Miura and P. L. Pritchett. Nonlocal stability analysis of the mhd kelvin-helmholtz instability in a compressible plasma. *J. Geophys. Res.*, 87(A9):7431–7444, 1982.

[43] T. K. M. Nakamura and M. Fujimoto. Electron inertia effects in an mhd-scale kh vortex. *Adv. Space Res.*, in press.

[44] A. Nishida. The geotail mission. *Geophys. Res. Lett.*, pages 2871–2873, 1994.

[45] A. Nishida, T. Mukai, T. Yamamoto, Y. Saito, and S. Kokubun. Magnetotail convection in geomagnetically active times, 1., distance to the neutral lines. *J. Geomagn. Geoelectr.*, 48(5-6):489–501, 1996.

[46] M. N. Nishino, T. Terasawa, and M. Hoshino. Increase of the tail plasma content during the northward interplanetary magnetic field intervals: Case studies. *J. Geophys. Res.*, 107(A9), 2002.

[47] M. L. Norman, L. Smarr, K. H. A. Winkler, and M. D. Smith. Structure and dynamics of supersonic jets. *Astron. and Astrophys.*, 113(2):285–302, 1982.

[48] K. Nykyri and A. Otto. Plasma transport at the magnetospheric boundary due to reconnection in kelvin-helmholtz vortices. *Geophys. Res. Lett.*, 28(18):3565–3568, 2001.

[49] K. W. Ogilvie and R. J. Fitzenreiter. The kelvin-helmholtz instability at the magnetopause and inner boundary layer surface. *J. Geophys. Res.*, 94(A11):15,113–15,123, 1989.

[50] H. Okuda and J. M. Dawson. Theory and numerical simulation on plasma diffusion across a magnetic field. *Phys. Fluids*, 16(3):408–426, 1973.

[51] R. S. B. Ong and N. Roderick. On the kelvin-helmholtz instability of earth's magnetopause. *Planet. Space Sci.*, 20(1):1, 1972.

[52] A. Otto and D. H. Fairfield. Kelvin-helmholtz instability at the magnetotail boundary: Mhd simulation and comparison with geotail observations. *J. Geophys. Res.*, 105(A9):21,175–21,190, 2000.

[53] T. L. Palmer, D. C. Fritts, and O. Andreassen. Evolution and breakdown of kelvin-helmholtz billows in stratified compressible flows. part 2: Instability structure, evolution, and energies. *J. Atmos. Sci.*, 53(22):3192–3212, 1996.

[54] T. D. Phan, L. M. Kistler, G. Haerendel, G. Paschmann, B. U. Ö. Sonnerup, W. Baumjohann, M. B. Bavassano-Cattaneo, C. W. Crlson, A. M. DiLellis, K. H. Fornacon, L. A. Frank, M. Fujimoto, E. Georgescu, S. Kokubun, E. Moebius, T. Mukai, M. Oieroset, W. R. Paterson, and H. Reme. Extended magnetic reconnection at the earth's magnetopause from detection of bi-directional jets. *Nature*, 404(20):848–850, 2000.

[55] T. D. Phan, D. Larson, J. McFadden, R. P. Lin, C. Calson, M. Moyer, K. I. Paularena, M. McCarthy, G. K. Parks, H. Réme, T. R. Sanderson, and R. P. Lepping. Low-latitude dusk flank magnetosheath, magnetopause, and boundary layer for low magnetic shear: Wind observations. *J. Geophys. Res.*, 102(A9):19,883–19,895, 1997.

[56] R. T. Pierrehumbert and S. E. Widnall. The two- and three-dimensional instabilities of spatially periodic shear layer. *J. Fluid Mech.*, 114:59–82, 1982.

[57] P. L. Pritchett. Simulation of collisionless electrostatic velocity-shear-driven instabilities. *Phys. Fluids*, 5(10):3770–3778, Oct 1993.

[58] P. L. Pritchett and F. V. Coroniti. The collisionless macroscopic kelvin-helmholtz instability 1. transverse electrostatic mode. *J. Geophys. Res.*, 89(A1):168–178, 1984.

[59] Z. Y. Pu and M. G. Kivelson. Kelvin-helmholtz instability at the magnetopause: Solution for compressible plasmas. *J. Geophys. Res.*, 88(A2):841–852, 1983.

[60] K. V. Roberts and J. B. Taylor. Magnetohydrodynamic equations for finite larmor radius. *Phys. Rev. Lett.*, 8(5):197–198, Mar 1962.

[61] C. T. Russell and R. C. Elphic. Initial isee magnetometer results: Magnetopause observations. *Space. Sci. Rev.*, 22(6):681–715, 1978.

[62] C. T. Russell and R. C. Elphic. Observation of magnetic flux ropes in the venus ionosphere. *Nature*, 279(5714):616–618, 1979.

[63] D. V. Sarafopoulos, N. F. Sidiropoulos, E. T. Sarris, V. Lutsenko, and K. Kudela. The dawn-dusk plasma sheet asymmetry of energetic particles: An interball perspective. *J. Geophys. Res.*, 106(A7):13,053–13,065, 2001.

[64] N. Sckopke, G Paschmann, G. Haerendel, B. U. Ö. Sonnerup, S. J. Bame, T. G. Forbes, E. W. Hones JR., and C. T. Russell. Structure of the low-latitude boundary layer. *J. Geophys. Res.*, 86(A4):2099–2110, 1981.

[65] A. K. Sen. Effect of compressibility on kelvin-helmholtz instability in a plasma. *Phys. Fluids*, 7:1293, 1964.

[66] J. Seon, L. A. Frank, A. J. Lazarus, and R.P. Lepping. Surface waves on the tailward flanks of the earth's magnetopause. *J. Geophys. Res.*, 100(A7):11,907–11,922, 1995.

[67] D. H. Sharp. An overview of rayleigh-taylor instability. *Physica D*, 12(1-3):3–18, 1984.

[68] D. J. Southwood. The hydromagnetic stability of the magnetospheric boundary. *Planet. Space Sci.*, 16:587–605, 1968.

[69] H. Suzuki, M. Fujimoto, and I. Shinohara. Current-sheet kink instability at ion-electron hybrid scale. *Adv. Space Res*, 30(12):2663–2666, 2002.

[70] T. Tajima, W. Horton, P. J. Morrison, J. Schutkeker, T. Kamimura, K. Mima, and Y. Abe. Instabilities and vortex dynamics in shear flow of magnetized plasmas. *Phys. Fluids B*, 3(4):938–954, 1991.

[71] N. Terada, S. Machida, and H. Shinagawa. Global hybrid simulation of the kelvin-helmholtz instability at the venus ionopause. *J. Geophys. Res.*, 107(A12), 2002.

[72] T. Terasawa, M. Fujimoto, H. Karimabadi, and N. Omidi. Anomalous ion mixing within a kelvin-helmholtz vortex in a collisionless plasma. *Phys. Rev. Lett.*, 68(18):2778–2781, 1992.

[73] T. Terasawa, M. Fujimoto, T. Mukai, I. Shinohara, Y. Saito, T. Yamamoto, S. Machida, S. Kokubun, A. J. Lazarus, J. T. Steinberg, and R. P. Lepping. Solar wind control of density and temperature in the near-earth plasma sheet: Wind/geotail collaboration. *Geophys. Res. Lett.*, 24(8):935–938, 1997.

[74] V. A. Thomas and D. Winske. Kinetic simulation of the kelvin-helmholtz instability. *Geophys. Res. Lett.*, 18(11):1943–1946, 1991.

[75] V. A. Thomas and D. Winske. Kinetic simulations of the kelvin-helmholtz instability at the magnetopause. *J. Geophys. Res.*, 98(A7):11425–11438, 1993.

[76] S. A. Thorpe. Transitional phenomena and the development of turbulence in stratified fluids: A review. *J. Geophys. Res.*, 92:5231–5248, 1987.

[77] R. A. Treumann, J. Labelle, and R. Pottelette. Plasma diffusion at the magnetopause: The case of lower hybrid drift waves. *J. Geophys. Res.*, 96(A9):16,009–16,013, Sep 1991.

[78] M. Wilber and R. M. Winglee. Dawn-dusk asymmetries in the low-latitude boundary layer arising from the kelvin-helmholtz instability: A particle simulation. *J. Geophys. Res.*, 100(A2):1883–1898, 1995.

[79] S. Wing and P. T. Newell. 2d plasma sheet ion density and temperature profiles for northward and southward imf. *Geophys. Res. Lett.*, 29(9), 2002.

[80] C. C. Wu. Kelvin-helmholtz instability at the magnetopause boundary. *J. Geophys. Res.*, 91(A3):3042–3060, 1986.

[81] D. L. Youngs. Numerical simulation of turbulent mixing by rayleigh-taylor instability. *Physica D*, 12(1-3):32–44, 1984.